

AN ULTRAVIOLET SURVEY OF LOW-REDSHIFT PARTIAL LYMAN-LIMIT SYSTEMS WITH THE HST COSMIC ORIGINS SPECTROGRAPH

J. MICHAEL SHULL, CHARLES W. DANFORTH, EVAN M. TILTON, JOSHUA MOLONEY
 CASA, Department of Astrophysical & Planetary Sciences,
 University of Colorado, Boulder, CO 80309

AND MATTHEW L. STEVANS
 Dept. of Astronomy, University of Texas at Austin, Austin, TX 78712
Draft version April 6, 2024

ABSTRACT

We present an ultraviolet spectroscopic survey of strong H I absorbers in the intergalactic medium, probing their evolution over the last 6-7 Gyr at redshifts $0.24 \leq z \leq 0.84$. We measure column densities $N_{\text{HI}} (\text{cm}^{-2})$ from the pattern of Lyman-series absorption lines and flux decrement at the Lyman limit (LL) when available. We analyzed 220 H I absorbers in ultraviolet spectra of 102 active galactic nuclei (AGN) taken by the Cosmic Origins Spectrograph aboard the *Hubble Space Telescope* with G130M/G160M gratings (1134-1795 Å). For 158 absorbers with $\log N_{\text{HI}} \geq 15$, the mean frequency is $dN/dz = 4.95 \pm 0.39$ over pathlength $\Delta z = 31.94$ ($0.24 \leq z \leq 0.84$). We identify 8 Lyman Limit Systems (LLS, $\log N_{\text{HI}} \geq 17.2$) and 54 partial systems (pLLS) with $16.0 \leq \log N_{\text{HI}} < 17.2$. Toward 159 AGN between $0.01 < z_{\text{abs}} < 0.84$ with $\Delta z \approx 48$, we find four damped Ly α absorbers (DLA) with $(dN/dz)_{\text{DLA}} = 0.083^{+0.066}_{-0.040}$ at $\langle z \rangle = 0.18$. The mean LLS frequency between $z = 0.24 - 0.48$ is $(dN/dz)_{\text{LLS}} = 0.36^{+0.20}_{-0.13}$ fitted to $N(z) = (0.25^{+0.13}_{-0.09})(1+z)^{1.14}$. For 54 pLLS we find $(dN/dz)_{\text{pLLS}} = 1.69 \pm 0.23$ at $\langle z \rangle = 0.39$, a frequency consistent with gaseous halo sizes $R \approx 100h^{-1}$ kpc for $(0.3-3L^*)$ galaxies. A maximum-likelihood analysis yields a distribution $f(N, z) = C_0 N^{-\beta} (1+z)^\gamma$ with $\beta = 1.48 \pm 0.05$ and $\gamma = 1.14^{+0.88}_{-0.89}$ for $15 \leq \log N_{\text{HI}} \leq 17.5$. The far-UV opacity gradient is $d\tau_{\text{eff}}/dz \approx (0.444)(1+z)^{1.14}$ over the range $15 \leq \log N_{\text{HI}} \leq 17$, implying mean LyC optical depth $\tau_{\text{eff}} \approx 0.3 - 0.5$ toward sources at $z = 1 - 2$.

Subject headings: cosmological parameters — ultraviolet: galaxies — observations — intergalactic medium — quasars: absorption lines

1. INTRODUCTION

Over the past decade, astronomers have uncovered large reservoirs of gas in the outer portions of galaxy halos (Tumlinson et al. 2011a, 2013; Stocke et al. 2013, 2014) and in the intergalactic medium or IGM (Penton et al. 2004; Shull et al. 2012a), far from the gravitational influence of individual galaxies. These gaseous structures are detected by absorption-line spectra of quasars and other active galactic nuclei (AGN) using resonance lines of neutral hydrogen (H I) and metal ions (e.g., C IV, O VI, Si III, C II) in the rest-frame far-ultraviolet. Shortward of the Ly α emission line at 1215.67 Å, numerous weak H I absorption lines blanket the AGN continuum in the “Lyman-alpha forest” with column densities that we have been able to measure reliably through *HST*/COS absorption-line spectra over the range $12.5 \leq \log N_{\text{HI}} (\text{cm}^{-2}) \leq 15.0$ (Danforth et al. 2016). Over the range $15 < \log N_{\text{HI}} \lesssim 17$, the Lyman lines are highly saturated, and column densities are difficult to measure from Lyman series absorption alone. When $\log N_{\text{HI}} \geq 17.2$, photoelectric absorption in the Lyman continuum (LyC) produces optical depth $\tau_{\text{LL}} \geq 1$ at the Lyman limit (LL) at $\lambda_{\text{LL}} = 911.753$ Å. These redshifted absorbers are called Lyman-limit systems (LLS), while those with slightly lower column den-

sities are termed “partial Lyman-limit systems” (pLLS). In this paper, we use the term Lyman Limit (LL) in reference to the redshifted wavelength (912 Å rest frame) and the types of absorbers (pLLS or LLS). The term Lyman decrement refers to the drop in transmitted flux at the LL, which is used to define continuum optical depth (τ_{LL}).

Spanning a loosely defined range ($16 < \log N_{\text{HI}} < 17.2$), the pLLS are commonly associated with galaxies (Sargent et al. 1989; Steidel 1990; Simcoe et al. 2006) and their gaseous halos, now more fashionably called the circumgalactic medium (CGM). Although previous *HST* surveys (Storrie-Lombardi et al. 1994; Stengler-Larrea et al. 1995; Ribaldo et al. 2011a) focused primarily on true LLS, we note that two recent surveys of “Lyman limit systems” (Ribaldo et al. 2011a; Lehner et al. 2013) also included many partial LLS in their tables. The LLS and pLLS dominate the continuum opacity of the IGM (Shull et al. 1999; Haardt & Madau 2012; O’Meara et al. 2013) and probe the metallicities in the environment around galaxies (Ribaldo et al. 2011b; Tripp et al. 2011; Lehner et al. 2013; Fox et al. 2013). Even rarer are the Damped Lyman-alpha (DLA) absorbers (Wolfe et al. 2005; Meiring et al. 2011; Turnshek et al. 2015) whose column densities, $N_{\text{HI}} \geq 2 \times 10^{20} \text{ cm}^{-2}$, are sufficient to produce strong Lorentzian wings in their absorption profiles. These H I lines provide the dominant

technique for measuring the baryon content of the IGM (Shull et al. 2012a), and the LLS/pLLS are a benchmark for determining the metallicity of the CGM (Tripp et al. 2011). Strong H I absorbers have been linked (Simcoe et al. 2006; Lehner et al. 2009; Ribaud et al. 2011b) to the extended regions of galaxies. The semantic question of “where galaxies end” (Shull 2014) depends on their gravitational influence as well as dynamical effects of gaseous outflow and infall from the cosmic web (Tripp et al. 2011).

In our recent survey (Danforth et al. 2016) of low-redshift Ly α absorbers with the Cosmic Origins Spectrograph (COS) on the *Hubble Space Telescope* (HST), we fitted the column densities to a power-law differential distribution, $f(N_{\text{HI}}) \propto N_{\text{HI}}^{-\beta}$, with $\beta = 1.65 \pm 0.02$ over the range $12.5 \leq \log N_{\text{HI}} \leq 15.0$. Column densities determined from strong Ly α lines are uncertain owing to line saturation at $\log N_{\text{HI}} \geq 14$ for typical Doppler parameters $b \approx 20 - 35 \text{ km s}^{-1}$. The distribution is also poorly constrained at $\log N_{\text{HI}} > 15$ because strong Ly α absorbers are rare. Some progress in defining their column densities has been made with access to higher Lyman lines (Ly β , Ly γ , Ly δ) from the *FUSE* satellite (Shull et al. 2000) and *HST* (Danforth & Shull 2008; Danforth et al. 2016). The higher Lyman lines become available to COS at modest redshifts ($z \geq 0.107$ for Ly β , $z \geq 0.167$ for Ly γ) and they yield more accurate measurements of the curve of growth (CoG). The LL shifts into the COS/G130M window at $z_{\text{abs}} \geq 0.24$. At $\log N_{\text{HI}} \gtrsim 16.2$, in data with good signal-to-noise ($S/N \gtrsim 10$) we can use the flux decrement at the Lyman edge to confirm and supplement the CoG solutions.

In this paper, we explore the pLLS/LLS distribution in N_{HI} and redshift, employing a “Lyman-comb” technique to find strong H I absorbers between $z_{\text{abs}} = 0.24 - 0.95$ from their pattern of Lyman-series absorption lines and Lyman edge. An accurate determination of the Ly decrement depends on reliable continuum placement longward and shortward of the LL at observed wavelength $\lambda_{\text{obs}} = (911.753 \text{ \AA})(1 + z_{\text{abs}})$. We use high-S/N spectra of 102 AGN at $z_{\text{AGN}} \geq 0.24$ with the COS G130M/160M gratings. Figure 1 shows the redshift coverage of our survey, plotting the number of AGN sight lines sensitive to the LL (at 912 \AA rest-frame). Our survey has much higher spectral resolution ($R \approx 17,000$) than earlier surveys with the low-resolution ($R \approx 1000 - 1300$) gratings on *HST*/FOS and *HST*/STIS. In well-exposed spectra with $S/N \gtrsim 10$, we are able to resolve velocity components $\Delta v = 40 - 400 \text{ km s}^{-1}$ within absorbers and construct multi-component CoGs when needed. For absorbers with $\log N_{\text{HI}} > 16.2$, the continuum optical depth at the LL is usually detectable by HST/COS with optical depth $\tau_{\text{LL}} = (6.304 \times 10^{-18} \text{ cm}^2) N_{\text{HI}} > 0.1$. By combining the Lyman decrement with CoG fitting, we can confirm the H I column density and its range of uncertainty.

The continuum can be influenced by AGN emission lines in the UV and EUV, many of which are broad and blended features that produce bumps and undulations in the underlying power-law continuum. Fortunately, we have a good template for the location of these emission features (Figure 2) obtained from the composite rest-frame UV/EUV spectrum of AGN (Shull et al. 2012b;

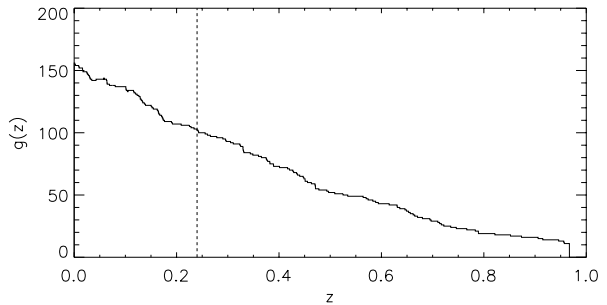


FIG. 1.— Distribution in redshift, $g(z)$, showing the number of AGN that contribute pathlength capable of detecting the redshifted LL of H I between $z = 0.003 - 0.96$. We consider only absorbers at $z \geq 0.24$ (dashed line) whose LL is redshifted into the COS/G130M band ($\lambda > 1130 \text{ \AA}$). These 102 AGN sight lines allow us to use the LL flux-decrement, when available, and curve of growth for Lyman absorption lines to determine H I column densities and assess systematic errors.

Stevans et al. 2014). We refer the reader to our papers on AGN composite spectra (Shull et al. 2012; Stevans et al. 2014) which describe our choice of line-free windows. Typical errors in continuum choice typically result in ± 0.02 errors in $\log N_{\text{HI}}$. In the rest-frame far-UV, the most prominent emission lines are the O VI doublet (1032 and 1038 \AA), C III (977 \AA), and a blend of O I features (930-950 \AA). The dominant emission lines in the rest-frame EUV (550 \AA to 912 \AA) are lines of O II and O III (833 \AA and 834 \AA), a broad complex (760-800 \AA) consisting of the Ne VIII doublet (770 \AA and 780 \AA) and O IV 788 \AA, the 700 \AA blend of O III (702 \AA) and N III (686 \AA), and strong emission lines of O IV (608 \AA, 554 \AA) and O V (630 \AA). A full list of EUV lines in the AGN composite spectrum is provided in Table 4 of Shull et al. (2012b).

The sample used in this survey began with 159 AGN targets chosen because their UV brightness allowed them to be observed by *HST*/COS with both G130M and G160M gratings. Of these 159 AGN, 102 had redshifts $z_{\text{AGN}} \geq 0.24$, sufficient to shift the LL and higher Lyman-series lines into the G130M window. This sample includes many AGN previously observed by the *International Ultraviolet Explorer* (IUE) and *HST* spectrographs. Many were used by the COS-GTO team (Danforth et al. 2016) and COS-Halos project (Tumlinson et al. 2013) for the purpose of studying the low-redshift IGM and galactic halo gas. Stevans et al. (2014) used 159 AGN with redshifts $0.001 < z_{\text{AGN}} \leq 1.476$ to produce a COS composite spectrum of AGN in their rest-frame UV and EUV. The AGN in the COS-Halos program were selected to avoid strong Mg II absorbers at $z > 0.4$, which would bias the survey against LLS. Because our survey of LLS and pLLS used only AGN with $z_{\text{abs}} \geq 0.24$, it excludes nearby Seyfert galaxies whose sight lines might be biased against LLS. Further discussion of potential sample biases for LLS and DLA is given in Section 3.3 and

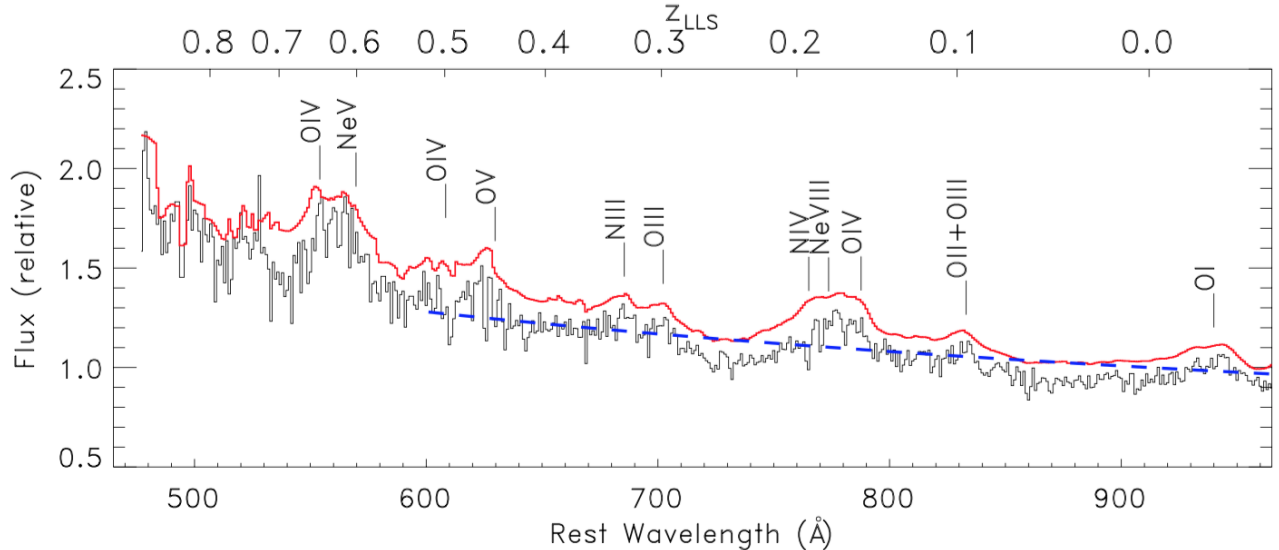


FIG. 2.— AGN composite spectrum based on Stevans et al. (2014) and annotated with prominent EUV broad emission lines of metal ions (O, N, Ne). Red spectrum shows spline fit to AGN flux passing above $\text{Ly}\alpha$ absorption lines (black). The AGN emission lines must be identified and fitted before placing the underlying EUV continuum (blue dotted line). Measuring the LL optical depth of absorbers requires careful attention to the the continuum on either side of the LL. The true continuum can be contaminated by broad emission lines such as the Ne VIII $\lambda 770, 780$ doublet, O IV $\lambda 788$, and the 685 \AA and 702 \AA lines of N III and O III. Shorter wavelength EUV lines of O IV, O V, and Ne V can affect the continuum around absorbers at $z_{\text{LLS}} = 0.45 - 0.70$.

in Ribaldo et al. (2011a) and Neeleman et al. (2016).

Spectra taken with the COS G130M/G160M gratings (Green et al. 2012) provide moderate spectral resolution ($R = \lambda/\Delta\lambda \approx 17,000$) allowing us to resolve individual Lyman-series absorbers and fit the underlying AGN continuum. With the combined coverage from the G130M grating ($1134 \text{ \AA} - 1460 \text{ \AA}$) and G160M grating ($1390 \text{ \AA} - 1795 \text{ \AA}$) we can identify LLS and pLLS out to $z_{\text{abs}} \approx 0.95$, using a template of Lyman-series absorption lines at the same redshift. Even at $\log N_{\text{HI}} < 16.2$, when the LyC optical depth is weak ($\tau_{\text{LL}} < 0.1$), we are able to identify the Lyman-line pattern down to $\log N_{\text{HI}} \approx 14.5$ in well-exposed spectra ($S/N \gtrsim 10$). Figure 3 shows three AGN sight lines with H I absorbers between $\log N_{\text{HI}} = 15.0 - 15.25$, found through higher Lyman-series absorption lines (Ly γ through Ly8). In Figure 4, we demonstrate the effectiveness of using the Lyman-line pattern, compared to the injection of weak “mock absorbers” 300 km s^{-1} to the red of the actual absorber. This confirms our ability to detect systems below 50 m\AA equivalent width in data with $S/N \gtrsim 10$.

Over the redshift range of H I absorbers in our full sample, $0.237 \leq z_{\text{abs}} \leq 0.928$, we surveyed total absorption pathlength $\Delta z_{\text{eff}} = 31.94$ and identified 211 absorbers: 8 were LLS with $\log N_{\text{HI}} \geq 17.2$, 54 were pLLS between $16.0 < \log N_{\text{HI}} < 17.2$, and the remainder lay between $14.0 < \log N_{\text{HI}} < 16.0$. Our COS survey contains the largest number of low- z LLS and pLLS to date, a distribution that we compare to absorbers in the HST/FOS Key-Project surveys of LLS at $0.4 < z < 1.4$ (Storrie-Lombardi et al. 1994; Stengler-Larrea et al. 1995) and the FOS/STIS survey of LLS at $z < 2.6$ (Ribaldo et al. 2011a).

In Sections 2 and 3, we describe the data set of LLS and pLLS absorbers and our determination of their dis-

tribution, $f(N, z)$, in column density and redshift. We find a line frequency $dN/dz = 4.95 \pm 0.39$ for $15.0 < \log N_{\text{HI}} < 18.5$ averaged over $0.24 < z < 0.84$. We quantify the pLLS distribution in H I column density and redshift through maximum-likelihood fitting to the form, $f(N, z) = C_0 N^{-\beta} (1+z)^\gamma$, with best-fit parameters $\beta = 1.48 \pm 0.05$ and $\gamma = 1.14^{+0.88}_{-0.89}$. Although the evolutionary index $\gamma \approx 1.1$ is uncertain, owing to the limited redshift coverage and statistics, it is consistent with cosmological expectations for a population of non-evolving pLLS absorbers with constant space density and absorption cross section. By integrating the distribution of absorbers, $f(N_{\text{HI}}, z)$, over column density, we compute the redshift gradient in LyC opacity, $d\tau_{\text{eff}}/dz$, for absorbers between $12.5 \leq \log N_{\text{HI}} \leq 17.2$. We estimate a far-UV (1130 \AA) continuum opacity, $\tau_{\text{eff}} \approx 0.4 - 0.5$, toward AGN at $z \approx 1.5 - 2.0$ and discuss the possible effects on AGN source selection and their rest-frame EUV spectra. In Section 4, we summarize our results and their implications for IGM photoelectric opacity in the UV, QSO UV-survey selection, and the spatial association of pLLS with galaxy halos. Appendix A gives narratives of our analysis of 73 strong H I absorbers, 23 of which were studied in previous surveys. Appendix B describes our statistical analysis and the maximum-likelihood approach to obtaining distribution parameters.

2. SURVEY TECHNIQUES

Our survey of strong H I absorbers comes as a natural by-product of the UV composite spectra of AGN constructed from moderate-resolution HST/COS data (Stevans et al. 2014). To find the underlying AGN continuum, we used G130M/G160M spectra to identify the numerous $\text{Ly}\alpha$ forest lines, as well as the less frequent but stronger (LLS and pLLS) absorbers. We did *not* consider

eight Lyman lines and decrement are easily detectable (greater than 50 mÅ equivalent width). To implement the method, we inspect the spectra for flux decrements at the LL, employing a computer script that scans for correlated down-pixels at the locations of higher-order Lyman lines of strong absorbers. When a system is confirmed, we measure the equivalent widths of up to the first 12 Lyman lines and fit them to a CoG to determine the column density and Doppler parameter (b in km s⁻¹). Our technique depends primarily on identifying the pattern of Lyman lines and less on detecting the Lyman decrement. For the standard wavelength coverage in the COS/G130M grating (1134–1459 Å), the LL becomes detectable¹ at $z_{\text{LL}} > 0.244$ and shifts out of the G130M band at $z_{\text{LL}} > 0.60$. By including wavelength coverage with the G160M grating (1400–1795 Å) we can observe the far-UV range with access to the LL out to $z_{\text{LL}} \approx 0.95$ and to various Lyman lines (Ly α - Ly ζ) over the redshift ranges shown in Table 1.

Figure 3 illustrates our method for the higher Lyman lines of three H I absorbers with $\log N_{\text{HI}} = 15.07 - 15.24$ at redshifts $z_{\text{abs}} = 0.2625, 0.4140$, and 0.5061 . All three systems were easily detected in Ly β , and two of them have Ly α (for the absorber at $z = 0.5061$, Ly α has shifted beyond the G160M window). From the expected detection limits (Table 1) in COS spectra like those shown in Figure 3, our survey is able to identify strong absorbers down to $\log N_{\text{HI}} \approx 15$. In some AGN sight lines with low S/N (~ 5), particularly those at redshifts ($z > 0.75$) where we lose Ly β , we may miss some absorbers at $\log N_{\text{HI}} = 15.0 - 15.5$.

We began with the 221 strong absorption systems identified in the 159 AGN sight lines studied by Stevans et al. (2014). Because the LL shifts into the G130M band at $z \geq 0.24$, we only searched for strong absorbers toward those 102 quasars with redshifts $z_{\text{AGN}} \geq 0.24$. For our statistical sample, we dropped a weak absorber at low column density ($\log N_{\text{HI}} = 13.5$). One LLS had a redshift ($z = 0.2374$) just below our cutoff at $z = 0.24$. We carefully re-analyzed all systems with $\log N_{\text{HI}} \geq 15.75$, combining a multi-component CoG with measurements of the Ly decrement, when detectable. To derive τ_{LL} we examined the AGN spectrum for broad emission-line contamination of the continuum on either side of the LL. In our re-analysis, we found an additional strong absorber omitted in Stevans et al. (2014), a DLA at $z_{\text{abs}} = 0.3221$. Over redshifts $0.237 \leq z_{\text{abs}} \leq 0.928$ we found eight true LLS ($\log N_{\text{HI}} \geq 17.2$), one DLA ($\log N_{\text{HI}} = 20.34 \pm 0.12$), and 54 pLLS ($16.0 \leq \log N_{\text{HI}} < 17.2$). Including the lower redshift portions of the spectrum ($z < 0.24$) we found a total of four DLAs towards all 159 surveyed AGN, at redshifts $z_{\text{DLA}} = 0.0963, 0.1140, 0.185$, and 0.3211 . Appendix A presents a narrative discussion of 73 systems with $\log N_{\text{HI}} \geq 15.75$, many of which exhibit multiple velocity components separated by $\Delta v \approx 40 - 400$ km s⁻¹.

¹ In some cases, the G130M spectra extend down to 1130 Å, allowing detection of the LL at $z \geq 0.24$. Because our Lyman-comb method relies on finding pLLS through a pattern of Lyman lines, we could also detect Lyman lines from pLLS at lower redshifts: $z > 0.107$ for Ly β , $z > 0.167$ for Ly γ , and $z > 0.195$ for Ly δ . In this survey we only report on systems at $z \geq 0.24$.

2.1. Measuring N_{HI} from Lyman Lines and Lyman-Edge

In a HST/COS survey of H I column densities in the low-redshift IGM along 82 AGN sight lines, Danforth et al. (2016) found 2577 distinct H I absorption systems, some of them single-line (Ly α) systems. For statistical analysis, they defined a “uniform sample” of 2256 systems in which N_{HI} was found by multi-line CoG analysis, using either (Ly α + Ly β) or (Ly β + Ly γ) at a minimum for $\log N_{\text{HI}} \geq 13.5$, and Ly α alone for well-measured weaker lines. Of these 2256 absorbers, 65 had column densities $N_{\text{HI}} \geq 10^{15}$ cm⁻². These column densities were determined by a traditional CoG, which works best for absorption lines that are unsaturated or mildly saturated. At $N_{\text{HI}} < 10^{13.5}$ cm⁻², IGM surveys typically rely on Ly α absorbers, since Ly β is too weak to detect at typical COS sensitivity (15–20 mÅ equivalent widths). When higher Lyman lines become available at higher z and greater N_{HI} , the CoG yields reliable parameters (N, b).

Once the Lyman lines become strongly saturated, with equivalent widths on the “flat portion” of the CoG, the inferred column densities are more uncertain. The onset of saturation is gauged by the line-center optical depth, $\tau_0 = (\pi e^2 / m_e c) (N f \lambda / \pi^{1/2} b)$, where $b = (25 \text{ km s}^{-1}) b_{25}$ is a typical doppler parameter. For the first four Lyman lines, these optical depths are

$$\begin{aligned} \tau_0(\text{Ly}\alpha) &= (30.3) N_{15} b_{25}^{-1} & \tau_0(\text{Ly}\beta) &= (4.86) N_{15} b_{25}^{-1} \\ \tau_0(\text{Ly}\gamma) &= (1.69) N_{15} b_{25}^{-1} & \tau_0(\text{Ly}\delta) &= (0.793) N_{15} b_{25}^{-1} \end{aligned}$$

for N_{HI} scaled to $(10^{15} \text{ cm}^{-2}) N_{15}$. As long as some Lyman lines remain near the linear portion of the CoG, this method works well. For $b \approx 25 \text{ km s}^{-1}$, the Ly α line begins to saturate ($\tau_0 > 1$ at $\log N_{\text{HI}} > 13.5$) producing large uncertainties at $14.5 < \log N_{\text{HI}} < 16.5$.

In this paper, we focus on the stronger H I absorbers, using their Lyman decrements to derive accurate column densities over the range $16.2 \leq \log N_{\text{HI}} \leq 17.85$. With our Lyman-comb technique and $S/N \geq 10$, we can detect the Lyman decrement at optical depths $\tau_{\text{LL}} \geq 0.1$ corresponding to $\log N_{\text{HI}} \geq 16.2$. Once $\log N_{\text{HI}} \geq 17.85$ ($\tau_{\text{LL}} > 4.46$) it becomes difficult to detect transmitted flux in the Lyman continuum. In a few cases with high S/N ($\gtrsim 20$) we detected or limited the residual flux transmission equivalent to $\tau_{\text{LL}} \geq 5.0$ ($\log N_{\text{HI}} \geq 17.9$). For high column density systems, we can constrain N_{HI} from damping wings in the Ly α line, when present (Ly α shifts out of the COS/G160M band at $z \gtrsim 0.47$.) By combining the Lyman decrement (for $\log N_{\text{HI}} > 16.2$) with CoG methods on higher Lyman lines, typically up to Ly12 and occasionally to Ly15, we obtain more accurate column densities than with CoG alone.

The CoG fitting uses a series of Voigt profiles convolved with an appropriate COS line spread function². Widely separated velocity components are identified semi-automatically (see Danforth et al. 2016), but closely blended components require interactive iden-

² www.stsci.edu/hst/cos/performance/spectral_resolution

tification and fitting. We compare the models to the observed spectrum in normalized flux space via a χ^2 minimization package MPFIT (Markwardt 2009) with equivalent widths fitted to line profiles of each component (not to the observed flux). Moderately saturated lines with simple component structure are well constrained by this method, and the CoG gives much better (N, b) solutions for H I than a single-line profile fit.

Figures 5–8 illustrate our technique for Lyman-series and Lyman decrement absorption for two LLS with $\log N = 17.85 \pm 0.02$ and $\log N = 17.67 \pm 0.10$ and two pLLS absorbers with $\log N_{\text{HI}} = 16.41 \pm 0.03$ and 17.01 ± 0.05 . The presence of a Lyman decrement typically yields $\log N_{\text{HI}}$ accurate to ± 0.05 or better. Figure 9 shows spectra of the other eight strong H I absorbers with $\log N_{\text{HI}} > 17.0$. Strong H I absorbers are often composed of multiple, blended components. Lower-order Lyman lines are typically too strong to see blended components, but higher-order lines can reveal their presence. Absorbers where the minimized χ^2 solution fails to match the data may harbor unresolved component structure. For example, in the strong absorber toward SBS 1108+560 (Figure 5), a weaker component is seen in the blue wing of Ly ϵ and higher lines. When blended components are present, we fit a CoG to each component, using only lines in which they are unambiguously separable, eliminating lines contaminated with airglow emission or unrelated absorption. Line profiles and total column densities for the combined solution (e.g., N_1, b_1, z_1 and N_2, b_2, z_2) are then calculated and compared qualitatively to the stronger, lower-order Lyman lines. In several cases, the CoG solution does not reproduce the observed line profiles, or it differs from the Lyman decrement. The CoG is determined from the measured equivalent widths of the lines. Sometimes a solution with a smaller b and larger N (or vice versa) is required to match the observed line profiles or decrement.

2.2. Lyman line overlap and velocity components

The CoG techniques generally give accurate results with the availability of higher Lyman lines. However, line overlap sets in at Ly15 ($\lambda = 915.329$ Å) or Ly16 ($\lambda = 914.919$ Å) as the higher Lyman series converges on the Lyman limit at $\lambda_{\text{LL}} = 911.753$ Å. Line crowding and uncertain continuum placement make measurements of equivalent widths difficult when the wavelength separation, $\Delta\lambda_{n,n+1}$, between sequential Lyman lines is comparable to their line width. Table 2 shows line separations and line-center optical depths for Ly12 - Ly24, scaled to the ratio, N_{17}/b_{25} , for column densities $N_{\text{HI}} = (10^{17} \text{ cm}^{-2})N_{17}$. The lines are distinguishable up to Ly15, where $\Delta\lambda_{n,n+1} \approx 0.5$ Å. For Gaussian line profiles, the full width at half maximum is $\Delta\lambda_{\text{FWHM}} = 2(\ln 2)^{1/2}(\Delta\lambda_D) \approx (0.127 \text{ Å}) b_{25} \lambda_{914}$, where λ_{914} is a typical (L15 - Ly20) wavelength in units of 914 Å and $\Delta\lambda_D = \lambda_0(b/c)$ is the doppler width. Severe overlap sets in above Ly20, where separations become less than 0.2 Å. At this point, higher Lyman lines overlap in their wings, 10% below the continuum, defined by width $\Delta\lambda_{10\%} = 2(\ln 10)^{1/2}(\Delta\lambda_D) \approx (0.231 \text{ Å}) b_{25} \lambda_{914}$. A few absorbers have $b = 40 - 50 \text{ km s}^{-1}$, with wing overlap

affecting Ly 14 - Ly17 at line separations of 0.4 - 0.5 Å.

Overlap creates difficulties in measuring equivalent widths, with offsetting effects of shared line absorption and continuum placement. Multiple velocity components complicate the problem further, and a proper treatment requires multi-line radiative transfer. Therefore, we do not include lines above Ly15 in our analysis, as illustrated in Figure 10 for the absorber toward PKS0552-640. The standard CoG up to Ly15 gives $\log N_{\text{HI}} = 17.01 \pm 0.05$, whereas including additional (overlapping) lines from Ly16 to Ly24 gives an erroneous fit with $\log N_{\text{HI}} = 16.81 \pm 0.02$. In this case, the observed Lyman decrement provides an accurate column density, $\log N_{\text{HI}} = 17.01 \pm 0.03$, verifying the CoG solution up to Ly15.

Appendix A provides narrative discussion for our analysis of 73 strong H I absorbers with $\log N_{\text{HI}} > 15.75$. For several absorbers with $\log N_{\text{HI}} > 16.25$, our combination of CoG fits and Ly decrement measurements uncovered a few discrepancies with previous values in the literature (Lehner et al. 2013; Fox et al. 2013; Stevans et al. 2014). For four systems with well-resolved velocity components separated by 150-200 km s $^{-1}$ or greater, we treated the components as separate absorbers: Systems #24abc, #47abc, #59ab, and #60ab.

3. RESULTS

To analyze the bivariate distribution, $f(N, z)$, of H I absorbers, we group them into a binned array, $F(i, j)$, shown in Table 3, with redshift indices ($i = 1 - 15$) and column density indices ($j = 1 - 15$). The 15 redshift bins have equal width $\Delta z = 0.04$ from $z = 0.24 - 0.84$. The first 12 column-density bins have width $\Delta(\log N_{\text{HI}}) = 0.25$ spanning $14 < \log N_{\text{HI}} \leq 17$. The last three bins ($j = 13, 14, 15$) are wider and cover the 10 strongest absorbers with $\log N_{\text{HI}} = 17.0 - 20.5$. As shown in Table 1 (column 4), the higher Lyman lines (Ly γ , Ly δ , Ly ϵ) are easily detectable, at 50 mÅ equivalent width, for column densities $\log N_{\text{HI}} \geq 14.3 - 14.9$. Because the best COS data have S/N > 20, we have regularly detected the first three Lyman lines (Ly α , Ly β , Ly δ) and often even higher Lyman lines (Figure 3). This allows us to identify absorbers with $\log N_{\text{HI}} = 14 - 15$, even though the Lyman edge is undetectable at these column densities. The LLS and stronger pLLS absorbers with $\log N_{\text{HI}} > 16.5$ are typically observed in higher Lyman lines up to Ly12 and often beyond (see Figures 5–9), and they yield precise H I column densities via CoG. At higher redshifts, the two strongest Lyman lines move out of the G160M window (Ly α at $z > 0.47$ and Ly β at $z > 0.75$). Because our higher redshift H I detections rely on Ly γ and higher lines, we could miss a few absorbers with $\log N_{\text{HI}} = 15.0 - 15.5$. Column densities for strong absorbers can sometimes be influenced by velocity components. In well-exposed COS spectra, we can identify components with $\Delta v = 40 - 400 \text{ km s}^{-1}$, all of which contribute to the Lyman decrement. We derive individual column densities with multi-component CoGs, which could affect absorber counts for the bins between $\log N_{\text{HI}} = 14.75 - 16.00$. We have taken a conservative approach, only splitting the velocity components in four well-separated systems with $\Delta v \geq 150 - 200 \text{ km s}^{-1}$.

The observed distribution in column density (Table 3) exhibits the expected falloff in numbers at high column

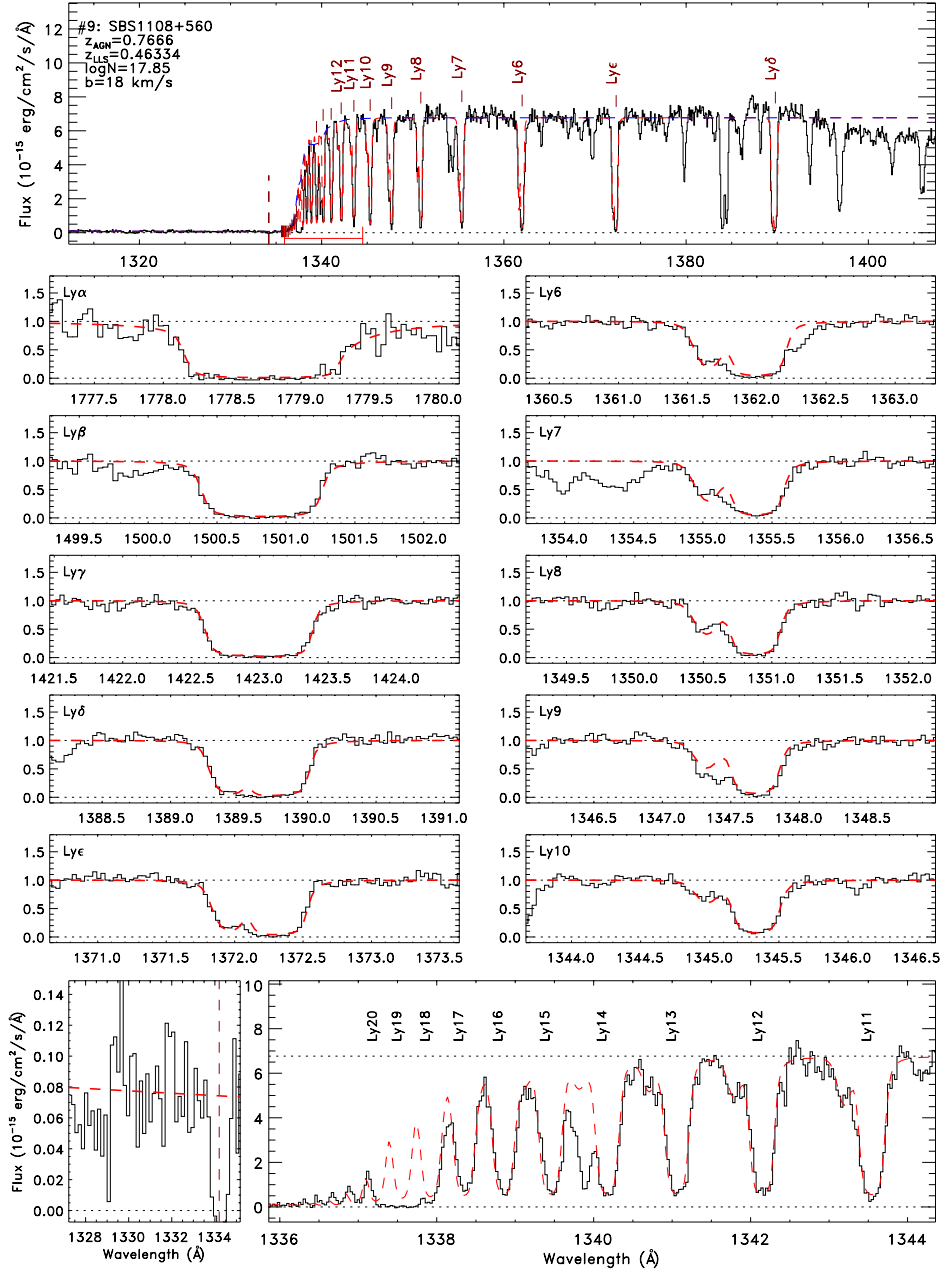


FIG. 5.— (Top) Normalized COS/G130M spectrum of SBS 1108+560 showing lines of System #9 at $z_{\text{abs}} = 0.46334$, a LLS with Lyman lines (Ly6 - Ly12) converging on LL at 1334.2 \AA (vertical red dashed line). Red dashed lines in spectrum show model with column density $\log N_{\text{HI}} = 17.85 \pm 0.02$ and doppler parameter $b = 18 \pm 2 \text{ km s}^{-1}$, not fits to individual lines. (Middle panels) Line profiles of Lyman lines (Ly α - Ly10). (Bottom) Higher Lyman lines (Ly11 - Ly20) and transmitted flux in LyC. Note C II $\lambda 1334.53$ interstellar absorption in the LyC (bottom left panel).

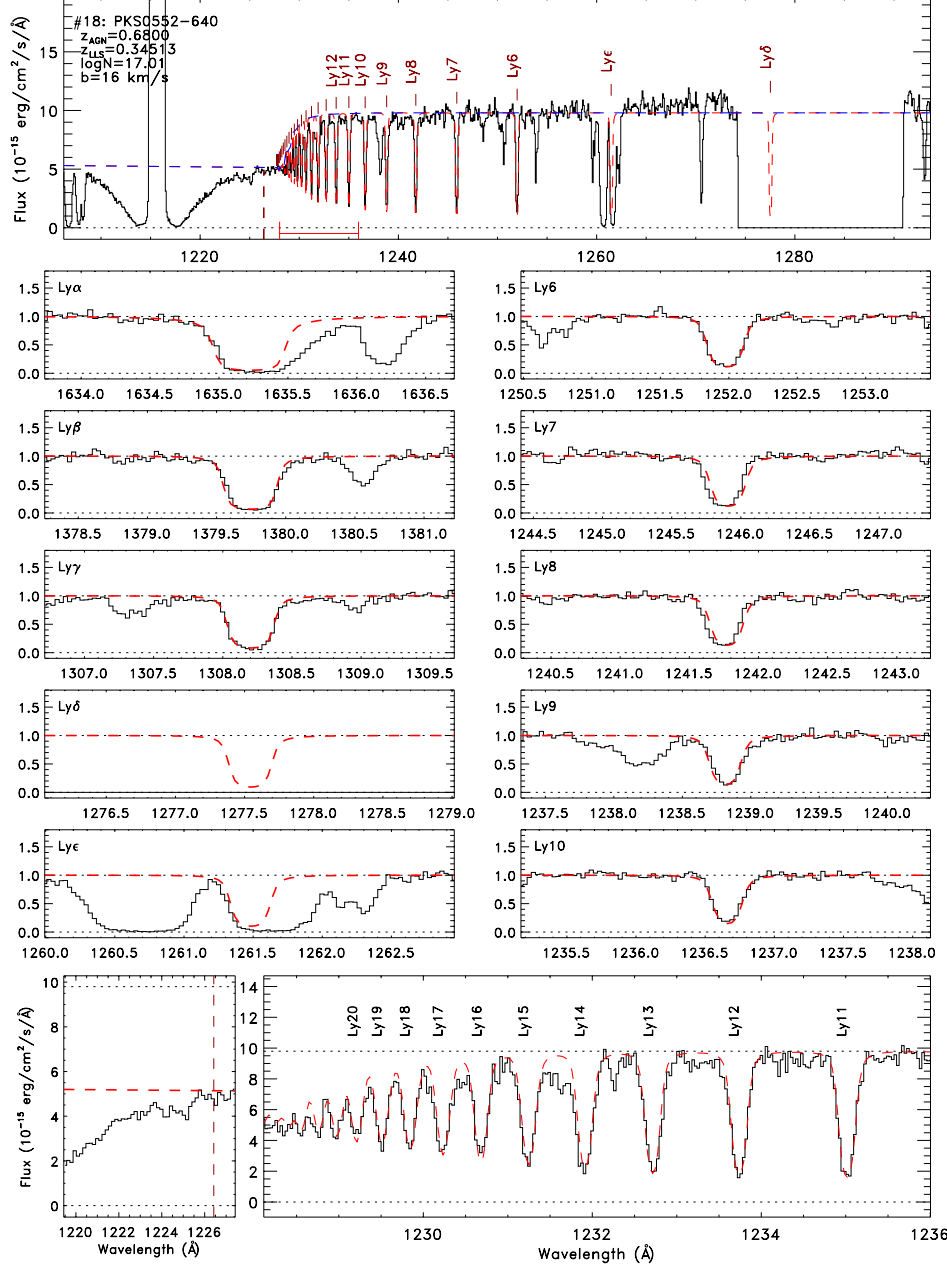


FIG. 6.— Same as Figure 5 for pLLS toward PKS0552-640 (System #18 at $z_{\text{abs}} = 0.34513$) with LL at 1226.4 Å. Redward wing of Galactic Ly α absorption extends from 1216-1226 Å. Red dashed lines in spectrum show profiles of Lyman lines (Ly α - Ly10) for model with $\log N_{\text{HI}} = 17.01 \pm 0.05$ and $b = 16 \pm 2$ km s⁻¹. (Bottom) Higher Lyman-series lines (Ly11 - Ly20) and transmitted flux in LyC above the Galactic DLA.

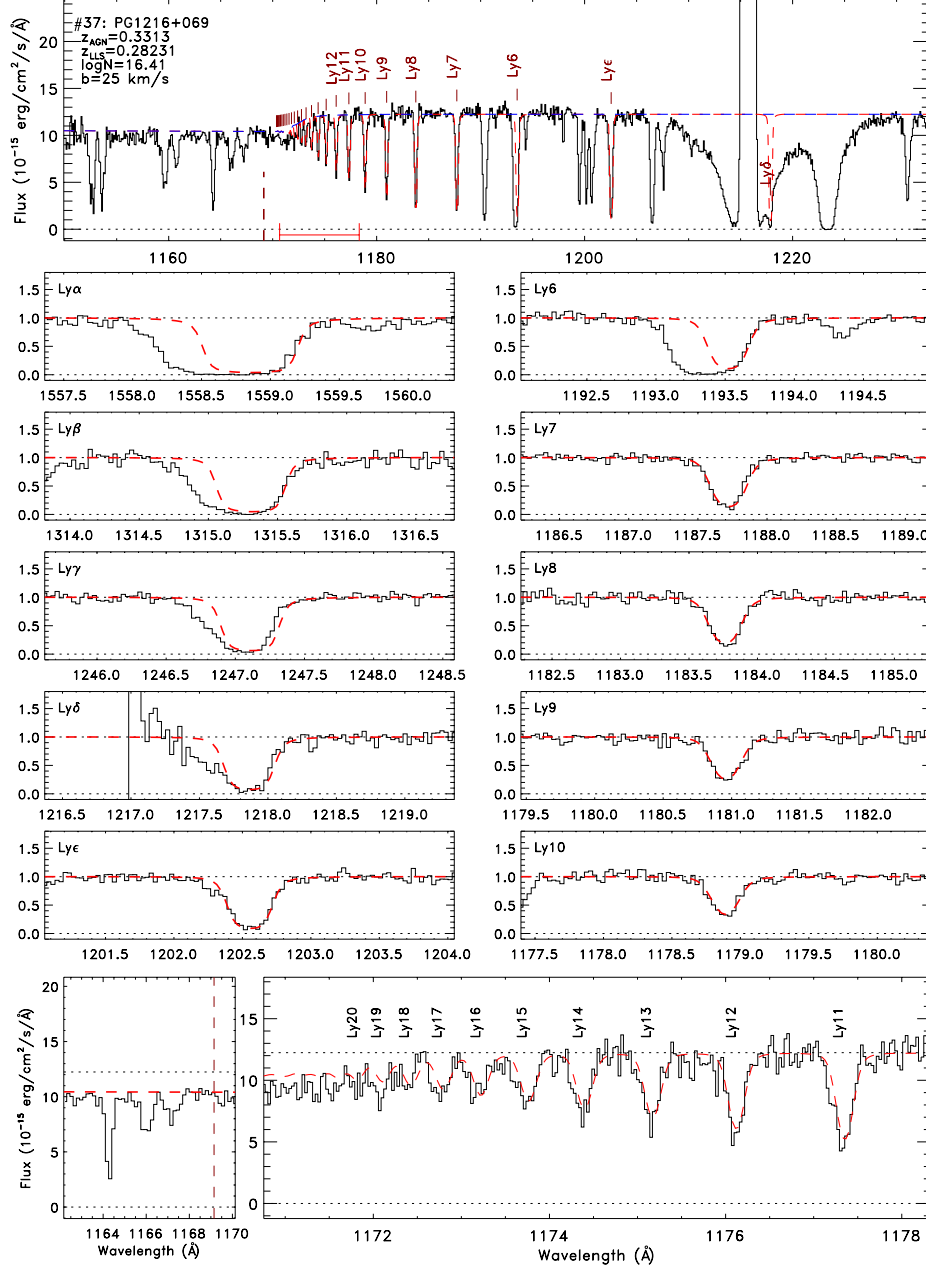


FIG. 7.— Same as Figure 5 for pLLS toward PG 1216+069 (System #37 at $z_{\text{abs}} = 0.28231$). Absorption lines converge on LL at 1161.15 Å. Red dashed lines (Ly ϵ - Ly10) show strongest component fitted to CoG with $\log N_{\text{HI}} = 16.41 \pm 0.03$ and $b = 25 \pm 5$ km s $^{-1}$. Lyman decrement gives $\tau_{\text{LL}} = 0.16 \pm 0.02$ or $\log N_{\text{HI}} = 16.40 \pm 0.06$. (Bottom) Higher Lyman lines (Ly11 - Ly20) and transmitted flux in LyC.

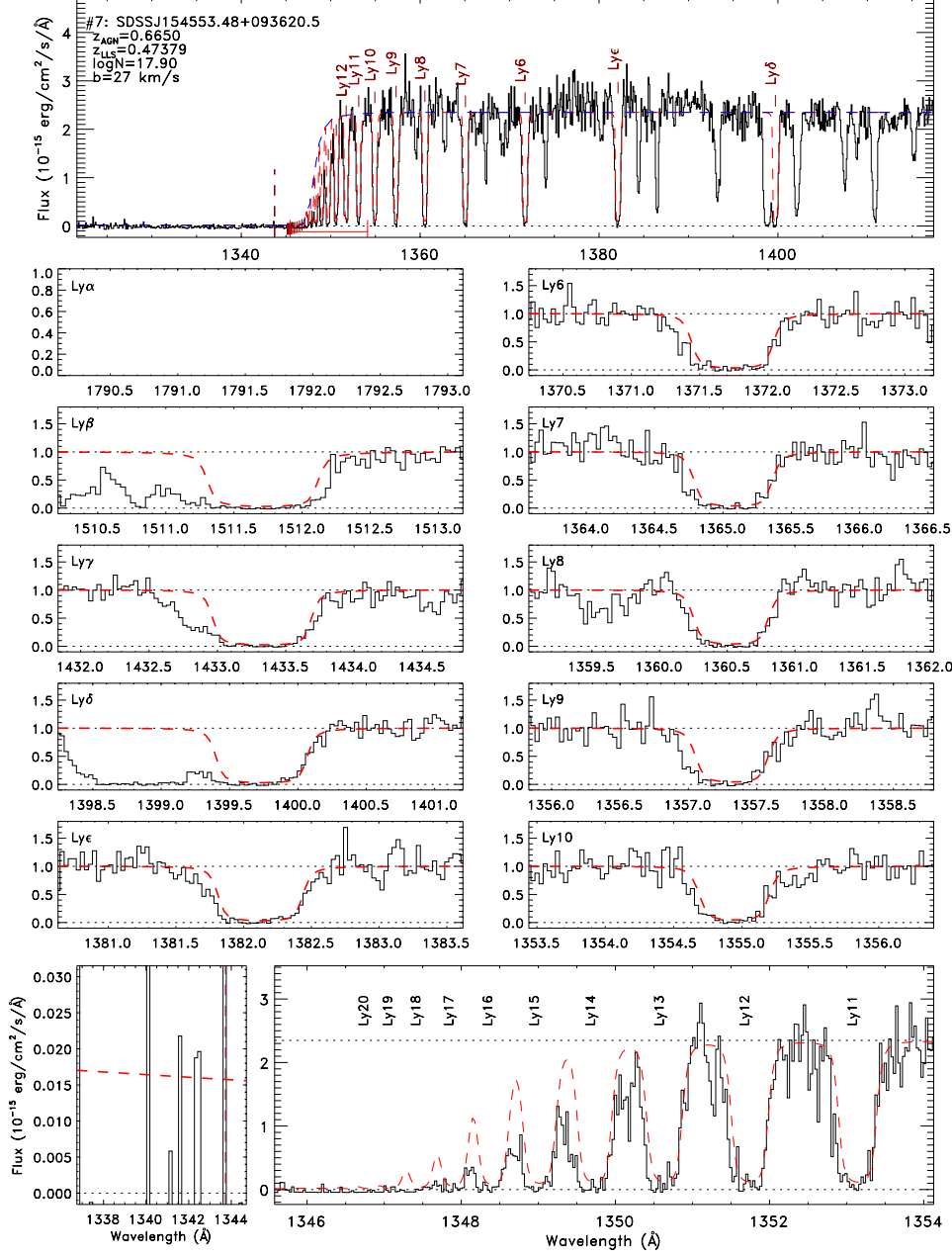


FIG. 8.— Same as Figure 5 for LLS toward SDSS J154553.48+093620.5 (System #7 at $z_{\text{abs}} = 0.47379$). Absorption lines of Ly6 - Ly12 converge on LL at 1343.7 Å. Red dashed lines (Lyβ - Ly10) show strongest component fitted to CoG with $\log N_{\text{HI}} = 17.67 \pm 0.15$ and $b = 35 \pm 1$ km s⁻¹. This column density would give $\tau_{\text{LL}} = 2.95$ and transmitted flux of 5.25%, inconsistent with observations of flux below the LL (bottom panels) which imply $\log N_{\text{HI}} \geq 17.9$.

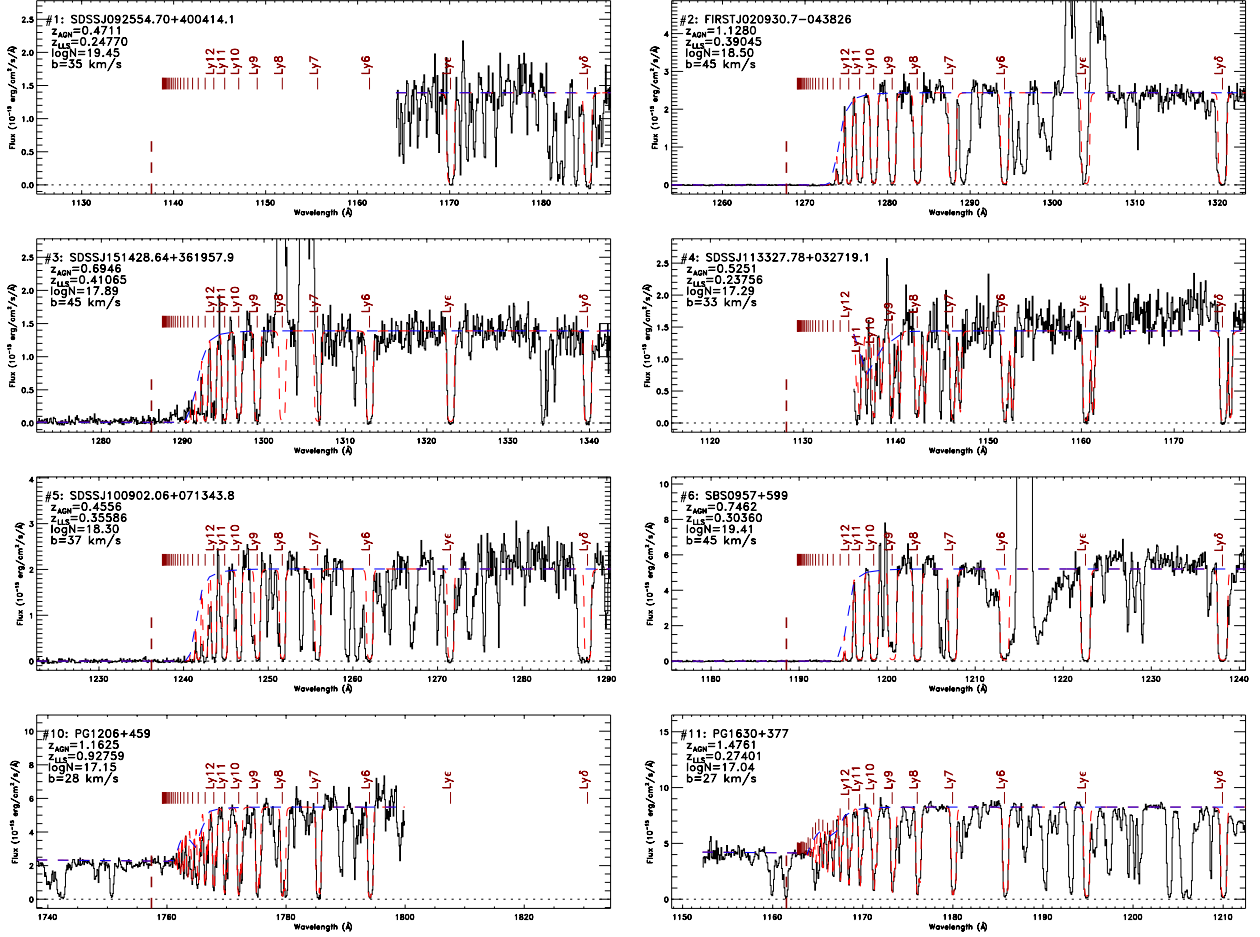


FIG. 9.— COS Spectra of eight strong H I absorbers ($\log N_{\text{HI}} > 17.0$), listed in Appendix A as systems #1–6, #10, #11 (see labels in top-left corner). These include six LLS and two pLLS ($\log N_{\text{HI}} = 17.15$ and 17.04). Other strong absorbers were shown in Figures 4, 5, and 7. Spectra for Systems #1 and #10 are limited by cutoffs of the settings of the G130M and G160M gratings. Additional Lyman lines beyond those shown were available in many cases.

densities owing to their scarcity. We believe the decrease in absorber numbers in bins $j = 1 - 4$ ($\log N_{\text{HI}} = 14 - 15$) arises primarily from the lower detection sensitivity of weak Lyman lines at higher redshift. Because the LL is not detectable at $\log N_{\text{HI}} < 16.2$, we rely on finding a pattern of higher Lyman lines (Ly γ , Ly δ , Ly ϵ) whose detection in the G160M window requires $\log N_{\text{HI}} \geq 14.3 - 14.9$ (Table 1). These higher Lyman lines are easily detected in G130M (see Figure 3), but at $z > 0.5$ we rely on G160M and higher (weaker) lines in the Lyman series. For this reason, we focus our attention on pLLS and LLS absorbers with $\log N_{\text{HI}} \geq 16.0$. Our statistical analysis in Appendix B restricts the H I absorber sample to the range $0.24 \leq z_{\text{abs}} \leq 0.84$ and $15 \leq \log N_{\text{HI}} \leq 20$, where we feel confident in detecting most systems in AGN sight lines with well-exposed COS spectra ($S/N > 10$). Our LLS sample is restricted to $0.24 \leq z \leq 0.48$, as described in Section 3.3. This technique differs from that in our re-

cent IGM survey (Danforth et al. 2016), which detected primarily weak H I absorbers through Ly α lines.

3.1. Redshift Coverage per Bin

The total (effective) redshift pathlength, $\Delta z_{\text{eff}}^{(\text{tot})}$, is found from the spectral coverage of the AGN in our survey. We chose redshift bins of width $\Delta z = 0.04$, starting at bin 1 ($0.24 < z < 0.28$) where the Lyman edge at wavelength $\lambda_{\text{LL}} = (911.753 \text{ \AA})(1+z)$ first falls within the range of most COS/G130M data (1134–1459 Å). Table 4 shows the number of AGN with sensitivity to detecting a LL in each redshift bin. Each AGN with redshift above the bin contributes pathlength $\Delta z = 0.04$, plus partial redshift coverage for a few AGN whose redshifts fall within the bin. The redshift-bin pathlengths, $\Delta z_{\text{eff}}^{(i)}$, are shown in column 5 of Table 4. To determine this redshift path, we subtracted a few spectral regions blocked by strong absorbers ($\log N_{\text{HI}} > 17$) along ten AGN sight

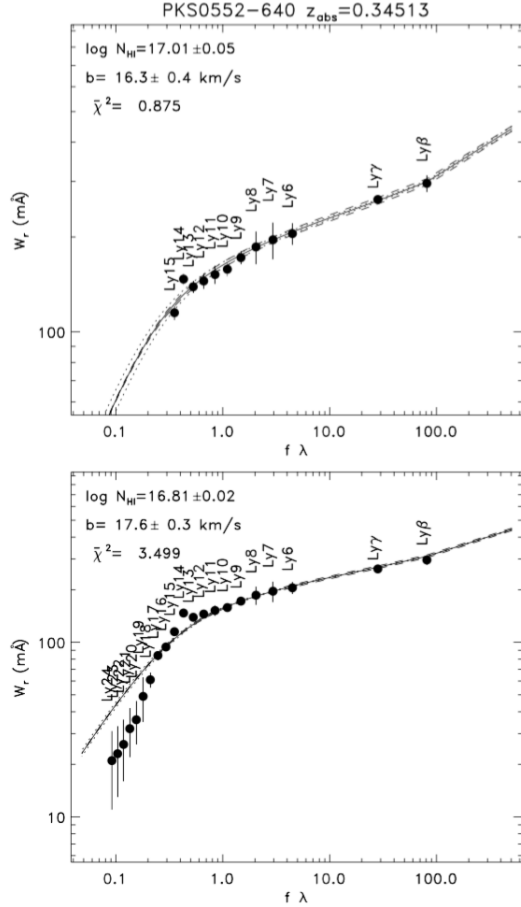


FIG. 10.— (Top) Curve of growth of the Lyman series (Ly β through Ly15) for pLLS toward PKS 0552-640 at $z_{\text{abs}} = 0.34513$ (see Figure 6). Equivalent widths (W_λ in mÅ), are plotted vs. line strengths, $f\lambda$, with oscillator strengths f and wavelengths λ (Å) from Morton (2003). The best fit gives $\log N_{\text{HI}} = 17.01 \pm 0.05$ with $b = 16.3 \pm 0.4$ km s $^{-1}$ (reduced χ^2 noted in header.) (Bottom) CoG including lines of Ly16 - Ly24. Line overlap and crowding result in reduced equivalent widths and an erroneous fit with $\log N_{\text{HI}} = 16.81 \pm 0.02$ and $b = 17.6 \pm 0.3$ km s $^{-1}$.

lines shown in Table 5. In practice, only a few of the strongest LLS absorbers, with $\log N_{\text{HI}} > 17.5$, produce significant blockage. Strong foreground absorption by the Galactic interstellar H I (Ly α) does not impact Δz_{eff} or the Lyman comb, since it usually blocks only one of the Lyman lines.

With the far-UV spectral coverage between 1134 Å and 1795 Å and availability of many lines in the Lyman series, we were able to detect strong H I systems between $z_{\text{abs}} = 0.237 - 0.928$. Because of the reduced spectral coverage of higher-redshift AGN, we limited our analysis to 15 redshift bins between $z = 0.24 - 0.84$. Sensitivity to higher Lyman lines declines at $z > 0.846$ as Ly γ shifts out of the COS/G160M band. The total pathlength in this sample (Table 4) is $\Delta z_{\text{eff}}^{\text{(tot)}} = 31.94$. For individual bins, the pathlength decreases from $\Delta z_{\text{eff}}^{(i)} = 3.83$ for bin 1 ($z = 0.26$ and $\lambda_{\text{LL}} = 1149$ Å) to $\Delta z_{\text{eff}}^{(i)} = 2.80$ for bin 5

($z = 0.42$ and $\lambda_{\text{LL}} = 1295$ Å). Although bin 5 covers the redshift ($z = 0.423$) at which Ly β shifts out of G130M, spectral overlap with G160M (1400–1459 Å) allows Ly β to be continuously observed to $z = 0.75$. The Lyman edge shifts out of G130M beyond bin 9 ($0.56 < z < 0.60$), and the AGN pathlength drops to $\Delta z_{\text{eff}}^{(i)} \approx 0.74 - 0.96$ in bins 13–15. With G160M, we have detected pLLS out to $z = 0.928$. Wavelength overlap between G130M and G160M gratings (1400–1459 Å) slightly enhances our ability for discovering Ly α absorbers at $z = 0.15 - 0.20$, Ly β absorbers at $z = 0.36 - 0.42$, and Ly γ absorbers at $z = 0.44 - 0.50$. However, this effect is minor. Because pLLS identification requires finding a pattern of several Lyman lines, our survey is most sensitive between $z \approx 0.24 - 0.84$.

Selection biases arise toward several high- z AGN that are less likely to contain strong LLSs and DLAs (see Sections 3.3 and 3.4). Our sample of 159 AGN (Stevans et al. 2014) contains 29 targets at $z > 0.70$ and 43 at $z > 0.60$, many of them observed previously by *IUE*, *HST*, and *FUSE*. To be detected in the G130M/G160M gratings, these AGN were “UV-qualified” for sufficient far-UV flux, usually by *GALEX* or *IUE*. A number of these AGN came from the COS-Halos project (Tumlinson et al. 2013) whose QSOs were selected to have high fluxes in the *GALEX* far-UV band and avoid strong Mg II absorbers at $z_{\text{abs}} > 0.4$.

3.2. Bivariate Distribution in $\log N$ and z

Table 6 lists 41 strong H I absorbers with $\log N_{\text{HI}} \geq 16.0$, classified as LLS or pLLS (systems #1-40 and #73 from Appendix A). The last columns compare our column densities to previous measurements from Lehner et al. (2013) and estimates from Stevans et al. (2014). The Lehner values are the same as those reported by Fox et al. (2013). Those from Stevans et al. (2014) were estimates, many of which were revised in this paper after careful analysis of CoGs and Lyman decrements. For 158 absorbers above our expected detection limit ($\log N_{\text{HI}} \geq 15.0$) the absorber frequency per redshift is $dN/dz \approx 4.95 \pm 0.39$ averaged over $0.24 < z < 0.84$. We see some indication of an increase in frequency with redshift. Figure 11 shows the distribution in column density for our pLLS data, together with the Ly α forest distribution from Danforth et al. (2016). Some offset is expected, as the COS Ly α forest survey covers $z < 0.47$ with median redshift $z_{\text{abs}} = 0.14$, whereas our pLLS survey spans $0.24 < z < 0.93$ with median $z_{\text{abs}} = 0.43$. The eight detected LLS range from $z = 0.237$ to 0.474 , with median redshift $z_{\text{abs}} = 0.39$. The absence of LLS at $z > 0.48$ is surprising statistically, as we expected to detect $3.6^{+3.1}_{-1.8}$ LLS between $0.48 < z < 0.84$ based on the derived redshift evolution (Section 3.3). This may be evidence for a bias toward AGN with high far-UV fluxes, unblocked by LLS at $z > 0.5$. We do not see this effect for the stronger pLLS with $\log N_{\text{HI}} = 16.5 - 17.0$. For pLLS statistics, we use the full redshift range ($0.24 \leq z \leq 0.84$) but restrict the LLS sample to bins 1–6 ($0.24 \leq z \leq 0.48$).

The Ly α forest and pLLS distributions match fairly well at $\log N_{\text{HI}} \geq 16$. A possible turnover in the pLLS distribution appears at $\log N_{\text{HI}} < 15.5$, which could mark the onset of survey incompleteness. Because of the small number of absorbers, one expects fluctuations in the

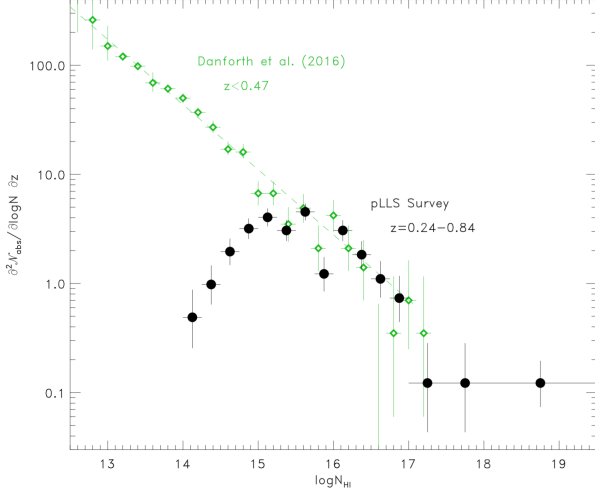


FIG. 11.— Distribution of H I absorbers in column density (per $\log N_{\text{HI}}$) over total redshift pathlength $\Delta z_{\text{eff}} = 31.94$ between $0.24 \leq z \leq 0.84$. Solid diamonds (green) are from the HST/COS survey (Danforth et al. 2016) of Ly α forest at $0 < z < 0.47$, and filled circles (black) show the current survey of pLLS and LLS at $0.24 < z < 0.84$. Green dotted line is a least-squares fit to the differential distribution, $f(N, z) \propto N^{-\beta}$, with $\beta = 1.60 \pm 0.02$.

range $\log N_{\text{HI}} = 15.0 - 16.0$ (bins $j = 5 - 8$ in Table 3). The two surveys agree for bin 7 (15.50–15.75) and bin 9 (16.00–16.25), whereas bin 8 (15.75–16.00) has a low number of absorbers that may arise from the finite spacings in our survey grid, $\Delta z = 0.04$, $\Delta(\log N_{\text{HI}}) = 0.25$. As noted above and in Table 1, we should be able to identify most absorbers between $15.0 < \log N_{\text{HI}} < 15.5$. However, a small decrease in detection efficiency of weak absorbers could occur at $z > 0.47$, when Ly α shifts out of the G160M window. The absorber numbers in bins 6–9 could also be affected by velocity components within strong systems, which separate into distinct absorbers. The distinction between “systems” and “components” is a subtle one that we have not pursued beyond the obvious cases in Systems #24abc, #47abc, #59ab, and #60ab (see Appendix A).

To analyze the bivariate differential distribution of absorbers in H I column density and frequency, we have applied a maximum-likelihood analysis (Appendix B) to the parameterized form $f(N, z) \equiv d^2N/dz dN_{\text{HI}} = C_0 N_{\text{HI}}^{-\beta} (1+z)^\gamma$. We fitted all absorbers in the ranges $0.24 \leq z \leq 0.84$ and $15 \leq \log N_{\text{HI}} \leq 20$, using Monte-Carlo Markov-Chain (MCMC) simulations to derive values $\beta = 1.48 \pm 0.05$ and $\gamma = 1.14^{+0.88}_{-0.89}$. Figure 12 shows the 2D joint probability distributions in power-law parameters and their 1σ error bars. Both distributions are close to Gaussian, although the column-density distribution is much better constrained (3.4% error in β) than the redshift evolution index, γ . The uncertainty in γ is illustrated in Figure 13 with a histogram of the redshift distribution from $z = 0.24 - 0.84$. This evolution index is similar to those determined in our Ly α survey (Danforth et al. 2016). Over redshifts $0 < z < 0.47$, we found $\gamma_{\text{all}} = 1.24 \pm 0.04$ for all absorbers with $\log N_{\text{HI}} > 13$. Refitting the distribution of 65 absorbers at $\log N_{\text{HI}} \geq 15.0$, we find $\gamma = 1.43 \pm 0.34$.

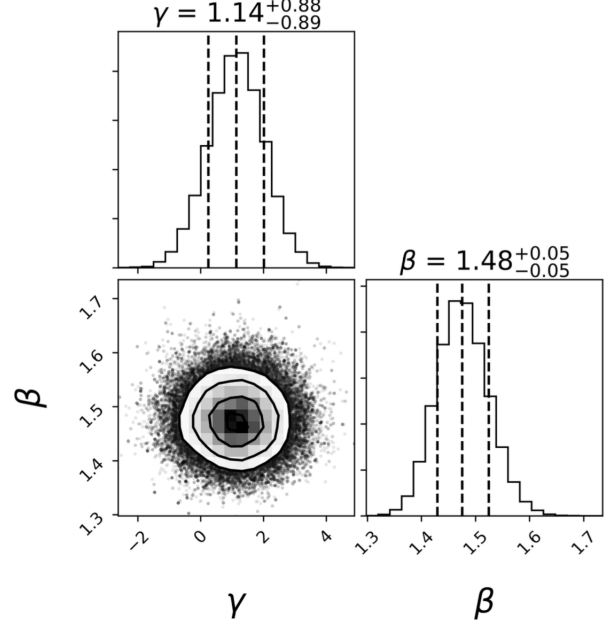


FIG. 12.— Parameterized evolution of the distribution of H I absorbers in column density and redshift, $f(N, z) = C_0 N^{-\beta} (1+z)^\gamma$, from Monte-Carlo Markov Chain (MCMC) samples for power-law parameters. Lower-left panel plots the 2D joint-probability of γ and β , and other panels show the marginalized distributions with median and 1σ bounds marked by dashed lines.

The normalization (C_0) of our (MCMC) distribution follows from integrating over observed (and fitted) ranges in redshift ($z_1 < z < z_2$) and column density ($N_1 < N_{\text{HI}} < N_2$),

$$N_{\text{tot}} = C_0 \int_{z_1}^{z_2} (1+z)^\gamma \Delta z_{\text{eff}}(z) dz \int_{N_1}^{N_2} N_{\text{HI}}^{-\beta} dN_{\text{HI}} \\ = (4.11 \times 10^{-6}) C_0. \quad (2)$$

In evaluating the integral over column density, we take $N_1 = 10^{15} \text{ cm}^{-2}$, $N_2 = 10^{20} \text{ cm}^{-2}$, and $\beta = 1.48$ to give 1.31×10^{-7} . The redshift integral gives 0.983, for $z_1 = 0.24$, $z_2 = 0.84$, $\gamma = 1.14$, and assuming $\Delta z_{\text{eff}}(z)$ to be constant across the full redshift range with pathlength $\Delta z_{\text{eff}}^{\text{(tot)}} = 31.94$. Thus, we find $C_0 = 3.87 \times 10^7$ for $N_{\text{tot}} = 159$ absorbers. If we weight $f(N, z)$ by the effective pathlengths, $\Delta z_{\text{eff}}(z_i)$, of the 15 individual redshift bins (Table 4), we find a slightly larger normalization, $C_0 = 4.12 \times 10^7$. We adopt $C_0 = 4 \times 10^7$ for $N(\text{cm}^{-2})$.

3.3. True Lyman-Limit Systems

By convention, true LLS are defined as absorbers with $\tau_{\text{LL}} \geq 1$ or $\log N_{\text{HI}} \geq 17.2$. Although most surveys follow this definition, several recent papers included pLLS absorbers with lower column densities in their lists. Because of the scarcity of low-redshift LLS, extending the definition of LLS into the pLLS range creates samples with better statistics. In our survey, we retain standard definitions of LLS and pLLS ($16.0 < \log N_{\text{HI}} < 17.2$) and analyze a total of 158 H I absorbers with $\log N_{\text{HI}} \geq 15.0$ between $z = 0.237 - 0.928$. Of these, eight are true LLS, one is a DLA ($\log N_{\text{HI}} = 20.34 \pm 0.12$) and 54 are

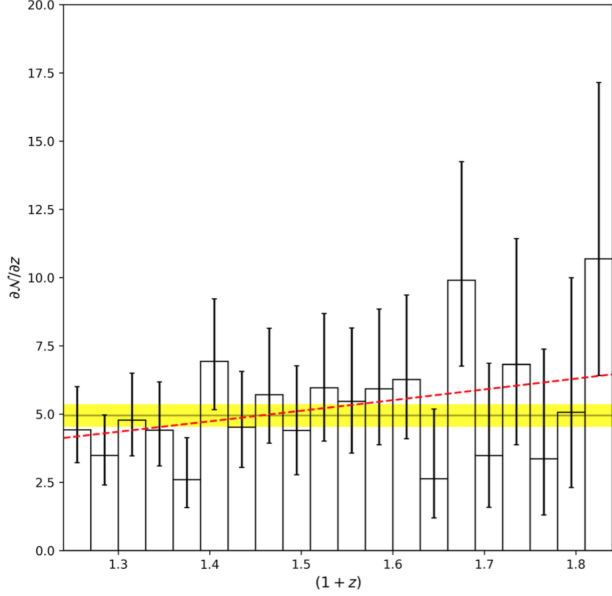


FIG. 13.— Parameterized evolution of the number of H I absorbers per unit redshift, dN/dz , for $z = 0.24 - 0.84$, integrating $f(N, z) = C_0 N^{-\beta} (1+z)^\gamma$ over $15 \leq \log N_{\text{HI}} \leq 20$. The MCMC realizations yield a fit with considerable uncertainty in index $\gamma = 1.14^{+0.88}_{-0.89}$. Horizontal (yellow) band shows the average line frequency, $\langle dN/dz \rangle = 4.95 \pm 0.39$, and red-dashed line is the MCMC fit with $\gamma = 1.14$. Histogram shows measured number of absorbers per unit redshift in 20 equal bins with error bars determined according to Poisson statistics. A non-integer number of absorbers may contribute to bin values because uncertainty in N_{HI} measurements can place a portion of an absorber's probability density outside the range used in fit.

pLLS. This *HST*/COS survey is one of the largest samples of strong H I absorbers at low redshift (full range from $0.237 \leq z \leq 0.928$). The eight LLS are detected through their Lyman decrements and in multiple Lyman lines using the COS G130M/160M gratings with resolution $R \approx 17,000$. The eight LLS in our COS survey are distinct from those in the FOS study, and they range from $z_{\text{abs}} = 0.2374 - 0.4738$ with median redshift $z_{\text{abs}} = 0.39$. Extrapolating the pLLS distribution (Section 3.2) into the LLS regime, we expect a frequency,

$$\left(\frac{dN}{dz} \right)_{\text{LLS}} = C_0 (1+z)^\gamma \int_{N_1}^{N_2} N^{-\beta} dN \approx 0.44 (1+z)^\gamma, \quad (3)$$

for $C_0 = 4 \times 10^7$ and $\beta = 1.48$. For $\gamma = 1.14$, the predicted number of LLS over the full survey, with $\Delta z_{\text{eff}} = 31.94$ for $0.24 \leq z \leq 0.84$, would be $N_{\text{LLS}} = 13.8^{+4.8}_{-3.8}$, larger than the observed 7 (or 8) LLS. We found no LLS in redshift bins 7–15 ($0.48 \leq z \leq 0.84$), whereas we would expect statistically to observe $N_{\text{LLS}} = 3.6^{+3.1}_{-1.8}$. For the restricted LLS range ($0.24 \leq z \leq 0.64$) in which the Lyman edge falls at $\lambda < 1495 \text{ \AA}$, the observed pathlength $\Delta z_{\text{eff}} = 26.82$ over bins 1–10. We would then expect to observe $N_{\text{LLS}} = 7.2^{+3.8}_{-2.8}$, in agreement with our survey numbers. This deficit suggests that some of the “high-redshift” ($z > 0.5$) AGN sight lines in our sample are biased *against* finding strong LLS and DLAs that block

their far-UV flux in the most sensitive portion ($1420 - 1650 \text{ \AA}$) of the *GALEX* far-UV band often used in QSO target selection. Many of these AGN have been studied with previous UV spectrographs (*IUE*, *FUSE*, *HST*) based on their far-UV brightness. Although we found no LLS between $0.48 \leq z \leq 0.84$, these AGN sight lines do contain strong pLLS absorbers ($16.5 \leq \log N_{\text{HI}} \leq 17.2$) in the expected numbers. Thus, the AGN bias may only affect the statistics for stronger LLS with $\tau_{\text{LL}} > 2$.

To guard against potential LLS bias at $z > 0.5$, we restrict our LLS sample to $z \leq 0.48$ and analyze the seven LLS in bins 1–6 over surveyed pathlength $\Delta z_{\text{eff}} = 19.24$. This leads to a LLS frequency, $dN/dz = 0.36^{+0.20}_{-0.13}$, at the median $z_{\text{LLS}} = 0.39$. Translating to standard form, $dN/dz = N_0 (1+z)^\gamma$, this frequency corresponds to $N_0 = 0.25^{+0.13}_{-0.09}$, after dividing by $(1+z)^\gamma \approx 1.46$ at the median redshift with $\gamma = 1.14$. This LLS frequency is in agreement with previous studies (see Table 7 for a summary). We begin with the *HST*/FOS Key Project survey of QSO absorption lines at $0.4 < z < 1.4$ (Bahcall et al. 1993). The LLS in that sample were analyzed in two papers that parameterized the redshift evolution. Storrie-Lombardi et al. (1994) found $dN/dz = (0.27^{+0.20}_{-0.13})(1+z)^{1.55 \pm 0.45}$ based on seven LLS observed by FOS at $0.456 < z < 1.036$ with median redshift $z_{\text{abs}} = 0.649$. Using the same seven LLS, Stengler-Larrea et al. (1995) found $dN/dz = (0.25^{+0.17}_{-0.10})(1+z)^{1.50 \pm 0.39}$. In a recent survey of strong absorbers at $z < 2.6$, Ribaud et al. (2011a) analyzed 206 LLS and pLLS absorbers with low-resolution gratings ($R \approx 1000$) on STIS (G140L, G230L) and FOS (G140L). Most of the H I absorbers in that survey were at $z > 1$; Table 4 in their paper lists five absorbers at $z < 0.5$ (3 true LLS) and 22 absorbers at $z < 0.84$ (17 LLS). From their LLS sample with $\tau_{\text{LLS}} \geq 1$, they fitted the evolution to $dN/dz = (0.28)(1+z)^{1.19 \pm 0.56}$ over $0.25 < z < 2.59$. In general, the number of low-redshift ($z < 1$) LLS reported in the literature is small, with just seven LLS in the *HST*/FOS Key Project and eight in our *HST*/COS survey (these 8 are distinct from those seen with FOS). We are also aware of three LLS at $z < 0.24$, found by the *FUSE* satellite in the far-UV:

PHL 1811 ($z_{\text{abs}} = 0.080923$) $\log N_{\text{HI}} = 17.98 \pm 0.05$ (Jenkins et al. 2005)

PKS 1302-102 ($z_{\text{abs}} = 0.09487$) $\log N_{\text{HI}} = 17.2 \pm 0.2$ (Cooksey et al. 2008)

PKS 0312-77 ($z_{\text{abs}} = 0.2028$) $\log N_{\text{HI}} = 18.22^{+0.19}_{-0.25}$ (Lehner et al. 2009)

We return to the observed deficit of LLS at $z > 0.48$, below the expected numbers given the fitted line frequency. The COS-Halos survey (Tumlinson et al. 2013) selected 39 UV-bright QSOs (*GALEX* far-UV magnitudes < 18.5) with median redshift $z_{\text{AGN}} = 0.525$. They avoided QSOs with strong (equivalent width $> 1 \text{ \AA}$) Mg II absorbers at $z > 0.4$ and advise that their QSOs at $z > 0.4$ are not expected to provide an unbiased sample of LLS. Our sample of 102 AGN with $z_{\text{AGN}} \geq 0.24$ includes 37 targets from the COS-Halos sample: 20 at $z_{\text{AGN}} > 0.5$, 14 at $z_{\text{AGN}} > 0.6$, and 9 with $z_{\text{AGN}} = 0.713 - 0.887$. We also have seven UV-bright (Palomar-Green) quasars observed with *IUE* (Tripp et al. 1994): PG 1407+265 ($z = 0.946$), PG 1148+549 ($z =$

0.975), PG 1206+459 ($z = 1.1625$), PG 1338+416 ($z = 1.21422$), PG 1522+101 ($z = 1.32785$), Q 0232-042 ($z = 1.437$), PG 1630+377 ($z = 1.476$). Our sample includes several UV-bright AGN (e.g., SBS 1108+560 at $z = 0.766619$, SBS 1122+594 at $z = 0.8514$) from the *HST* GTO Program and Guest Investigator Programs 11248, 11264, 11585, 11598, 11741, with diverse scientific goals including intergalactic absorbers (Danforth et al. 2016), high-redshift absorbers (Tripp et al. 2011; Ribaud et al. 2011b), galaxy-quasar pairs (Keeney et al. 2006; Crighton et al. 2010; Meiring et al. 2011; Tumlinson et al. 2013; Stocke et al. 2013; Bordoloi et al. 2014), and interstellar high-velocity clouds (Shull et al. 2009). Several of these high- z AGN were selected to study intervening Ne VIII absorbers and the hot phase of the IGM (Narayanan et al. 2011; Tripp et al. 2011; Savage et al. 2011; Meiring et al. 2013; Hussain et al. 2015).

Our derived LLS coefficient, $N_0 = 0.25^{+0.13}_{-0.09}$, is consistent with previous values (Table 7) from low-resolution *HST* surveys with FOS and STIS. Our fit to pLLS redshift evolution over $0.24 < z < 0.84$ gives $\gamma_{\text{pLLS}} = 1.14^{+0.88}_{-0.89}$, consistent with estimates noted above (Storrie-Lombardi et al. 1994; Stengler-Larrea et al. 1995; Ribaud et al. 2011a). However, the *HST* surveys are all based on small numbers of LLS with different redshift coverages. The median LLS redshifts are $z = 0.65$ for the seven FOS Key Project absorbers and $z = 0.39$ for the eight LLS studied by COS. The Ribaud et al. (2011a) survey was dominated by systems at $z > 1$, with only three LLS at $z \leq 0.5$. Thus, the redshift evolution of LLS and pLLS remains uncertain. Our best fit, $\gamma_{\text{pLLS}} = 1.14$, is similar to the value $\gamma_{\text{LF}} = 1.24 \pm 0.06$ (Danforth et al. 2016) for weak Ly α forest absorbers and also to that, $\gamma_{\text{LLS}} = 1.19 \pm 0.56$ (Ribaud et al. 2011a) fitted to the LLS ($\tau_{\text{LLS}} \geq 1$) absorbers at $z < 2.6$ in low-resolution FOS and STIS spectra. Differences in N_0 inferred from extrapolating $f(N, z)$ could be used to detect a turnover in the power-law slope (β) at $\log N > 17$. However, the number of low- z LLS absorbers is currently too small to provide reliable statistics. Obviously, larger UV surveys of LLS and pLLS that cover a wider range of redshifts would have greater leverage for determining the evolution index γ .

Accurate values of pLLS/LLS evolution out to $z \approx 2$ are also important for assessing the far-UV opacity to intermediate-redshift AGN, as we discuss in Section 3.5. The scarcity of strong absorbers ($\log N_{\text{HI}} > 16.5$) results in large fluctuations about these mean optical depths. However, the accumulated far-UV absorption from pLLS could decrease F_{λ} and flatten the spectral energy distribution in the far-UV. There may also be bias in the selection of the intermediate-redshift quasars ($1.0 < z < 2.2$) used to construct rest-frame LyC composite spectra (Telfer et al. 2002; Shull et al. 2012b; Stevans et al. 2014; Tilton et al. 2016). To be selected, these AGN needed to have detectable fluxes in the *GALEX* far-UV channel covering 1344–1786 Å (Morrissey et al. 2005). Thus, the observed AGN sight lines generally avoided encountering LLS at $z_{\text{LLS}} \approx 0.5 - 1.0$ with $\log N_{\text{HI}} > 17.5$ that block the far-UV absorption. How strongly this selection bias affects the intrinsic AGN composite spectrum is still unknown.

3.4. Damped Ly α Absorbers

Although we have focused primarily on pLLS and LLS absorbers, we also include a discussion of the four DLAs detected along the sight lines to all 159 AGN in our sample. We provide these low-redshift statistics with only moderate astronomical interpretation, because of the small numbers and the accompanying uncertainties in deriving effective pathlengths. We compare our values with several previous DLA surveys that used UV data at $z < 1.65$ (Rao et al. 2006; Meiring et al. 2011; Battisti et al. 2012; Turnshek et al. 2015; Neeleman et al. 2016). Table 8 lists these four DLAs, together with six sub-DLAs ($\log N_{\text{HI}} = 19.0 - 20.3$) and two strong absorbers ($\log N_{\text{HI}} \approx 18.5 \pm 0.5$) whose large error bars place them near the sub-DLA range. As with our LLS statistics, we only consider redshifts $z_{\text{abs}} < 0.48$. Indeed, all four DLAs in our sample are at low redshifts ($z < 0.4$). Three were found serendipitously toward AGN in the COS-Halos survey, which excluded QSOs with strong Mg II absorbers at $z > 0.4$. The fourth DLA ($z_{\text{abs}} = 0.185$) is toward B0120-28, a UV-bright QSO used to probe the Magellanic Stream. Because of the small numbers of low-redshift DLAs and the range of QSO targeting strategies, the statistics that follow are uncertain, as are those in other low-redshift surveys.

In our COS survey of 102 QSOs at $z \geq 0.24$, we had an effective pathlength $\Delta z = 19.24$ sensitive to detecting LLS and DLA between $0.24 < z < 0.48$. We include the extra pathlength ($\Delta z = 29.26$) at the redshifts between $0.01 < z < 0.24$ available to all 159 AGN, and subtract a small amount ($\Delta z = 0.282$) of LLS-blocked spectra. Thus, we have total redshift coverage $\Delta z \approx 48$ sensitive to DLAs. Our statistics for DLA frequency are therefore based on four low-redshift DLAs: J1619+3342 ($z_a = 0.0963$) with $\log N_{\text{HI}} = 20.55 \pm 0.10$; J1009-0713 ($z_a = 0.1140$) with $\log N_{\text{HI}} = 20.68 \pm 0.10$; B0120-28 ($z_a = 0.185$) with $\log N_{\text{HI}} = 20.50 \pm 0.10$; and J1616+4153 ($z_a = 0.3211$) with $\log N_{\text{HI}} = 20.60 \pm 0.20$. Over pathlength $\Delta z = 48$, these four DLAs correspond to a line frequency,

$$\left(\frac{dN}{dz}\right)_{\text{DLA}} = 0.083^{+0.066}_{-0.040}, \quad (4)$$

at mean redshift $\langle z \rangle = 0.18$. We now compare this DLA frequency to those inferred from other surveys at $z < 1.65$. Owing to the small numbers of low- z DLAs, these surveys also have large uncertainties, ranging from $dN/dz = 0.033^{+0.026}_{-0.015}$ (Neeleman et al. 2016) to $0.25^{+0.24}_{-0.14}$ (Meiring et al. 2011). Most of the DLAs in those surveys are at higher redshifts ($z > 1$) compared to the 4 DLAs in our COS survey ($z = 0.096, 0.114, 0.185$, and 0.321). As we now discuss, our value is generally consistent with these prior estimates.

Rao, Turnshek, & Nestor (2006) used UV spectra from *HST*/STIS, identifying DLAs from a Mg II and Fe II selected sample. They found $dN/dz = 0.079 \pm 0.019$ for DLAs at $z < 1.65$ based on 18 DLAs found in 108 Mg II systems at ($0.11 < z < 0.9$) with median redshift $z = 0.609$. Their fit to DLA evolution over all redshifts gave $n(z) = n_0(1+z)^\gamma$ with $n_0 = 0.044 \pm 0.005$ and $\gamma = 1.27 \pm 0.11$. Meiring et al. (2011) found $dN/dz = 0.25^{+0.24}_{-0.14}$ from three DLAs along a COS-

surveyed path with $\Delta z = 11.94$. These three DLAs were also identified in our survey: J1616+4153 ($z_a = 0.3211$), J1619+3342 ($z_a = 0.0963$), J1009-0713 ($z_a = 0.1140$). Their much higher LLS absorber frequency was based on a smaller redshift pathlength, only 22% of that in our survey. Neeleman et al. (2016) conducted a large UV survey of 463 quasars at $z < 1.6$ over significant pathlength ($\Delta z = 123.3$). They found a line frequency $dN/dz = 0.033^{+0.026}_{-0.015}$ at median redshift $z = 0.623$. However, these statistics were based on just 4 DLAs with data from FOS, STIS, and COS. They originally had a total of 47 DLAs in their sample, but they excluded most of them in their statistics because they were found through Mg II targeting or because of a galaxy close to the QSO sightline.

In the most recent survey, Rao et al. (2017) examined the statistical properties of DLAs at $0.11 < z < 1.65$ using UV measurements (*HST*/ACS, *GALEX* and *HST*/COS). Over a wide range of redshifts ($z = 0 - 5$) they fit $dN/dz = (0.027 \pm 0.007)(1+z)^{1.682 \pm 0.200}$. This fit corresponds to $dN/dz = 0.036$ at the mean redshift ($z = 0.18$) of our survey. They find no bias with Mg II-selected samples of DLAs. Their COS sample turned up no true DLAs (all had $\log N_{\text{HI}} \leq 20.0$) but two of them were sub-DLAs, also found in our survey (Systems #1 and #6 in Appendix A).

3.5. Opacity of the Low- z IGM

After the epoch of reionization of neutral hydrogen at $z \approx 7$, the IGM becomes mostly ionized. However, the UV continuum of intermediate-redshift AGN is still blanketed by Ly α absorbers that produce photoelectric opacity in their Lyman continua. This LyC opacity determines the mean-free-path of ionizing photons in the IGM, attenuates the ionizing photons from galaxies and quasars, and determines the metagalactic EUV background radiation (Fardal et al. 1998; Miralda-Escudé 2003; Haardt & Madau 2012; O’Meara et al. 2013). This continuum opacity is also relevant to measuring the composite spectrum of quasars in their rest-frame LyC. Our recent studies of AGN at intermediate redshifts ($z \approx 1.5 - 2.2$) exhibit frequent pLLS absorption (Shull et al. 2012b; Stevans et al. 2014; Tilton et al. 2016) whose LyC optical depth and recovery at shorter wavelengths is used to restore the underlying AGN continuum.

The primary observable of our survey is the bivariate distribution of H I absorbers in redshift and column density. For a Poisson-distributed ensemble of H I absorbers (Paresce et al. 1980), one can compute the *average* photoelectric continuum opacity in the low-redshift IGM by integrating over the relevant range of column densities. We find the gradient of optical depth with redshift,

$$\frac{d\tau_{\text{eff}}}{dz} = \int \left(\frac{d^2 \mathcal{N}_{\text{abs}}}{dz dN} \right) [1 - \exp\{-N\sigma(z)\}] dN. \quad (5)$$

Here, N denotes N_{HI} and we define the H I photoelectric optical depth as $\tau(\lambda_o) = N\sigma(\lambda_o)$ at a typical *observed* far-UV wavelength, $\lambda_o \equiv \lambda_{\text{LL}}(1+z_o)$. The Lyman continuum cross section is approximated as $\sigma(\lambda_o) \approx \sigma_0(\lambda_o/\lambda_{\text{LL}})^3$ where $\sigma_0 = 6.30 \times 10^{-18} \text{ cm}^2$. We adopt a fiducial far-UV wavelength $\lambda_o = 1130 \text{ \AA}$ where the COS/G130M coverage begins. By construction, $\lambda_o < \lambda_{\text{LL}}(1+z)$ and $z_o < z$ in order for λ_o to lie in

the LyC of the absorber.

We now compute the cumulative optical depth, $\tau_{\text{eff}}(z_o, z)$, due to a population of H I absorbers at redshift z . For absorbers with $\tau_{\text{LL}} < 1$ ($N < 1.59 \times 10^{17} \text{ cm}^{-2}$) we approximate $[1 - \exp(-\tau)] \approx \tau$. We express the H I column density distribution as separable power laws in column density and redshift,

$$f(N, z) \equiv \frac{d^2 \mathcal{N}_{\text{abs}}}{dz dN} = C_0 N^{-\beta} (1+z)^\gamma, \quad (6)$$

for column densities N measured in cm^{-2} . In our pLLS survey, a maximum-likelihood fit finds $\beta_{\text{pLLS}} = 1.48 \pm 0.05$, $\gamma_{\text{pLLS}} = 1.14^{+0.88}_{-0.89}$, and $C_0 = 4 \times 10^7$ over the higher range in column density ($15 \leq \log N \leq 20$). The redshift-gradient of LyC optical depth at observed wavelength λ_o depends on an integral over the column-density distribution,

$$\begin{aligned} \frac{d\tau_{\text{eff}}(z_o, z)}{dz} &= C_0 \sigma_0 \left[\frac{1+z_o}{1+z} \right]^3 (1+z)^\gamma \int_{N_1}^{N_2} N^{(-\beta+1)} dN \\ &= \frac{C_0 \sigma_0 (1+z)^\gamma}{(2-\beta)} \left[\frac{1+z_o}{1+z} \right]^3 \left[N_2^{(2-\beta)} - N_1^{(2-\beta)} \right] \end{aligned} \quad (7)$$

For $\beta_{\text{pLLS}} = 1.48 \pm 0.05$, the H I opacity is weakly dominated by the higher-column density absorbers with $\tau_{\text{eff}} \propto N_2^{0.52}$. Here, $\sigma(\lambda_o) \approx \sigma_0[(1+z_o)/(1+z)]^3$ is the cross section at wavelength λ_o . From the observed distribution parameters we derive an opacity gradient, $d\tau_{\text{eff}}/dz = (0.408)(1+z)^{\gamma_{\text{pLLS}}}[(1+z_o)/(1+z)]^3$ for the strong absorbers, $15 \leq \log N_{\text{HI}} \leq 17.2$. We then integrate $\tau_{\text{eff}}(z_o, z)$ from redshift z_o out to higher redshifts,

$$\begin{aligned} \tau_{\text{eff}}^{(\text{pLLS})}(z_o, z) &= (0.396) \int_{z_o}^z \left[\frac{1+z_o}{1+z} \right]^3 (1+z)^\gamma dz \\ &= \frac{(0.396)(1+z_o)^{\gamma+1}}{(2-\gamma)} \left[1 - \left(\frac{1+z_o}{1+z} \right)^{(2-\gamma)} \right] \end{aligned} \quad (8)$$

For our best-fitting index, $\gamma_{\text{pLLS}} = 1.14$, the optical depths at $\lambda_o = 1130 \text{ \AA}$ ($z_o = 0.24$) are $\tau_{\text{eff}}(z_o, z) = (0.25, 0.33, 0.39)$ for sources at $z = (1.0, 1.5, 2.0)$. These opacities depend somewhat on the index γ_{pLLS} . For $\gamma_{\text{pLLS}} = 2$, the integral has a logarithmic dependence,

$$\tau_{\text{eff}}^{(\text{pLLS})}(z_o, z) = (0.396)(1+z_o)^3 \ln \left[\frac{1+z}{1+z_o} \right]. \quad (9)$$

At $z = (1.0, 1.5, 2.0)$, the corresponding optical depths are $\tau_{\text{eff}}(z_o, z) = (0.37, 0.55, 0.69)$. Because several LLS surveys have coverage to higher redshifts, it is possible that γ_{pLLS} could be higher than our assumed value of $\gamma = 1.14$. However, this best-fit index is similar to previous studies. For example, Ribaud et al. (2011a) found $\gamma = 1.19 \pm 0.56$ for LLS with $\tau_{\text{LL}} \geq 1$ over the range $0.25 < z < 2.59$. However, their survey only had 3 LLS at $z \leq 0.5$ and 17 at $z \leq 0.84$.

Weaker lines in the Ly α forest, with $\log N < 15$, contribute less optical depth, $d\tau_{\text{eff}}/dz = (0.0674)(1+z)^{\gamma_{\text{LF}}}$,

from which we find

$$\tau_{\text{eff}}^{(\text{LF})}(z_o, z) = \frac{(0.0674)(1+z_o)^{\gamma+1}}{(2-\gamma)} \left[1 - \left(\frac{1+z_o}{1+z} \right)^{(2-\gamma)} \right]. \quad (10)$$

For the index, $\gamma_{\text{LF}} = 1.24 \pm 0.06$, that fits all absorbers at $\log N_{\text{HI}} > 13.0$ (Danforth et al. 2016), the Ly α -forest optical depths at $\lambda_o = 1130 \text{ \AA}$ ($z_o = 0.24$) are $\tau_{\text{eff}}(z_o, z) = 0.0453, 0.0614$, and 0.0727 for sources at $z = 1.0, 1.5$, and 2.0 . Combining the pLLS and Ly α forest, we find average optical depths of $\tau_{\text{eff}}(z_o, z) = 0.29, 0.39, 0.46$ in the far UV (1130 \AA) corresponding to the Lyman edge redshifted to $z_o = 0.24$ and sources at $z = 1.0, 1.5, 2.0$.

4. SUMMARY AND DISCUSSION

This *HST*/COS survey is one of the largest sets of 220 strong H I absorbers at low redshift. Our survey spans column densities ($14.0 \leq \log N_{\text{HI}} \leq 20.4$) and redshifts ($0.237 \leq z \leq 0.928$) sampled in bins of width $\Delta z = 0.04$ from $z = 0.24 - 0.84$ and $\Delta(\log N_{\text{HI}}) = 0.25$. With sensitivity to multiple lines in the H I Lyman series, our pLLS survey should be nearly complete for the 158 absorbers with $\log N_{\text{HI}} > 15$. The column densities of a few absorbers in two bins ($\log N_{\text{HI}} = 15.0 - 15.5$) may have shifted to adjoining bins owing to CoG effects of velocity components. We may also have missed some weak absorbers at $z > 0.5$, detected only in higher Lyman-series lines, since Ly α and Ly β shift out of the COS/G160M window at $z > 0.47$ and $z > 0.75$ respectively. Our survey includes 8 true LLS ($\log N_{\text{HI}} \geq 17.2$), one DLA ($\log N_{\text{HI}} = 20.34 \pm 0.12$), and 54 pLLS ($16.0 \leq \log N_{\text{HI}} < 17.2$). All absorbers were detected with the G130M and G160M gratings at spectral resolution ($R \approx 17,000$ or $\Delta v \approx 18 \text{ km s}^{-1}$) sufficient to measure multiple lines in the H I Lyman series, along with the Lyman decrement at $\log N_{\text{HI}} \geq 16.2$. Our Lyman-comb technique is superior for column-density determination compared to methods based on low resolution ($R \approx 1000$) data. By combining the Lyman-series CoG with the Lyman decrement, we obtain reliable values of N_{HI} and its bivariate distribution, $f(N_{\text{HI}}, z)$.

The COS distribution is in good agreement with previous *HST* surveys of LLS at $0.4 < z < 1.4$, with an absorber frequency per unit redshift parameterized as $dN/dz = N_0(1+z)^\gamma$ and summarized in Table 7. Storrie-Lombardi et al. (1994) found $dN/dz = (0.27)(1+z)^{1.55 \pm 0.45}$ and Stengler-Larrea et al. (1995) found $dN/dz = (0.25)(1+z)^{1.50 \pm 0.39}$. Each of these FOS studies analyzed the same seven LLS. From FOS and STIS data, Ribaldo et al. (2011a) fitted an index $\gamma = 1.19 \pm 0.56$ for LLS absorbers between $0.25 < z < 2.59$. The eight LLS systems in our COS survey are distinct from those in the FOS study and range from $z_{\text{abs}} = 0.2374$ to $z = 0.47379$ with median redshift $z_{\text{abs}} = 0.39$. Over total pathlength $\Delta z = 19.24$ between $0.24 < z < 0.48$, we find a mean frequency, $\langle dN/dz \rangle_{\text{LLS}} = 0.36_{-0.13}^{+0.20}$. With median redshift $z_{\text{LLS}} = 0.39$, this translates to $N(z) = N_0(1+z)^\gamma$ where $N_0 = 0.25_{-0.09}^{+0.13}$ at $z = 0$. An index $\gamma \approx 1.1$ is what one would expect for non-evolving pLLS absorbers at $z < 1$. For a Λ CDM cosmology with standard (Planck-2016) parameters, the expected red-

shift evolution for absorbers with constant space density ϕ_0 and cross section σ_0 is:

$$\frac{dN}{dz} = \frac{\phi_0 \sigma_0 c}{H_0} \frac{(1+z)^2}{[\Omega_m(1+z)^3 + \Omega_\Lambda]^{1/2}} \equiv \left(\frac{\phi_0 \sigma_0 c}{H_0} \right) S(z). \quad (11)$$

Over our sampled range in redshift, $0.24 \leq z \leq 0.84$, with $\Omega_m \approx 0.3$ and $\Omega_\Lambda \approx 0.7$, the cosmological factor is well-fitted by $S(z) = (1.08)(1+z)^{1.1}$ to 3% accuracy. Thus, our derived maximum-likelihood value $\gamma = 1.14_{-0.89}^{+0.88}$, is consistent with non-evolving absorbers, although the allowed range in γ provides poor constraint on their low- z evolution. Ultraviolet spectroscopic surveys of pLLS at $z = 0.7 - 1.5$, with better statistics and redshift leverage, would narrow the range of γ_{pLLS} and help to characterize their redshift evolution.

In the Introduction, we alluded to the relationship between LLS absorbers and the extended regions of galaxies. Using our statistical sample of pLLS, with observed frequency $dN/dz = 1.69 \pm 0.33$, equation (11) implies a cross section, $\sigma_0 = \pi R_0^2$, with effective radius R_0 if we associate the pLLS with an appropriate space density of galaxies. We use the luminosity function of low-redshift ($z = 0.1$) galaxies from the Sloan Digital Sky Survey (Blanton et al. 2003), with normalization $\phi_* = (1.49 \pm 0.04) \times 10^{-2} h^3 \text{ Mpc}^{-3}$ and faint-end slope $\alpha = -1.05 \pm 0.01$, to find:

$$R_0 = \left[\frac{dN/dz}{\pi(c/H_0) \phi_* S(z) (\Delta L/L^*)} \right]^{1/2} \approx (110 \pm 10 \text{ kpc}) h^{-1} [S(z) (\Delta L/L^*)]^{-1/2}. \quad (12)$$

The cosmological factor $S(z) \approx 1.57$ at the median absorber redshift ($z = 0.39$). The fractional luminosity bandwidth ($\Delta L/L^*$) depends on the minimum luminosity and ranges from 0.56 (integrating down to $0.5L^*$) to 1.83 (integrating down to $0.1L^*$). Both scaling factors enter as the square root. Taking $h \approx 0.7$ and recognizing the uncertainty in galactic parameters, we see that both LLS and pLLS have the correct absorber frequencies, dN/dz , to be associated with extended halos of luminous ($0.3 - 3.0L^*$) galaxies. In the COS-Halos Survey, the CGM of star-forming galaxies has been detected in O VI absorption (Tumlinson et al. 2011) out to distances of 100-150 kpc. Tumlinson et al. (2013) detected strong H I absorption averaging $\sim 1 \text{ \AA}$ in Ly α equivalent width out to 150 kpc, with 100% covering fraction for star-forming galaxies. Radial extents of 100-200 kpc are also consistent with the region of gravitational influence of $10^{12} M_\odot$ galaxies, estimated from a proper treatment of the virial radius (Shull 2014),

$$R_{\text{vir}}(M_h, z_a) = (206 \text{ kpc}) h_{70}^{-2/3} M_{12}^{1/3} (1+z_a)^{-1} \times \left[\frac{\Omega_m(z_a) \Delta_{\text{vir}}(z_a)}{200} \right]^{-1/3}. \quad (13)$$

This expression differs from often-used formulae by the scaling with overdensity Δ_{vir} and by the factor $(1+z_a)^{-1}$. This factor reflects the fact that most galaxies underwent virialization in the past, when the IGM background density was higher by a factor of $(1+z_a)^3$. Typical “half-mass assembly” redshifts are $z_a \approx 0.8 - 1.2$. After initial assembly, their proper size changes gradually

because of continued mass infall into the halo. From the statistics of current pLLS survey, we are unable to ascertain the H I column density at which “strong H I absorbers” are less directly associated with galaxy halos. Based on the steep fall-off of the observed differential distribution, $f(N_{\text{HI}}, z) \propto N_{\text{HI}}^{-1.65}$, it likely occurs below $N_{\text{HI}} = 10^{15} \text{ cm}^{-2}$. This prediction is consistent with observations (Figure 5 in Stocke et al. 2013) which find that virtually no absorbers with $\log N_{\text{HI}} \leq 14.5$ are within one virial radius of a galaxy of any luminosity. The issue of H I “covering factor” is difficult to constrain in our sample, since we have not undertaken a program to identify the associated galaxies. Many of them are at $z > 0.3$ and detecting them would be difficult.

The degree of pLLS/LLS evolution out to $z \approx 2$ is important for assessing the far-UV opacity to intermediate redshift AGN (Section 3.5). The scarcity of strong absorbers ($\log N_{\text{HI}} > 16.5$) results in large fluctuations about these mean optical depths. Far-UV absorption from pLLS could decrease F_{λ} and flatten the spectral energy distribution in the far-UV. Selection bias may affect the intermediate-redshift quasars ($1.0 < z < 2.2$) used to construct rest-frame LyC composite spectra (Telfer et al. 2002; Shull et al. 2012b; Stevans et al. 2014; Tilton et al. 2016). These AGN need to have detectable fluxes in the *GALEX* far-UV channel covering 1344–1786 Å (Morrissey et al. 2005). Thus, the observed AGN sight lines generally avoided encountering LLS at $z_{\text{LLS}} \approx 0.5 - 1.0$ with $\log N_{\text{HI}} > 17.5$ that block the far-UV absorption. How strongly this selection bias affects the intrinsic AGN composite spectrum is not yet understood.

We would benefit from larger FUV/NUV surveys of pLLS/LLS absorbers toward QSOs with $z_{\text{AGN}} = 1 - 2$, with attention to biases introduced by target selection. This project will be difficult, since FUV-bright QSOs are needed to extend the absorber distribution, $f(N, z)$, to higher redshifts, and targeting via the presence or absence of strong Mg II absorbers will bias the LLS survey. The current COS survey provides reliable data at low redshift ($z < 0.5$), but connecting line frequency, dN/dz , continuously to values at $z > 1.5$ (O’Meara et al. 2013) is critical for IGM radiative transfer models that rely on FUV opacities.

We now summarize the main results of our survey:

1. Over redshifts $0.24 \leq z \leq 0.84$, the average frequency for strong H I absorbers ($\log N_{\text{HI}} \geq 15.0$) is $\langle dN/dz \rangle \approx 4.95 \pm 0.39$. We parameterize the bivariate distribution of H I absorbers as $f(N, z) = C_0 N_{\text{HI}}^{-\beta} (1+z)^{\gamma}$, where a maximum likelihood fit over the ranges $0.24 \leq z \leq 0.84$ and $15 \leq \log N_{\text{HI}} \leq 20$ gives $\beta \approx 1.48 \pm 0.05$, $\gamma \approx 1.14^{+0.88}_{-0.89}$, and $C_0 = 4 \times 10^7$ for column densities N_{HI} in cm^{-2} . This distribution is poorly determined at $\log N_{\text{HI}} > 17.5$. The redshift evolution ($\gamma \approx 1.1$) is consistent with absorbers of constant space density and cross section.
2. Based on seven true LLS with $\log N_{\text{HI}} \geq 17.2$ between $0.24 < z < 0.48$, we derive a LLS frequency of $(dN/dz)_{\text{LLS}} = (0.25^{+0.13}_{-0.09})(1+z)^{\gamma}$, assuming the best-fitting index $\gamma = 1.14$ derived from MCMC simulations of all strong absorbers. The frequency

for pLLS is $(dN/dz)_{\text{pLLS}} = (1.69 \pm 0.33)(1+z)^{\gamma}$. If these absorbers are associated with halos of luminous ($0.3 - 3.0 L^*$) galaxies, the pLLS frequency implies circumgalactic gas cross sections of 100 – 150 kpc radial extent.

3. Over the range ($0.01 < z < 0.48$) of the COS survey of 159 AGN sensitive to DLAs, we found 4 DLAs over pathlength $\Delta z \approx 48$. From this, we estimate an absorber frequency, $(dN/dz)_{\text{DLA}} = 0.083^{+0.066}_{-0.040}$. Although uncertain, this frequency is lower than the previous (COS-studied) value, $0.25^{+0.24}_{-0.14}$ (Meiring et al. 2011), which was based on 3 DLAs over $\Delta z = 11.94$, but larger than the values $dN/dz \approx 0.027 - 0.036$ (Neeleman et al. 2016; Rao et al. 2017). All of these surveys suffer from small-number statistics.
4. Combining the data from low-redshift COS surveys of pLLS and Ly α forest absorbers, we estimate the H I photoelectric opacity gradient, $d\tau_{\text{eff}}/dz$, for mean optical depth in the far-UV continuum (1130 Å). For indices $\gamma_{\text{pLLS}} = 1.14$ and $\gamma_{\text{LF}} = 1.24$, with considerable stochasticity, we estimate mean far-UV optical depths $\tau_{\text{eff}}(z_0, z) = 0.29, 0.39$, and 0.46 for sources at $z = 1.0, 1.5$, and 2.0.
5. The observed distributions of strong H I absorbers are expected to have considerable variations among sight lines. Above $N_{\text{HI}} = (10^{17} \text{ cm}^{-2})N_{17}$, the fitted cumulative frequency is small, $dN(> N_{\text{HI}})/dz = (0.577)N_{17}^{-0.48}(1+z)^{\gamma}$. Our estimates of far-UV continuum opacity suggest that surveys of intermediate-redshift AGN may have a selection bias toward sight lines with low optical depths, lacking strong LLS absorbers.

This survey was based on observations made with the NASA/ESA Hubble Space Telescope, obtained from the data archive at the Space Telescope Science Institute. STScI is operated by the Association of Universities for Research in Astronomy, Inc. under NASA contract NAS5-26555. The project originated from individual and survey observations of AGN taken with the Cosmic Origins Spectrograph on the *Hubble Space Telescope*. We appreciate helpful discussions with John Stocke, Todd Tripp, and David Turnshek. In early stages, this research was supported by grant HST-GO-13302.01.A from the Space Telescope Science Institute to the University of Colorado Boulder. More recent work was carried out through academic support from the University of Colorado.

REFERENCES

- Bahcall, J. N., Bergeron, J., Boksenberg, A., et al. 1993, *ApJS*, 87, 1
- Battisti, A. J., Meiring, J. D., Tripp, T. M., et al. 2012, *ApJ*, 744, 93
- Blanton, M. R., Hogg, D. W., Bahcall, N. A., et al. 2003, *ApJ*, 592, 819
- Bordoloi, R., Tumlinson, J., Werk, J. K., et al. 2014, *ApJ*, 796, 136
- Clauset, A., Shalizi, C. R., & Newman, M. E. J. 2009, *SIAM Review*, 51, 661
- Cooksey, K. L., Prochaska, J. X., Chen, H.-W., et al. 2008, *ApJ*, 676, 262
- Crighton, N. H. M., Morris, S. L., Bechtold, J., et al. 2010, *MNRAS*, 402, 1273
- Danforth, C. W., & Shull, J. M. 2008, *ApJ*, 679, 194
- Danforth, C. W., Keeney, B. A., Tilton, E. M., et al. 2016, *ApJ*, 817, 111
- Fardal, M. A., Giroux, M. L., & Shull, J. M. 1998, *AJ*, 115, 2206
- Foreman-Mackey, D., Hogg, D. W., Lang, D., & Goodman, J. 2013, *PASP*, 125, 306
- Fox, A. J., Lehner, N., Tumlinson, J., et al. 2013, *ApJ*, 778, 187
- Gehrels, N. 1986, *ApJ*, 303, 336
- Goldstein, M. L., Morris, S. A., & Yen, G. G. 2004, *European Physical Journal B*, 41, 255
- Goodman, J., & Weare, J. 2010, *Commun Appl Math Comput Sci.*, 5, 65
- Green, J. C., Froning, C. S., Osterman, S., et al. 2012, *ApJ*, 744, 60
- Haardt, F., & Madau, P. 2012, *ApJ*, 746, 125
- Hussain, T., Muzahid, S., Narayanan, A., et al. 2015, *MNRAS*, 446, 2444
- Janknecht, E., Reimers, D., Lopez, S., & Tytler, D. 2006, *A&A*, 458, 427
- Jenkins, E. B., Bowen, D. V., Tripp, T. M., & Sembach, K. R. 2005, *ApJ*, 623, 767
- Keeney, B. A., Stocke, J. T., Rosenberg, J. L., Tumlinson, J., & York, D. G. 2006, *AJ*, 132, 2496
- Kim, T.-S., Carswell, R. F., Cristiani, S., D'Odorico, S., & Giallongo, E. 2002, *MNRAS*, 335, 555
- Lehner, N., Prochaska, J. X., Kobulnicky, H. A., et al. 2009 *ApJ*, 694, 734
- Lehner, N., Howk, J. C., Tripp, T. M. et al. 2013 *ApJ*, 770, 138
- Markwardt, C. B. 2009, *Astronomical Data Analysis Software and Systems XVIII*, ASP Conference Series, Vol. 411, 251
- Meiring, J. D., Tripp, T. M., Prochaska, J. X., et al. 2011, *ApJ*, 732, 35
- Meiring, J. D., Tripp, T. M., Werk, J. K., et al. 2013, *ApJ*, 767, 49
- Miralda-Escudé, J. 2003, *ApJ*, 596, 66
- Morrissey, P., Schiminovich, D., Barlow, T., et al. 2005, *ApJ*, 619, L7
- Morton, D. C. 2003, *ApJS*, 149, 205
- Muzahid, S., Srianand, R., & Charlton, J. 2015, *MNRAS*, 448, 2840
- Narayanan, A., Savage, B. D., Wakker, B. P., et al. 2011, *ApJ*, 730, 15
- Neeleman, M., Prochaska, J. X., Ribaldo, J., et al. 2016, *ApJ*, 818, 113
- Newman, M. E. C. 2005, *Contemporary Physics*, 46, 323
- O'Meara, J. M., Prochaska, J. X., Worseck, G., Chen, H.-W., & Madau, P. 2013, *ApJ*, 765, 137
- Paresce, F., McKee, C. F., & Bowyer, S. 1984, *ApJ*, 240, 387
- Penton, S. V., Stocke, J. T., & Shull, J. M. 2004, *ApJS*, 152, 29
- Prochaska, J. X., Werk, J. K., Worseck, G., et al. 2017, *ApJ*, 837, 169
- Rao, S. M., Turnshek, D. A., & Nestor, D. B. 2006, *ApJ*, 636, 610
- Rao, S. M., Turnshek, D. A., Sardane, G. M., & Monier, E. M. 2017, *MNRAS*, 471, 3428
- Ribaldo, J., Lehner, N., & Howk, J. C. 2011a, *ApJ*, 736, 42
- Ribaldo, J., Lehner, N., Howk, J. C., et al. 2011b, *ApJ*, 743, 207
- Rudie, G. C., Steidel, C. C., Shapley, A. E., & Pettini, M. 2013, *ApJ*, 769, 146
- Sargent, W. L. W., Steidel, C. C., & Boksenberg, A. 1989, *ApJS*, 69, 703
- Savage, B. D., Lehner, N., Narayanan, A., et al. 2011, *ApJ*, 743, 180
- Shull, J. M. 2014, *ApJ*, 784, 142
- Shull, J. M., Roberts, D., Giroux, M. L., et al. 1999, *AJ*, 118, 1450
- Shull, J. M., Giroux, M. L., Penton, S. V., et al. 2000, *ApJ*, 538, L13
- Shull, J. M., Jones, J. R., Danforth, C. W., & Collins, J. A. 2009, *ApJ*, 699, 754
- Shull, J. M., Smith, B. D., & Danforth, C. W. 2012a, *ApJ*, 759, 23
- Shull, J. M., Stevans, M. L., & Danforth, C. W. 2012b, *ApJ*, 752, 162
- Shull, J. M., Danforth, C. W., & Tilton, E. M. 2014, *ApJ*, 796, 49
- Simcoe, R. A., Sargent, W. L. W., Rauch, M., & Becker, G. 2006, *ApJ*, 637, 648
- Songaila, A., & Cowie, L. 2010, *ApJ*, 721, 1448
- Steidel, C. C. 1990, *ApJS*, 74, 37
- Stengler-Larrea, E. A., Boksenberg, A., Steidel, C. C., et al. 1995, *ApJ*, 444, 64
- Stevans, M. L., Shull, J. M., Danforth, C. W., & Tilton, E. M. 2014, *ApJ*, 794, 75
- Stocke, J. T., Keeney, B. A., Danforth, C. W. et al. 2013, *ApJ*, 763, 148
- Stocke, J. T., Keeney, B. A., Danforth, C. W. et al. 2014, *ApJ*, 791, 128
- Storrie-Lombardi, L. J., McMahon, R. G., Irwin, M. J., & Hazard, C. 1994, *ApJ*, 427, L13.
- Tejos, N., Morris, S. L., Finn, C. W., et al. 2014, *MNRAS*, 437, 2017
- Telfer, R., Zheng, W., Kriss, G. A., & Davidsen, A. F. 2002, *ApJ*, 656, 773
- Tilton, E. M., Stevans, M. L., Shull, J. M., & Danforth, C. W. 2016, *ApJ*, 817, 56
- Tripp, T., Bechtold, J., & Green, R. F. 1994, *ApJ*, 433, 533
- Tripp, T., Meiring, J. D., Prochaska, J. X. et al. 2011, *Science*, 334, 952
- Tumlinson, J., Thom, C., Werk, J. K., et al. 2011a, *Science*, 334, 948
- Tumlinson, J., Werk, J. K., Thom, C., et al. 2011b, *ApJ*, 733, 111
- Tumlinson, J., Thom, C., Werk, J. K., et al. 2013, *ApJ*, 777, 59
- Turnshek, D. A., Monier, E. M., Rao, S. M., et al. 2015, *MNRAS*, 449, 1536
- Tytler, D. 1987a, *ApJ*, 321, 49
- Tytler, D. 1987b, *ApJ*, 321, 69
- Weymann, R. J., Jannuzi, B. T., Lu, L., et al. 1998, *ApJ*, 506, 1
- Wolfe, A. M., Gawiser, E., & Prochaska, J. X. 2005, *ARA&A*, 43, 861

APPENDIX

APPENDIX A: NOTES ON LLS AND PLLS ABSORBERS

In this Appendix, we discuss the column-density determinations for 73 strong H I absorbers ($\log N_{\text{HI}} > 15.75$) at $z_{\text{abs}} \geq 0.24$. In an approximate analysis used in our construction of an AGN composite spectrum (Stevens et al. 2014), the H I column densities of these systems were estimated and used to correct the underlying continuum. These estimates were based on automated CoG fitting, which becomes uncertain when the Lyman lines reach saturation (Table 2) and in the presence of multiple velocity components. In the current survey, we carefully examined each of these systems, combining multi-component CoG fits with an analysis of the flux decrement at the Lyman limit. In fitting the continuum above and below the LL, we looked for contamination by broad AGN emission lines using the template shown in Figure 1. The underlying continuum lies below these emission lines. Systems labeled #1 through #26 (Table 6) had initial estimates $\log N_{\text{HI}} \geq 16.5$, for which we expect a clear Lyman limit with optical depth $\tau_{\text{LL}} \geq 0.2$. Systems #27 to #72 had estimated column densities $15.75 \leq \log N_{\text{HI}} \leq 16.49$. System #73 is a DLA with $\log N_{\text{HI}} = 20.34 \pm 0.12$ at $z_{\text{abs}} = 0.3211$ not tabulated in Stevens et al. (2014). Some of these systems were discussed in previous papers (Tripp et al. 2011; Ribaud et al. 2011b; Tumlinson et al. 2011b; Lehner et al. 2013; Fox et al. 2013; Tilton et al. 2016).

For the LLS and pLLS absorbers, our strategy of combining CoG with LL flux decrements, when detected, provided confirmation of the column density and its uncertainty. In a number of cases involving multiple velocity components, we used the spectral resolution of G130M and G160M gratings to fit multi-component CoGs. When the components separations were less than 100 km s^{-1} , we combined them into a single system. In a few instances with clearly separated components ($\Delta v > 150 - 200 \text{ km s}^{-1}$) we kept separate track of the individual column densities and split them into separate absorbers, denoted Systems #24abc, #47abc, #59ab, and #60ab. At the COS spectral resolution, the LL flux decrements and optical depths, τ_{LL} , typically arise from all components within $100\text{--}400 \text{ km s}^{-1}$. With good S/N in the higher-order Lyman lines, we are able to identify absorption systems with $\Delta v \geq 100 \text{ km s}^{-1}$. In comparing our column densities with prior work, we usually found good agreement ($\Delta \log N_{\text{HI}} \leq 0.1$), but deviations are noted in the narratives and in the final column of Table 6. In our statistical analysis (Section 3 and Appendix B) we use our revised column densities and error bars.

#1: *SDSS J092554.70+400414.1*, $z_{\text{AGN}} = 0.471139$, $z_{\text{abs}} = 0.24770$. — See Figure 9. Because the COS observations for this sight line only covered wavelengths $\lambda > 1164 \text{ \AA}$, higher-order Lyman lines (above Ly ϵ) and the Lyman edge are not accessible. However, Ly α shows a sub-DLA with damping wings that we fit with $\log N_{\text{HI}} = 19.45 \pm 0.05$, a value slightly smaller than that ($\log N = 19.55 \pm 0.15$) quoted by Battisti et al. (2012), Meiring et al. (2013), and Lehner et al. (2013). Although our CoG solution for Ly α - Ly ϵ gives a lower value ($\log N = 19.33 \pm 0.03$, $b = 37 \pm 5 \text{ km s}^{-1}$), we adopt $\log N_{\text{HI}} = 19.45 \pm 0.10$ and $b = 35 \pm 5 \text{ km s}^{-1}$ because the lower column density from the CoG does not reproduce the observed Ly α damping wings.

#2: *FIRST J020930.7-043826*, $z_{\text{AGN}} = 1.13194$, $z_{\text{abs}} = 0.39043$. — See Figure 9. The flux at $\lambda < 1270 \text{ \AA}$ is consistent with zero ($< 1\%$) transmission in the Lyman continuum (optical depth $\tau_{\text{LL}} > 4.6$ and $\log N_{\text{HI}} > 17.86$). Lines above Ly12 suffer from crowding and are difficult to measure accurately. The CoG fit to Ly α - Ly12 constrains $\log N_{\text{HI}}$ to the range $18.1\text{--}18.9$ with $b = 45 \pm 5 \text{ km s}^{-1}$, in agreement with the observed line profiles. In their Appendix A, Tejos et al. (2014) quoted $\log N_{\text{HI}} = 18.87 \pm 0.03$ with $b = 34 \pm 1 \text{ km s}^{-1}$. However, this error bar seems far too small, and we adopt $\log N_{\text{HI}} = 18.5 \pm 0.4$.

#3: *SDSS J151428.64+361957.9*, $z_{\text{AGN}} = 0.694596$, $z_{\text{abs}} = 0.41065$. — See Figure 9. Low-quality data ($S/N \sim 6$ per resolution element) limits the accuracy of the Ly decrement method. The continuum has undulations ($1300\text{--}1340 \text{ \AA}$) arising from AGN emission lines of Ne VIII and O IV. From transmission shortward of the Ly edge, we find $\log N_{\text{HI}} = 17.89 \pm 0.06$. The Lyman lines show a single component, with a CoG fit to Ly α - Ly12 giving $\log N_{\text{HI}} = 18.04 \pm 0.20$ and $b = 43 \pm 2 \text{ km s}^{-1}$. Two absorption components are seen in Si III in this system, not apparent in the H I lines. We adopt the decrement measurement, $\log N_{\text{HI}} = 17.89 \pm 0.06$, and find that $b = 45 \pm 5 \text{ km s}^{-1}$ reproduces the observed line profiles.

#4: *SDSS J113327.78+032719.1*, $z_{\text{AGN}} = 0.525073$, $z_{\text{abs}} = 0.23740$. — See Figure 9. The initial redshift measurement of this system at $z = 0.2466$ (Stevens et al. 2014) placed it within our first redshift bin ($z_{\text{abs}} = 0.24 - 0.28$). The higher Lyman lines ($n > 11$) lie blueward of the edge of the COS spectra, and no Ly decrement measurement is possible. A more careful examination of the data shows two absorbers at redshifts slightly below $z = 0.24$, and thus outside bin 1. Our CoG fits to the red and blue components are inconsistent with the higher-order Lyman line profiles, suggesting the presence of additional components. We find qualitative agreement with the line profiles for Ly α - Ly10 using a three-component model: Component 1 ($z_1 = 0.2374$) with $\log N_1 = 17.2 \pm 0.1$, $b_1 = 35 \pm 5 \text{ km s}^{-1}$; Component 2 ($z_2 = 0.2378$) with $\log N_2 = 15.8 \pm 0.1$, $b_2 = 25 \pm 5 \text{ km s}^{-1}$; Component 3 ($z_3 = 0.2383$) with $\log N_3 = 16.5 \pm 0.1$, $b_3 = 25 \pm 5 \text{ km s}^{-1}$. The velocity separations are $\Delta v_{12} = 97 \text{ km s}^{-1}$ and $\Delta v_{23} = 121 \text{ km s}^{-1}$. We adopt the summed total column density $\log N_{\text{HI}} = 17.29 \pm 0.11$.

#5: *SDSS J100902.06+071343.8*, $z_{\text{AGN}} = 0.455631$, $z_{\text{abs}} = 0.35586$. — See Figure 9. The initial estimate of this system, $\log N = 17.41 \pm 0.04$ (Stevens et al. 2014) underpredicts the Ly decrement significantly. The continuum at $\lambda < 1240 \text{ \AA}$ is consistent with zero flux ($\tau_{\text{LL}} > 5$, $\log N > 17.9$), and the lower-order Lyman lines (Ly α - Ly6) are contaminated with other absorption. We adopt a CoG fit to Ly7 - Ly12 with $\log N_{\text{HI}} = 18.3 \pm 0.2$ and $b = 37 \pm 2 \text{ km s}^{-1}$, consistent with the decrement and providing a good match to the line profiles. This column is similar to the range (18.0 - 18.8) quoted by Tumlinson et al. (2011b) and the value ($\log N_{\text{HI}} = 18.4 \pm 0.2$) in Lehner et al. (2013). This sight line also contains a DLA (Meiring et al. 2011) at $z_{\text{abs}} = 0.1140$ with $\log N_{\text{HI}} = 20.68 \pm 0.10$ (see Table 8).

#6: *SDSS J100102.55+594414.3 (SBS 0957+599)*, $z_{\text{AGN}} = 0.746236$, $z_{\text{abs}} = 0.30355$. — See Figure 9. The Stevens et al. (2014) CoG measurement of this system ($\log N_{\text{HI}} = 17.27 \pm 0.04$) significantly underpredicts the observed Lyman decrement. The continuum at $\lambda < 1194 \text{ \AA}$ is consistent with zero flux ($\tau_{\text{LL}} > 5$, $\log N_{\text{HI}} > 17.9$), and significant damping wings in the Ly α profile imply an even higher column density. Battisti et al. (2012) found $\log N_{\text{HI}} = 19.32 \pm 0.10$ by fitting the Ly α profile wings. We use a CoG fit to Ly α - Ly11, constrained by the requirement that $\log N_{\text{HI}} > 18$, to find $\log N_{\text{HI}} = 19.41 \pm 0.12$ and $b = 45 \pm 1 \text{ km s}^{-1}$, consistent with both the line profiles and the Ly decrement.

#7: *SDSS J154553.48+093620.5*, $z_{\text{AGN}} = 0.665$, $z_{\text{abs}} = 0.47379$. — See Figure 8. This absorber exhibits a strong Lyman decrement ($\tau_{\text{LL}} > 5$) implying $\log N_{\text{HI}} > 17.9$. The transmitted flux shows no recovery from the LL ($\lambda_{\text{obs}} = 1344 \text{ \AA}$) shortward to the end of the COS/G130M data ($\lambda_{\text{obs}} \approx 1155 \text{ \AA}$), which requires $\log N_{\text{HI}} \geq 18.1$. A CoG fit to Ly β - Ly12 gives $\log N = 17.67 \pm 0.15$, inconsistent with the Ly decrement. The Ly α absorption line lies redward of the end of the COS/FUV data, and we cannot use its damping wings as a measurement of column density. The redward wing of Ly β limits $\log N < 19.0$, but the CoG suggests $\log N_{\text{HI}} < 18.5$. The dominant absorption in metal lines (C II, Si II, and O VI) occurs at $z_1 = 0.4738$, with additional absorption 150 km s^{-1} redward ($z_2 = 0.4743$) seen in C II and O VI. However, this second component cannot explain the redward wing of Ly β . We adopt a range $18.1 < \log N_{\text{HI}} \leq 18.5$, treated statistically as $\log N_{\text{HI}} = 18.3 \pm 0.2$, and find that $b = 25 - 35 \text{ km s}^{-1}$ matches the line profiles.

#8: *SDSS J091029.75+101413.6*, $z_{\text{AGN}} = 0.463194$, $z_{\text{abs}} = 0.41924$. — This AGN sight line also contains system #14 (see below). The low-S/N G130M data makes line measurements somewhat uncertain. The UV continuum is contaminated by prominent AGN emission lines: O I (1355-1370 \AA observed), C III $\lambda 977$ (1430-1450 \AA observed), and O VI $\lambda 1035$ (1490-1520 \AA observed). Fitting a continuum through line-free regions at 1390-1410 \AA , 1460-1480 \AA , and 1490-1520 \AA , we find a Lyman decrement with $\tau_{\text{LL}} = 0.49_{-0.11}^{+0.05}$ ($\log N = 16.89_{-0.11}^{+0.04}$). A CoG fit gives $\log N_{\text{HI}} = 16.51 \pm 0.09$ with $b = 38 \pm 8 \text{ km s}^{-1}$, inconsistent with the Ly decrement. We adopt the decrement value, with its asymmetric error bars, $\log N_{\text{HI}} = 16.89_{-0.11}^{+0.04}$.

#9: *SBS 1108+560*, $z_{\text{AGN}} = 0.766619$, $z_{\text{abs}} = 0.46334$. — See Figure 5. The CoG solution to this system ($\log N \sim 17.1$) significantly underpredicts the flux in the Lyman continuum. The spectrum has high S/N, allowing us to estimate the Ly decrement to great precision. The transmitted continuum shortward of the Lyman edge lies *above* the interstellar absorption line of C II $\lambda 1334.53$; we also see Si II absorption lines at 1190 \AA and 1193 \AA . The transmitted flux in the Lyman continuum is $1.2 \pm 0.2\%$, implying optical depth $\tau_{\text{LL}} = 4.42 \pm 0.15$ and our adopted value, $\log N_{\text{HI}} = 17.85 \pm 0.02$. With this column density, we find that $b = 18 \pm 2 \text{ km s}^{-1}$ provides a good match to the relatively narrow Lyman line profiles. A second, blue component visible in Ly ϵ - Ly13 is fitted with a CoG having $\log N_{\text{HI}} = 15.9 \pm 0.05$ and $b = 20 \pm 5 \text{ km s}^{-1}$. The combination of these two components, the weaker of which makes little contribution to the Ly decrement, fits the line profiles well.

#10: *PG 1206+459*, $z_{\text{AGN}} = 1.16254$, $z_{\text{abs}} = 0.92772$. — See Figure 9. This high-redshift absorption system is observable by COS only in the higher Lyman lines (Ly6 and above). However, the high-quality of the data and the Ly decrement allow accurate measurements for this pLLS (Tripp et al. 2011). Two components appear in the $n \geq 9$ Lyman lines. The optical depth, $\tau_{\text{LL}} = 0.86 \pm 0.02$, implies a total column density $\log N_{\text{tot}} = 17.15 \pm 0.05$, but the allocation to the two components remains uncertain. Two components fit the profiles well ($\Delta v = 156 \text{ km s}^{-1}$): Component 1 (at $z_1 = 0.9270$) with $\log N_1 = 16.95 \pm 0.05$, $b_1 = 28 \pm 5 \text{ km s}^{-1}$; Component 2 (at $z_2 = 0.9280$) with $\log N_2 = 16.3 \pm 0.1$, $b_2 = 25 \pm 5 \text{ km s}^{-1}$. Their column densities sum to $\log N_{\text{tot}} = 17.04 \pm 0.06$ and account for the Ly decrement: In their study of this absorber, Tripp et al. (2011) fitted three clusters of 9 velocity components, which they labeled Group A ($\log N_A = 15.74$), Group B ($\log N_B = 16.99$), and Group C ($\log N_C = 15.98$). Their summed column density ($\log N_{\text{tot}} = 17.05 \pm 0.11$) is 0.05 dex less than our adopted value, $\log N_{\text{HI}} = 17.10 \pm 0.10$, which is intermediate between our CoG and LL measurements.

#11: *PG 1630+377*, $z_{\text{AGN}} = 1.47607$, $z_{\text{abs}} = 0.27395$. — See Figure 9. Our measurement of the Lyman decrement ($\tau_{\text{LL}} = 0.69 \pm 0.04$) requires total column density $\log N = 17.04 \pm 0.05$, comparable to previously reported values of 17.06 ± 0.05 (Ribaud et al. 2011b), 16.98 ± 0.05 (Lehner et al. 2013), and 16.92 ± 0.04 (Stevens et al. 2014). Higher-order lines (Ly7 - Ly13) show two components ($\Delta v = 75 \text{ km s}^{-1}$): a strong, blue component ($z_1 = 0.27395$, $\log N_1 = 16.95 \pm 0.05$, $b_1 = 28 \pm 5 \text{ km s}^{-1}$) and a weaker, red component ($z_2 = 0.27427$, $\log N_2 = 16.3 \pm 0.1$, $b_2 = 25 \pm 5 \text{ km s}^{-1}$). We adopt $\log N_{\text{tot}} = 17.04 \pm 0.05$.

#12: *SDSS J100535.24+013445.7*, $z_{\text{AGN}} = 1.0809$, $z_{\text{abs}} = 0.83711$. — The Ly decrement from this absorber is determined by N_{HI} of both system #12 and #52 ($z = 0.83938$) located 370 km s^{-1} to the red. The LL optical depth was fitted to $\tau_{\text{LL}} = 0.414 \pm 0.03$ ($\log N_{\text{tot}} = 16.82 \pm 0.04$). System #12 consists of two closely separated ($\Delta v = 77 \text{ km s}^{-1}$) velocity components. CoG fits to the Lyman lines, where separable in Ly7 - Ly13, give: Component 1 ($z_1 = 0.83690$) with $\log N_1 = 16.53 \pm 0.07$, $b_1 = 25 \pm 3 \text{ km s}^{-1}$; and Component 2 ($z_2 = 0.83737$) with $\log N_2 = 16.31 \pm 0.09$, $b_2 = 20 \pm 3 \text{ km s}^{-1}$ summing to our adopted value $\log N_{\text{tot}} = 16.73 \pm 0.10$ for system #12. Including the (CoG-fitted) $\log N_{\text{HI}} = 16.09 \pm 0.05$ for system #52, we find $\log N_{\text{tot}} = 16.82 \pm 0.10$, consistent with the Ly decrement. Although system #12 is blended with system #52, we report them separately because they are easily separable ($\Delta v \approx 390 \text{ km s}^{-1}$) in their Lyman line absorption.

#13: *SDSS J143511.53+360437.2*, $z_{\text{AGN}} = 0.428593$, $z_{\text{abs}} = 0.37297$. — The AGN continuum appears to have broad O I emission features (1310–1335 Å observed frame). The observed decrement ($\tau_{\text{LL}} = 0.42 \pm 0.05$) implies $\log N_{\text{HI}} \approx 16.82 \pm 0.05$. The CoG solution to Ly α - Ly13, omitting Ly γ , Ly δ , and Ly11 which are blended, gives a consistent (adopted) solution, $\log N_{\text{HI}} = 16.84 \pm 0.06$, $b = 19 \pm 1 \text{ km s}^{-1}$. This sight line also contains a sub-DLA at $z_{\text{abs}} = 0.2026$ with $\log N_{\text{HI}} = 19.80 \pm 0.10$ (see Table 7).

#14: *SDSS J091029.75+101413.6*, $z_{\text{AGN}} = 0.463194$, $z_{\text{abs}} = 0.26340$. — See also system #8 above. Low-quality data ($S/N \sim 2$) and an undulating AGN continuum in the region of the Lyman limit make decrement measurements unreliable. However, the uncertain values, $\log N_{\text{HI}} = 16.86 \pm 0.5$ (Stevans et al. 2014) and $16.58^{+0.04}_{-0.07}$ (Prochaska et al. 2017) are not supported, as we detect no Ly decrement ($\tau_{\text{LL}} < 0.1$). Our CoG fit to unblended lines of Ly β , Ly γ , Ly ϵ , and Ly6 - Ly10 gives $\log N_{\text{HI}} = 16.21 \pm 0.07$, $b = 21 \pm 2 \text{ km s}^{-1}$, consistent with the lack of a measurable Ly decrement

#15: *SDSS J161916.54+334238.4*, $z_{\text{AGN}} = 0.470946$, $z_{\text{abs}} = 0.47088$. — This absorber is offset by just 146 km s^{-1} blueward of the AGN systemic velocity. The LL lies on the red wing of a damped Ly α absorber profile at 1332.7 Å ($z_{\text{DLA}} = 0.0963$) with $\log N_{\text{HI}} = 20.55 \pm 0.10$ (see Table 7). However, there is sufficiently recovered continuum in the blue wing of the DLA (1310–1320 Å) to measure a LL decrement with $\tau_{\text{LL}} = 0.43 \pm 0.05$ and $\log N_{\text{HI}} = 16.83 \pm 0.05$. This solution fits the stronger Lyman lines (Ly α - Ly8) but increasingly overpredicts the higher-order absorption profiles ($n \geq 9$). We adopt $\log N_{\text{HI}} = 16.83 \pm 0.10$ and $b = 32 \pm 5 \text{ km s}^{-1}$, noting unresolved structure in the system.

#16: *SDSS J155048.29+400144.9*, $z_{\text{AGN}} = 0.496843$, $z_{\text{abs}} = 0.31257$. — This sight line has two strong absorbers (#16 and #17). The redshift of this absorber places the LL in the complicated region (1200 – 1220 Å) of the Galactic DLA and geocoronal N I and H I emission lines. The AGN continuum may be contaminated by broad O IV $\lambda 788$ emission (observed between 1170–1185 Å). The observed Ly decrement (1190–1197 Å) is uncertain ($\tau_{\text{LL}} = 0.13 \pm 0.03$) implying $\log N_{\text{HI}} = 16.31 \pm 0.10$, a factor of 2 lower than that (16.62 ± 0.06) found by Stevans et al. (2014) from a CoG fit. Additional absorption is present in some of the higher-order Lyman lines ($n > 8$) which is not accounted for by this lower- N solution. This may have driven the previous CoG solution to a higher column density. We adopt $\log N_{\text{HI}} = 16.3 \pm 0.1$ and $b = 40 \pm 5 \text{ km s}^{-1}$.

#17: *SDSS J155048.29+400144.9*, $z_{\text{AGN}} = 0.496843$, $z_{\text{abs}} = 0.49200$. — The Lyman decrement ($\tau_{\text{LL}} = 0.25 \pm 0.03$, $\log N_{\text{HI}} = 16.60 \pm 0.05$) is consistent with the Stevans et al. (2014) value, $\log N_{\text{HI}} = 16.57 \pm 0.05$. We adopt $\log N_{\text{HI}} = 16.60 \pm 0.05$ with $b = 25 \pm 5 \text{ km s}^{-1}$.

#18: *PKS 0552–640*, $z_{\text{AGN}} = 0.680$, $z_{\text{abs}} = 0.34513$. — See Figure 6. This system lies on the red edge of a damped Ly α profile (the Galactic DLA). However, the Lyman edge lies $\sim 10 \text{ Å}$ redward of the line center where the continuum has recovered from DLA absorption. The decrement ($\tau_{\text{LL}} = 0.64 \pm 0.04$) requires $\log N_{\text{HI}} = 17.01 \pm 0.03$. The data are of very high quality ($S/N \sim 25$), and we are able to measure a single, narrow absorber in 24 lines (Ly α to Ly ω). The highest-order lines ($n \geq 16$) are blended and not useful in CoG analysis as noted in Table 2. A fit to Ly β - Ly15 gives $\log N_{\text{HI}} = 17.01 \pm 0.05$, $b = 16 \pm 2 \text{ km s}^{-1}$. This column density is above previous values, 16.90 ± 0.08 (Lehner et al. 2013) and 16.71 ± 0.03 (Stevans et al. 2014).

#19: *SDSS J124511.25+335610.1*, $z_{\text{AGN}} = 0.711698$, $z_{\text{abs}} = 0.5567$. — This AGN sight line has three strong absorbers (systems #19, #20, and #46) which we fit simultaneously to set the continuum. The decrement for this system gives $\tau_{\text{LL}} = 0.12 \pm 0.02$, although the local continua may be contaminated by AGN emission lines. The LL-inferred column density, $\log N_{\text{HI}} = 16.28 \pm 0.07$, is much smaller than the CoG fit, $\log N_{\text{HI}} = 16.63 \pm 0.09$, but additional absorption appears in the higher ($n > 8$) Lyman lines. We adopt $\log N_{\text{HI}} = 16.28 \pm 0.10$ based on the Ly decrement, with an increased error.

#20: *SDSS J124511.25+335610.1*, $z_{\text{AGN}} = 0.711698$, $z_{\text{abs}} = 0.68927$. — As noted for system #19, we use a multi-component fit to set the continuum. The Lyman decrement ($\tau_{\text{LL}} = 0.37 \pm 0.03$) implies $\log N_{\text{HI}} = 16.77 \pm 0.03$, somewhat larger than the value (16.68 ± 0.2) from Stevans et al. (2014). The local continua may be contaminated by AGN emission lines. A two-component profile is seen in the $n > 6$ lines. Our CoG fits two closely separated ($\Delta z = 75 \text{ km s}^{-1}$) individual components in Ly6 - Ly11 gives: Component 1 ($z_1 = 0.68894$) with $\log N_1 = 16.57 \pm 0.10$, $b_1 = 22 \pm 3 \text{ km s}^{-1}$, and Component 2 ($z_2 = 0.68936$) with $\log N_2 = 16.10 \pm 0.1$, $b_2 = 35 \pm 5 \text{ km s}^{-1}$, summing to our adopted column density, $\log N_{\text{tot}} = 16.70 \pm 0.11$, similar to the observed decrement.

#21: *SDSS J100102.55+594414.3 (SBS 0957+599)*, $z_{\text{AGN}} = 0.746236$, $z_{\text{abs}} = 0.41595$. — The AGN continuum is contaminated by the prominent emission lines of Ne VIII ($\lambda 770, 780$) and O IV ($\lambda 788$) observed at 1320–1380 Å. Shortward of the Lyman edge, the flux level is contaminated by the prominent 700 Å lines of O III and N III (1220–1250 Å observed frame). The Ly decrement is somewhat uncertain because of this line emission and continuum placement. Choosing continua redward and blueward of the LL to avoid these emission lines, our best fit gives $\tau_{\text{LL}} = 0.29 \pm 0.04$ and $\log N_{\text{HI}} = 16.66 \pm 0.06$. Two closely separated ($\Delta v = 95 \text{ km s}^{-1}$) components are apparent in Ly δ - Ly12 (geocoronal airglow is blended with Ly8 - Ly10). The redder component is the stronger and dominates the LL decrement. We adopt $z_2 = 0.41560$, $\log N_1 = 15.9 \pm 0.05$, $b_1 = 24 \pm 5 \text{ km s}^{-1}$, and $z_2 = 0.41605$, $\log N_2 = 16.45 \pm 0.05$, $b_2 = 35 \pm 5 \text{ km s}^{-1}$, summing to $\log N_{\text{tot}} = 16.56 \pm 0.05$. Because of CoG uncertainties, we adopt the Ly decrement value with an increased error, $\log N_{\text{HI}} = 16.66 \pm 0.08$.

#22: *HB89 0107–025-NED05*, $z_{\text{AGN}} = 0.956$, $z_{\text{abs}} = 0.39909$. — The continuum is well defined above the edge, despite a few AGN emission features (the 700 Å feature from O III and N III observed near 1370 Å). Our fit to the Lyman decrement ($\tau_{\text{LL}} = 0.50 \pm 0.02$) implies $\log N_{\text{HI}} = 16.89 \pm 0.03$. A CoG fit to the system (Ly γ - Ly15) gives $\log N_{\text{HI}} = 16.77 \pm 0.06$ and $b = 25 \pm 2 \text{ km s}^{-1}$. We adopt the Ly decrement solution with a wider the error range, $\log N_{\text{HI}} = 16.89 \pm 0.06$.

#23: *SDSS J084349.49+411741.6*, $z_{\text{AGN}} = 0.989986$, $z_{\text{abs}} = 0.53255$. — The LL optical depth, $\tau_{\text{LL}} = 0.45 \pm 0.02$, implies $\log N_{\text{HI}} = 16.85 \pm 0.02$. However, the decrement is determined by column densities of both system #23 and #51 ($z = 0.53356$), located 198 km s^{-1} to the red. A 2-component CoG to system #23 reproduces the line profiles well with $\log N_{\text{HI}} \approx 16.67 \pm 0.08$. Including $\log N_{\text{HI}} = 16.11 \pm 0.05$ for system #51 gives a total column density $\log N_{\text{tot}} = 16.78 \pm 0.07$. We adopt the Ly decrement value, but widen the error range to $\log N_{\text{HI}} = 16.85 \pm 0.04$.

#24: *SDSS J100535.24+013445.7*, $z_{\text{AGN}} = 1.0809$, $z_{\text{abs}} = 0.41865$. — Three velocity components (denoted #24abc) contribute to the Ly decrement, with optical depth as $\tau_{\text{LL}} = 0.58 \pm 0.04$ ($\log N_{\text{HI}} = 16.96 \pm 0.03$). Because the component splittings are easily separable, $\Delta v_{12} = 216 \text{ km s}^{-1}$ and $\Delta v_{23} = 243 \text{ km s}^{-1}$, we treat these as distinct absorbers, where we adopt: Component 1 ($z_1 = 0.41755$) with $\log N_1 = 14.88 \pm 0.06$, $b_1 = 25 \pm 2 \text{ km s}^{-1}$; Component 2 ($z_2 = 0.41851$) with $\log N_2 = 16.69 \pm 0.04$, $b_2 = 30 \pm 2 \text{ km s}^{-1}$; Component 3 ($z_3 = 0.41966$) with $\log N_3 = 15.91 \pm 0.08$, $b_3 = 22 \pm 2 \text{ km s}^{-1}$, summing to $\log N_{\text{tot}} = 16.76 \pm 0.05$. The LL optical depth is reasonably consistent with this 3-component CoG sum.

#25: *PG 1522+101*, $z_{\text{AGN}} = 1.32785$, $z_{\text{abs}} = 0.72865$. — The decrement ($\tau_{\text{LL}} = 0.26 \pm 0.03$) implies $\log N_{\text{HI}} = 16.62 \pm 0.05$, comparable to values (16.66 ± 0.05 and 16.60 ± 0.04) reported by Lehner et al. (2013) and Stevans et al. (2014). Combined with our CoG fit to the higher Lyman lines, we adopt $\log N_{\text{HI}} = 16.62 \pm 0.05$ and $b = 29 \pm 5 \text{ km s}^{-1}$.

#26: *Q0232–042*, $z_{\text{AGN}} = 1.43737$, $z_{\text{abs}} = 0.73888$. — Our fit to the Ly decrement implies $\log N_{\text{HI}} = 16.77 \pm 0.02$, slightly stronger than the Stevans et al. (2014) CoG solution of 16.64 ± 0.08 and the value 16.72 ± 0.03 from Lehner et al. (2013). Including our CoG fit to the higher Lyman lines, we adopt $\log N_{\text{HI}} = 16.76 \pm 0.05$ and $b = 30 \pm 5 \text{ km s}^{-1}$.

#27: *PG 1522+101*, $z_{\text{AGN}} = 1.32785$, $z_{\text{abs}} = 0.51839$. — Also known as PHL 1377. The AGN continuum appears contaminated by broad emission lines (O IV $\lambda 608$ and O V $\lambda 630$). A weak Ly decrement is visible ($\log N_{\text{HI}} = 16.1–16.3$) with uncertain depth owing to AGN line emission. We performed CoG fits to two closely separated components ($\Delta v = 99 \text{ km s}^{-1}$): Component 1 ($z_1 = 0.5180$, $\log N_1 = 15.64 \pm 0.04$, $b_1 = 15 \pm 1 \text{ km s}^{-1}$) and Component 2 ($z_2 = 0.5185$, $\log N_2 = 16.17 \pm 0.04$, $b_2 = 17 \pm 1 \text{ km s}^{-1}$) summing to $\log N_{\text{tot}} = 16.28 \pm 0.05$. This column density is somewhat larger than that (16.22 ± 0.02) quoted by Lehner et al. (2013) but comparable to that (16.32 ± 0.2) in Stevans et al. (2014). We adopt our summed 2-component CoG solution, $\log N_{\text{tot}} = 16.28 \pm 0.05$, with the error based on combining the CoG with the Ly decrement constraint.

#28: *PG 1338+416*, $z_{\text{AGN}} = 1.21422$, $z_{\text{abs}} = 0.68610$. — This AGN sight line has three strong absorbers in our survey (#28, #29, and #53). The continuum is likely contaminated by AGN broad emission feature of O III and N III near 700 Å (observed near 1550 Å). The fitted Ly decrement ($\tau_{\text{LL}} = 0.188 \pm 0.030$) implies $\log N_{\text{HI}} = 16.47 \pm 0.07$ with the error bar arising from the uncertain placement of the continuum shortward of the LL. From CoG fitting, we adopt $\log N_{\text{HI}} = 16.49 \pm 0.05$ with $b = 20 \pm 5 \text{ km s}^{-1}$, comparable to previous values of 16.45 ± 0.05 (Lehner et al. 2013), 16.49 ± 0.04 (Stevans et al. 2014), and 16.49 ± 0.04 (Tilton et al. 2016).

#29: *PG 1338+416*, $z_{\text{AGN}} = 1.21422$, $z_{\text{abs}} = 0.34885$. — As noted for system #28, the AGN continuum is likely contaminated by AGN broad emission lines, in this case from O IV $\lambda 554$ and Ne V $\lambda 570$ observed between 1240–1260 Å. The Ly decrement ($\tau_{\text{LL}} = 0.147 \pm 0.052$) implies $\log N_{\text{HI}} = 16.37 \pm 0.19$. The higher error arises from uncertain placement of the continuum shortward of the LL. We performed CoG fits to two components separated by $\Delta v = 76 \text{ km s}^{-1}$: Component 1 ($z_1 = 0.34855$, $\log N_1 = 16.28 \pm 0.02$, $b_1 = 32 \pm 1 \text{ km s}^{-1}$) and Component 2 ($z_2 = 0.34889$, $\log N_2 = 15.44 \pm 0.18$, $b_2 = 18 \pm 3 \text{ km s}^{-1}$) summing to $\log N_{\text{tot}} = 16.34 \pm 0.05$. We adopt $\log N_{\text{HI}} = 16.34 \pm 0.10$, comparable to previous values of 16.30 ± 0.13 (Lehner et al. 2013) and 16.37 ± 0.06 (Stevans et al. 2014).

#30: *PKS 0637-752*, $z_{\text{AGN}} = 0.653$, $z_{\text{abs}} = 0.46850$. — The fit to the Ly decrement implies $\log N_{\text{HI}} = 16.48 \pm 0.02$, but the placement of the continuum shortward of the LL is somewhat uncertain. Using CoG fitting of Ly β - Ly17, we find $\log N_{\text{HI}} = 16.43 \pm 0.05$ and $b = 18 \pm 5 \text{ km s}^{-1}$, a column density similar to the value of 16.48 ± 0.04 (Lehner et al. 2013) but higher than 16.08 ± 0.03 (Stevans et al. 2014). We adopt the Ly decrement value with a wider error, $\log N_{\text{HI}} = 16.48 \pm 0.05$.

#31: *SDSS J141910.20+420746.9*, $z_{\text{AGN}} = 0.873501$, $z_{\text{abs}} = 0.28895$. — This AGN sight line has four strong absorbers in our survey (#31, #32, #33, and #50). The AGN continuum is contaminated by the 700 Å emission lines (O III and N III) observed between 1300-1320 Å. The Ly decrement is below the detectable level ($\tau_{\text{LL}} < 0.1$, $\log N_{\text{HI}} < 16.20$). Using CoG fitting, we adopt $\log N_{\text{HI}} = 16.17 \pm 0.05$ with $b = 25 \pm 5 \text{ km s}^{-1}$. This column is the same as quoted by Stevans et al. (2014) but below that (16.40 ± 0.07) quoted in Lehner et al. (2013), which would produce a larger Lyman decrement than observed.

#32: *SDSS J141910.20+420746.9*, $z_{\text{AGN}} = 0.873501$, $z_{\text{abs}} = 0.42555$. — The continuum near the LL (1300 Å observed frame) is not flat, with no obvious decrement ($\tau_{\text{LL}} < 0.15$ and $\log N_{\text{HI}} < 16.38$). This edge is contaminated by the 700 Å broad emission feature of O III and N III (observed between 1300-1315 Å). Using CoG fitting, we adopt $\log N_{\text{HI}} = 16.24 \pm 0.10$ and $b = 23 \pm 3 \text{ km s}^{-1}$. This column density is slightly above previous values of 16.17 ± 0.06 (Lehner et al. 2013) and 16.02 ± 0.02 (Stevans et al. 2014).

#33: *SDSS J141910.20+420746.9*, $z_{\text{AGN}} = 0.873501$, $z_{\text{abs}} = 0.53460$. — The continuum is contaminated by AGN emission lines of Ne VIII and O IV observed between 1445-1475 Å. We see no obvious Ly decrement ($\tau_{\text{LL}} < 0.1$, $\log N_{\text{HI}} < 16.20$). Using CoG fitting, we adopt $\log N_{\text{HI}} = 16.15 \pm 0.10$ and $b = 16 \pm 2 \text{ km s}^{-1}$, a column intermediate between values of $16.34(+0.23, -0.12)$ (Lehner et al. 2013) and 16.06 ± 0.07 (Stevans et al. 2014).

#34: *SDSS J143511.53+360437.2*, $z_{\text{AGN}} = 0.428593$, $z_{\text{abs}} = 0.38766$. — We see a Ly decrement ($\tau_{\text{LL}} = 0.10 \pm 0.03$, $\log N_{\text{HI}} = 16.20 \pm 0.12$) based on a small flux decrement between 1258-1265 Å. Prochaska et al. (2017) quote $\log N_{\text{HI}} < 16.65$ from low-resolution (COS/G140L) data. Using CoG fitting, we adopt $\log N_{\text{HI}} = 16.17 \pm 0.05$ and $b = 32 \pm 5 \text{ km s}^{-1}$. This column density is similar to values of 16.18 ± 0.05 (Lehner et al. 2013) and 16.15 ± 0.02 (Stevans et al. 2014).

#35: *SDSS J094331.61+053134.4*, $z_{\text{AGN}} = 0.564336$, $z_{\text{abs}} = 0.35455$. — Because of continuum undulations (1220-1240 Å), we cannot measure a reliable Ly decrement. CoG fitting gives values identical to those of Lehner et al. (2013) and Stevans et al. (2014). We adopt $\log N_{\text{HI}} = 16.12 \pm 0.05$ with $b = 25 \pm 5 \text{ km s}^{-1}$ from CoG fitting.

#36: *PG 1407+265*, $z_{\text{AGN}} = 0.946$, $z_{\text{abs}} = 0.68270$. — Based on high quality data, we measure a Ly decrement, $\tau_{\text{LL}} = 0.153 \pm 0.012$, implying $\log N_{\text{HI}} = 16.38 \pm 0.03$, comparable to previous values of 16.38 ± 0.02 (Lehner et al. 2013) and 16.39 ± 0.03 (Stevans et al. 2014). Including CoG fitting, we adopt $\log N_{\text{HI}} = 16.38 \pm 0.05$ with $b = 32 \pm 5 \text{ km s}^{-1}$.

#37: *PG 1216+069*, $z_{\text{AGN}} = 0.3313$, $z_{\text{abs}} = 0.28231$. — See Figure 7. Based on high quality data, we measure a Ly decrement, $\tau_{\text{LL}} = 0.16 \pm 0.02$, implying $\log N_{\text{HI}} = 16.40 \pm 0.06$. CoG fitting to Lye - Ly14 gives $\log N_{\text{HI}} = 16.41 \pm 0.03$ and $b = 25 \pm 2 \text{ km s}^{-1}$, comparable to 16.40 ± 0.05 (Lehner et al. 2013).

#38: *SDSS J161916.54+334238.4*, $z_{\text{AGN}} = 0.470946$, $z_{\text{abs}} = 0.26938$. — We see no obvious Ly decrement, but the wavelength calibration near the Lyman edge (1150-1165 Å) is uncertain. Using CoG fitting, we adopt $\log N_{\text{HI}} = 16.40 \pm 0.08$ and $b = 29 \pm 2 \text{ km s}^{-1}$. This column density is similar to previous values 16.48 ± 0.05 (Lehner et al. 2013) and 16.40 ± 0.03 (Stevans et al. 2014).

#39: *SBS 1122+594*, $z_{\text{AGN}} = 0.8514$, $z_{\text{abs}} = 0.55810$. — The AGN continuum near the Ly edge is uncertain, owing to broad emission lines of Ne VIII and O IV observed between 1440-1470 Å. Fitting a continuum below those emission features, we estimate a Ly decrement of $\tau_{\text{LL}} = 0.18 \pm 0.04$ and $\log N_{\text{HI}} = 16.46 \pm 0.08$. We also fit a CoG with three velocity components separated by $\Delta v_{12} = 129 \text{ km s}^{-1}$ and $\Delta v_{23} = 58 \text{ km s}^{-1}$: Component 1 ($z_1 = 0.55748$) with $\log N_1 = 15.79 \pm 0.05$, $b_1 = 27 \pm 3 \text{ km s}^{-1}$; Component 2 ($z_2 = 0.55815$) with $\log N_2 = 16.13 \pm 0.05$, $b_2 = 21 \pm 2 \text{ km s}^{-1}$; Component 3 ($z_3 = 0.55845$) with $\log N_3 = 15.94 \pm 0.05$, $b_3 = 21 \pm 3 \text{ km s}^{-1}$, summing to our adopted value, $\log N_{\text{tot}} = 16.45 \pm 0.06$ with $b = 29 \pm 2 \text{ km s}^{-1}$. This column density is comparable to the value of 16.42 ± 0.02 (Stevans et al. 2014) but above the value 16.24 ± 0.02 of Lehner et al. (2013). The Ly decrement is consistent with our higher value.

#40: *HE 0439-5254*, $z_{\text{AGN}} = 1.053$, $z_{\text{abs}} = 0.61512$. — The AGN continuum below the LL is contaminated by the broad 700 Å emission lines of O III and N III observed between 1445-1455 Å. The continuum below the Ly edge ($\lambda < 1473 \text{ Å}$) is therefore somewhat uncertain. From the Ly decrement, we estimate $\tau_{\text{LL}} = 0.15 \pm 0.03$, implying $\log N_{\text{HI}} = 16.38 \pm 0.08$. We fit a CoG with three velocity components, separated by $\Delta v_{12} = 46 \text{ km s}^{-1}$ and $\Delta v_{23} = 89 \text{ km s}^{-1}$: Component 1 ($z_1 = 0.61495$) with $\log N_1 = 16.2 \pm 0.1$, $b_1 = 18 \pm 2 \text{ km s}^{-1}$; Component 2 ($z_2 = 0.61520$) with $\log N_2 = 15.8 \pm 0.1$, $b_2 = 60 \pm 10 \text{ km s}^{-1}$; Component 3 ($z_3 = 0.61568$) with $\log N_3 = 15.59 \pm 0.15$, $b_3 = 16 \pm 5 \text{ km s}^{-1}$. Our adopted summed total, $\log N_{\text{tot}} = 16.42 \pm 0.10$, is higher than previous values of 16.28 ± 0.04 (Lehner et al. 2013) and 16.25 ± 0.04 (Stevans et al. 2014). We believe our 3-component fitting is more accurate, with a summed column density consistent with the (less certain) Ly decrement.

#41: *B0117-2837*, $z_{\text{AGN}} = 0.348858$, $z_{\text{abs}} = 0.348330$. — The AGN continuum is contaminated by broad emission features of O I (observed at 1265-1275 Å) and C III (observed at 1310-1320 Å) and by an absorption dip (1290-1300 Å). The flux shortward of the LL is complicated by the redward damping wing of Galactic Ly α absorption (1227-1232 Å). The Ly decrement is uncertain, $\tau_{\text{LL}} = 0.16 - 0.20$ or $\log N_{\text{HI}} = 16.40 - 16.50$, and we place more weight on CoG fitting. We fit two closely separated ($\Delta v = 73 \text{ km s}^{-1}$) absorbers at $z_1 = 0.34833$ ($\log N_1 = 15.66 \pm 0.03$) and $z_2 = 0.34866$ ($\log N_2 = 16.00 \pm 0.04$), summing to $\log N_{\text{tot}} = 16.14 \pm 0.04$, well below the estimated Ly decrement. Because of the continuum uncertainty with the Ly decrement, we adopt the summed CoG value, $\log N_{\text{tot}} = 16.16 \pm 0.10$ with an expanded error bar owing to contaminating AGN line emission.

#42: *Ton 576 (SDSS J111754.31+263416.6)*, $z_{\text{AGN}} = 0.420466$, $z_{\text{abs}} = 0.35194$. — This AGN has a well-defined continuum longward of the LL ($\lambda > 1232.6 \text{ Å}$), but the flux recovery shortward of the Ly edge is complicated by damped Galactic Ly α absorption. Our fit to the redward wing of the Galactic DLA suggests $\tau_{\text{LL}} = 0.14 \pm 0.03$ ($\log N_{\text{HI}} = 16.35 \pm 0.08$) for a flat continuum, but a downward-sloping continuum to shorter wavelengths gives $\log N_{\text{HI}} = 16.22 \pm 0.08$. The CoG from Stevans et al. (2014) gave 16.14 ± 0.02 . Our new two-component ($\Delta v = 69 \text{ km s}^{-1}$) CoG fit to Ly δ - Ly9 gives values: $z_1 = 0.35194$, $\log N_1 = 15.89 \pm 0.09$ and $z_2 = 0.35225$, $\log N_2 = 15.70 \pm 0.06$, summing to $\log N_{\text{tot}} = 16.11 \pm 0.10$. We adopt the summed CoG value, with a slightly larger error bar, $\log N_{\text{HI}} = 16.11 \pm 0.12$, reflecting the Ly decrement.

#43: *SDSS J080908.13+461925.6*, $z_{\text{AGN}} = 0.656338$, $z_{\text{abs}} = 0.61917$. — The continuum is not well defined, owing to likely contamination by O I emission (1560-1570 Å observed frame). A weak Ly decrement suggests $\tau_{\text{LL}} = 0.089 \pm 0.015$ or $\log N_{\text{HI}} = 16.15 \pm 0.07$. However, the continuum below the LL is uncertain. We adopt the value from CoG-fitting, $\log N_{\text{HI}} = 16.18 \pm 0.07$ with $b = 36 \pm 2 \text{ km s}^{-1}$.

#44: *3C 57*, $z_{\text{AGN}} = 0.670527$, $z_{\text{abs}} = 0.32332$. — Three velocity components are evident at $z_1 = 0.32257$, $z_2 = 0.32303$, and $z_3 = 0.32342$, with separations ($\Delta v_{12} = 104 \text{ km s}^{-1}$ and $\Delta v_{23} = 88 \text{ km s}^{-1}$). The Ly decrement falls in the Galactic DLA and is unobservable. Our new 3-component CoG fit finds $\log N_1 = 15.61 \pm 0.03$, $\log N_2 = 15.45 \pm 0.03$, and $\log N_3 = 16.12 \pm 0.09$, summing to $\log N_{\text{tot}} = 16.30 \pm 0.12$ and similar to the value 16.29 ± 0.01 (Stevans et al. 2014). We adopt a column density, $\log N_{\text{HI}} = 16.30 \pm 0.05$, consistent with both CoG and Ly decrement.

#45: *SDSS J113457.62+255527.9*, $z_{\text{AGN}} = 0.710078$, $z_{\text{abs}} = 0.43233$. — A new CoG fit gives $\log N_{\text{HI}} = 16.47 \pm 0.06$, whereas Stevans et al. (2014) quoted 16.40 ± 0.03 . The continuum is fairly well defined, but portions may be contaminated by broad emission lines of Ne VIII and O IV observed at 1320-1350 Å. The Ly decrement implies $\tau_{\text{LL}} = 0.19 \pm 0.020$ and $\log N_{\text{HI}} = 16.48 \pm 0.05$. With the CoG information, we adopt $\log N_{\text{HI}} = 16.48 \pm 0.06$.

#46: *SDSS J124511.25+335610.1*, $z_{\text{AGN}} = 0.711698$, $z_{\text{abs}} = 0.71297$. — There are three strong absorbers in this sight line, including systems #19 and #20. Absorbers #20 and #46 have a complex flux recovery between 1540-1560 Å, as the envelope of higher Lyman lines from system #46 ($z = 0.71297$) merges with the LL of system #20 ($z = 0.68918$). Our fit to the Ly decrement gives $\log N_{\text{HI}} = 16.52 \pm 0.05$.

#47: *SDSS J143726.14+504558.8*, $z_{\text{AGN}} = 0.783319$, $z_{\text{abs}} = 0.77248$. — The data quality is poor, and the continuum has likely contamination from AGN emission lines of O I observed at 1670-1690 Å and C III $\lambda 977$ observed at 1740 Å. No Ly decrement is evident to a limit $\log N_{\text{HI}} < 16.6$. Because the component splittings are easily separable, $\Delta v_{12} = 390 \text{ km s}^{-1}$ and $\Delta v_{23} = 230 \text{ km s}^{-1}$, we treat these as distinct absorbers, denoted #47abc, where $z_1 = 0.76890$ ($\log N_1 = 16.15 \pm 0.07$), $z_2 = 0.77120$ ($\log N_2 = 15.4 \pm 0.2$), and $z_3 = 0.77255$ ($\log N_3 = 16.26 \pm 0.10$). The middle component is poorly constrained, with a CoG based on only Ly γ , Ly δ , and Ly ϵ . The summed CoG fit gives $\log N_{\text{tot}} = 16.26 \pm 0.11$ with $b = 40 \pm 6 \text{ km s}^{-1}$.

#48: *SDSS J234500.43-005936.0*, $z_{\text{AGN}} = 0.789429$, $z_{\text{abs}} = 0.253900$. — Because no data were taken at $\lambda < 1164 \text{ Å}$, we cannot measure the Ly decrement (at 1143 Å). We rely on a 2-component CoG solution, which gives $\log N_1 = 15.85 \pm 0.10$ and $b_1 = 25 \pm 3 \text{ km s}^{-1}$ (blue component with Ly ϵ and Ly ζ) and $\log N_2 = 15.77 \pm 0.16$, $b_1 = 41 \pm 12 \text{ km s}^{-1}$ (red component with Ly β to Ly ζ). These column densities sum to $\log N_{\text{tot}} = 16.11 \pm 0.13$.

#49: *SDSS J101622.60+470643.3*, $z_{\text{AGN}} = 0.821527$, $z_{\text{abs}} = 0.72766$. — No clear Ly decrement is seen ($\log N_{\text{HI}} < 16.34$). The continuum is uncertain longward of the LL because of AGN emission lines. Our CoG fit uses Ly β to Ly10 to find $\log N_{\text{HI}} = 16.16 \pm 0.09$ with $b = 19 \pm 2 \text{ km s}^{-1}$.

#50: *SDSS J141910.20+420746.9*, $z_{\text{AGN}} = 0.873501$, $z_{\text{abs}} = 0.84523$. — A weak Ly decrement may be present with $\log N_{\text{HI}} = 16.23 \pm 0.15$, with an uncertain continuum redward of the edge owing to O I emission lines observed at 1770-1790 Å. We fit a CoG to Ly δ up to Ly10, with our adopted value $\log N_{\text{HI}} = 16.23 \pm 0.05$ and $b = 29 \pm 2 \text{ km s}^{-1}$.

#51: *SDSS J084349.49+411741.6*, $z_{\text{AGN}} = 0.989986$, $z_{\text{abs}} = 0.53556$. — The source has a well-defined continuum, with a Ly decrement suggesting $\tau_{\text{LL}} = 0.41 \pm 0.02$ or $\log N_{\text{HI}} = 16.81 \pm 0.02$ for a flat continuum. This decrement includes both systems #23 and #51. However, system #23 at $z = 0.53255$ is easily separable in the Lyman lines, lying 178 km s^{-1} blueward. These absorbers are visible in blended Lyman lines (Ly γ , Ly δ , Ly ϵ) at redshifts $z_1 = 0.53255$ for system #23 ($\log N_1 = 16.67 \pm 0.05$) and $z_2 = 0.5355$ for system #51 ($\log N_2 = 16.11 \pm 0.05$). Their column densities sum to $\log N_{\text{HI}} = 16.78 \pm 0.05$, consistent with the decrement. In our statistics, we treat systems #23 and #51 as distinct absorbers, since they are easily separable in the Lyman absorption lines.

#52: *SDSS J100535.24+013445.7*, $z_{\text{AGN}} = 1.0809$, $z_{\text{abs}} = 0.83938$. — The source has a well-defined continuum, with LL optical depth $\tau_{\text{LL}} = 0.41 \pm 0.03$ ($\log N_{\text{tot}} = 16.82 \pm 0.04$) produced by absorption from system #12 at $z_1 = 0.83711$ and system #52 at $z_2 = 0.83938$. These two systems are easily distinguished, separated by $\Delta v \approx 390 \text{ km s}^{-1}$ in the Lyman lines (Ly γ , Ly δ , Ly ϵ). Our CoG gives $\log N_{\text{HI}} = 16.09 \pm 0.05$ for system #52. The combined column densities of #12 and #52 are consistent with the Ly decrement.

#53: *PG 1338+416*, $z_{\text{AGN}} = 1.21422$, $z_{\text{abs}} = 0.62075$. — This AGN sight line has three absorbers with Lyman edges near 1537 Å (system #28), 1478 Å (system #53), and 1225 Å (system #29). The continuum between 1540-1580 Å is contaminated by broad emission lines of O II and O III (rest-frame 833-834 Å). For this system, the weak Ly decrement at 1478 Å is poorly determined. CoG fitting gives $\log N_{\text{HI}} = 16.17 \pm 0.06$ for #53, consistent with that found by Tilton et al. (2016).

#54: *Q 0232-042*, $z_{\text{AGN}} = 1.43747$, $z_{\text{abs}} = 0.322450$. — This AGN is also known as PHL 1377 (see also system #26). No Lyman decrement is evident. Our CoG fit gives $\log N_{\text{HI}} = 16.14 \pm 0.04$ with $b = 34 \pm 2 \text{ km s}^{-1}$.

#55: *PG 0003+158*, $z_{\text{AGN}} = 0.4509$, $z_{\text{abs}} = 0.3478$. — The data have high S/N, and a Lyman series is evident up to Ly 12 with higher lines intruding on the red wing of the Galactic DLA. We use the excellent CoG fit with $\log N_{\text{HI}} = 16.10 \pm 0.03$ with $b = 17 \pm 1 \text{ km s}^{-1}$, consistent with a weak LL flux decrement.

#56: *SDSS J161916.54+334238.4*, $z_{\text{AGN}} = 0.470946$, $z_{\text{abs}} = 0.44231$. — This AGN also contains system #15 (Lyman edge at 1341 Å) and a DLA at 1333 Å ($z_{\text{abs}} = 0.0963$ –see Table 7). This DLA blocks the LL of system #56 as well as lines of Ly7 - Ly9. A good CoG fit using Ly α to Ly6 plus Ly10 and Ly11 yields $\log N_{\text{HI}} = 15.90 \pm 0.06$ with $b = 26 \pm 2 \text{ km s}^{-1}$.

#57: *PG 0637-752*, $z_{\text{AGN}} = 0.653$, $z_{\text{abs}} = 0.24326$. — The LL at 1133.5 Å falls just below the COS/G130M data range, and blueward continuum is not visible. However, a CoG fit to Ly γ , Ly ϵ , Ly8, and Ly10 gives $\log N_{\text{HI}} = 15.81 \pm 0.05$ with $b = 22 \pm 2 \text{ km s}^{-1}$.

#58: *PKS 0552-640*, $z_{\text{AGN}} = 0.68$, $z_{\text{abs}} = 0.446$. — A CoG fit to Ly β through Ly14 gives a very good fit with $\log N_{\text{HI}} = 15.96 \pm 0.02$ and $b = 28 \pm 1 \text{ km s}^{-1}$. This column density is consistent with a weak LL decrement visible in very good data.

#59: *SDSS J124511.25+335610.1*, $z_{\text{AGN}} = 0.717$, $z_{\text{abs}} = 0.63215$. — The data quality is poor, with no obvious Ly decrement. A double-component structure is seen in Ly β through Ly8, easily separable as components denoted #59ab. A two-component CoG gives a reasonable fit, with $z_1 = 0.63190$ ($\log N_1 = 15.83 \pm 0.10$, $b_1 = 17 \pm 1 \text{ km s}^{-1}$) and $z_2 = 0.63245$ ($\log N_2 = 15.80 \pm 0.06$, $b_2 = 36 \pm 2 \text{ km s}^{-1}$) summing to $\log N_{\text{HI}} = 16.12 \pm 0.10$.

#60: *SBS 1108+560*, $z_{\text{AGN}} = 0.766619$, $z_{\text{abs}} = 0.28646$. — This sight line has a very strong LLS (system #9) to the red of absorber #60. In the low-flux region blueward of #9 we see two strong velocity components (separation $\Delta v = 233 \text{ km s}^{-1}$) in Ly α through Ly9, with considerable blending from other absorption. Because the components are easily separable, we treat these as distinct absorbers, denoted #60ab. Individual CoG fits to these features give: $z_1 = 0.2855$ ($\log N_1 = 16.12 \pm 0.09$, $b_1 = 34 \pm 2 \text{ km s}^{-1}$) and $z_2 = 0.2865$ ($\log N_2 = 16.14 \pm 0.07$, $b_2 = 57 \pm 3 \text{ km s}^{-1}$) summing to $\log N_{\text{HI}} = 16.43 \pm 0.08$. The implied $\tau_{\text{LL}} = 0.17$ is difficult to confirm, given the poor data at 1173 Å and the likely presence of AGN broad emission lines of O III and N III (1150-1170 Å observed frame).

#61: *SDSS J143726.14+504555.8*, $z_{\text{AGN}} = 0.783319$, $z_{\text{abs}} = 0.250650$. — The LL at 1140 Å is barely within the COS/G130M data range. The data are quite noisy, and several Lyman lines are blocked (Ly γ) or contaminated by other absorption (Ly7). A CoG fit with $\log N_{\text{HI}} = 16.27 \pm 0.08$ and $b = 24 \pm 2 \text{ km s}^{-1}$ implies a Ly decrement with $\tau_{\text{LL}} = 0.12$ that is hard to confirm. However, this column density over-predicts the line profiles of Ly8, Ly9, and Ly10. We widen the error and adopt $\log N_{\text{HI}} = 16.27 \pm 0.12$.

#62: *SDSS J234500.43-005936.0*, $z_{\text{AGN}} = 0.789429$, $z_{\text{abs}} = 0.54818$. — The data quality is quite good, with no LL decrement visible at 1411.6 Å. We see hints of two velocity components ($\Delta v \approx 40 \text{ km s}^{-1}$) with extra absorption in asymmetric red wings of Ly ϵ through Ly10. A two-component CoG gives $\log N_1 = 15.63 \pm 0.07$ and $\log N_2 = 16.10 \pm 0.17$, summing to 16.23. We adopt a single-component CoG to Ly β through Ly12 which gives $\log N_{\text{HI}} = 16.16 \pm 0.06$ and $b = 26 \pm 2 \text{ km s}^{-1}$.

#63: *SDSS J101622.60+470643.3*, $z_{\text{AGN}} = 0.821527$, $z_{\text{abs}} = 0.66475$. — This sight line includes system #49 ($z_{\text{abs}} = 0.727$). The continuum longward of the LL (1520-1540 Å) may be contaminated by AGN emission lines (O II and O III at 833-834 Å rest-frame). A CoG fit to Ly β through Ly9 gives $\log N_{\text{HI}} = 15.99 \pm 0.03$ with $b = 28 \pm 1 \text{ km s}^{-1}$.

#64: *SBS 1122+594*, $z_{\text{AGN}} = 0.8514$, $z_{\text{abs}} = 0.67835$. — This sight line also includes system #39 ($z_{\text{abs}} = 0.5581$). The data quality is high, with a well-constrained CoG fit: $\log N_{\text{HI}} = 16.06 \pm 0.04$ and $b = 19 \pm 1 \text{ km s}^{-1}$. The observed weak Ly decrement is consistent with this column density.

#65: *SDSS J141910.20+420746.0*, $z_{\text{AGN}} = 0.873501$, $z_{\text{abs}} = 0.52221$.— This sight line also includes systems #31, #32, #33, #50, and #66. Systems #31 and #32 are at much lower redshifts, and system #50 is at a much higher redshift ($z = 0.84523$). System #33 has a somewhat higher redshift ($z = 0.53460$) but widely separated ($\Delta v = 2440 \text{ km s}^{-1}$). The data quality is not good, and no Ly decrement is apparent. A CoG fit to Ly β , Ly γ , Ly δ , Ly ϵ , and Ly7 gives $\log N_{\text{HI}} = 15.87 \pm 0.07$ with $b = 37 \pm 2 \text{ km s}^{-1}$.

#66: *SDSS J141910.20+420746.0*, $z_{\text{AGN}} = 0.873501$, $z_{\text{abs}} = 0.80463$.— This sight line also includes systems #31, #32, #33, #50, and #66. Systems #31 and #32 are at much lower redshifts, and system #50 is at somewhat higher redshift ($z = 0.84523$), although it produces no visible Ly decrement at the location of system #66 (1645.4 Å). The Ly γ line is strong, and lines of Ly δ to Ly ζ show two velocity components ($\Delta v = 66 \text{ km s}^{-1}$) which we fit with CoGs to find: $z_1 = 0.8044$ ($\log N_1 = 15.71 \pm 0.22$, $b_1 = 16 \pm 3 \text{ km s}^{-1}$) and $z_2 = 0.8047$ ($\log N_2 = 15.75 \pm 0.06$, $b_2 = 19 \pm 2 \text{ km s}^{-1}$) summing to $\log N_{\text{HI}} = 16.03 \pm 0.15$.

#67: *FBQS J0751+2919*, $z_{\text{AGN}} = 0.915$, $z_{\text{abs}} = 0.82902$.— The data are of very high quality data with a weak Ly decrement. A CoG fit to Ly δ through Ly12 gives $\log N_{\text{HI}} = 16.06 \pm 0.02$ with $b = 34 \pm 2 \text{ km s}^{-1}$.

#68: *PG 1407+265*, $z_{\text{AGN}} = 0.946$, $z_{\text{abs}} = 0.59964$.— The data are of very high quality data, but no Ly decrement is visible. A CoG fit to Ly γ through Ly12 gives $\log N_{\text{HI}} = 16.08 \pm 0.04$ with $b = 14 \pm 1 \text{ km s}^{-1}$.

#69: *LBQS 0107–0235*, $z_{\text{AGN}} = 0.957039$, $z_{\text{abs}} = 0.536$.— The data are of very high quality data, but no Ly decrement is visible. Two broad, well-separated absorption components ($\Delta v = 142 \text{ km s}^{-1}$) are seen in Ly β through Ly ϵ , with the stronger (redder) component visible up to Ly10. A two-component CoG fit finds: $z_1 = 0.53572$ ($\log N_1 = 15.42 \pm 0.05$, $b_1 = 40 \pm 9 \text{ km s}^{-1}$) and $z_2 = 0.53645$ ($\log N_2 = 15.66 \pm 0.05$, $b_2 = 40 \pm 7 \text{ km s}^{-1}$) summing to $\log N_{\text{HI}} = 15.86 \pm 0.05$.

#70: *LBQS 0107–0235*, $z_{\text{AGN}} = 0.957039$, $z_{\text{abs}} = 0.87636$.— A very weak Ly decrement may be present, consistent with $\log N_{\text{HI}} < 16.1$. A CoG fit to Ly δ through Ly12 gives $\log N_{\text{HI}} = 15.96 \pm 0.04$ with $b = 30 \pm 5 \text{ km s}^{-1}$.

#71: *PG 1522+101*, $z_{\text{AGN}} = 1.32785$, $z_{\text{abs}} = 0.67518$.— This sight line also includes systems #25 ($z = 0.72865$), which produces a Ly decrement at 1576 Å redward of system #71 and #27 ($z = 0.51839$). System #71 consists of two absorption components, separated by $\Delta v \approx 72 \text{ km s}^{-1}$, which we fit with: $z_1 = 0.6748$ ($\log N_1 = 15.39 \pm 0.05$, $b_1 = 27 \pm 2 \text{ km s}^{-1}$) and $z_2 = 0.6752$ ($\log N_2 = 15.71 \pm 0.04$, $b_2 = 42 \pm 4 \text{ km s}^{-1}$) summing to $\log N_{\text{HI}} = 15.88 \pm 0.05$.

#72: *PG 1630+377*, $z_{\text{AGN}} = 1.47607$, $z_{\text{abs}} = 0.91449$.— Owing to its high redshift (for this survey), the COS spectra show absorption in Ly ϵ through Ly10, but no Ly decrement is visible. There appear to be two velocity components ($\Delta v = 66 \text{ km s}^{-1}$) with a stronger blue component ($z_1 = 0.9143$, $\log N_{\text{HI}} = 15.67 \pm 0.04$, but a poorly constrained doppler parameter, $b = 99 \pm 49 \text{ km s}^{-1}$). A weaker red component at $z_2 = 0.9148$ is only reliably detected in Ly ϵ through Ly7, with a poorly constrained column density, $\log N_{\text{HI}} = 15.4 \pm 0.2$. The total system has $\log N_{\text{HI}} = 15.86 \pm 0.10$,

#73: *SDSS 161649.42+415416.3*, $z_{\text{AGN}} = 0.440417$, $z_{\text{abs}} = 0.3211$.— This DLA did not appear in the Stevans et al. (2014) list, but we found it in our new examination through its Lyman edge at 1204.5 Å. Meiring et al. (2011) and Battisti et al. (2012) quote $\log N_{\text{HI}} = 20.60 \pm 0.20$ from fitting the Ly α damping wings. Our CoG fit to Ly β and Ly δ - Ly8 yields a somewhat smaller column density, $\log N_{\text{HI}} = 20.34 \pm 0.12$ with $b = 49 \pm 2 \text{ km s}^{-1}$. Stevans et al. (2014) listed no other strong H I absorbers in this sightline with $\log N_{\text{HI}} > 15.5$.

APPENDIX B: MAXIMUM-LIKELIHOOD FITTING OF THE PLLS DISTRIBUTION

Following the convention in studies of quasar absorption lines (Weymann et al. 1998; Kim et al. 2002, among many others), we express the column density distribution as separable power laws in column density, N , and redshift, z ,

$$f(N, z) \equiv \frac{d^2 \mathcal{N}_{\text{abs}}}{dz dN} = C_0 N^{-\beta} (1+z)^\gamma. \quad (\text{B1})$$

As presented in Tables 3-4, the pLLS and LLS absorbers are allocated to bins in z and $\log N$, with the survey sensitivity expressed through the effective redshift, Δz_{eff} , covered by QSOs in our sample. Many studies (e.g., Janknecht et al. 2006; O’Meara et al. 2013) including our previous work (e.g., Danforth et al. 2016, and references therein) have employed variants of least-squares fitting of $f(N, z)$ to binned histograms in order to determine β and γ . This approach has several benefits, most notably its illustrative value in plots or tables and its computational simplicity in the presence of measurement errors and search pathlengths that may vary as functions of N and z . In the limit of small bins of zero uncertainty, it tends toward the maximum-likelihood results. However, in the presence of finite binned data, this least-squares approach does not generally yield the maximum-likelihood estimates of the parameters for power-law distributions (Newman 2005; Clauset et al. 2009) and it introduces systematic biases in the fit parameters and their confidence intervals³. Because of the prevalence of binned fits in the literature, it is worth explaining in detail the maximum-likelihood approach to obtaining these parameters, as implemented in the present study.

From Equation B1, the likelihood function for a dataset of \mathcal{N} absorbers given the parameters β and γ is

$$\mathcal{L}(\vec{P}(N, z) | \beta, \gamma) = \prod_{i=1}^{\mathcal{N}} \left(\int_{\text{out}} P_i(N, z) dN dz + C_0 \int_{z_{\min}}^{z_{\max}} \int_{N_{\min}}^{N_{\max}} P_i(N, z) N^{-\beta} (1+z)^\gamma w(N, z) dN dz \right). \quad (\text{B2})$$

Here, $P_i(N, z)$ is the normalized probability density distribution for measurements of N and z for absorber i , and $w(N, z)$ is a weight function that accounts for the surveyed pathlength in z . The first term in Equation B2 represents the total probability that absorber i is outside the range in z or N over which we wish to fit the free parameters.

The normalized distribution $P_i(N, z)$ characterizes the data-derived uncertainties and correlations in the measurements, which will depend on factors such as data quality and line-fitting techniques, and it introduces the need to evaluate the double-integral in Equation B2. In moderate resolution spectra, such as the COS G130M and G160M data used in this study, the uncertainty in redshift determination is quite small, and we neglect it. We assume that $P_i(N, z) \approx P_i(N) \delta(z - z_i)$ where z_i is the measured redshift of the absorber, although this assumption is not valid for all datasets used in IGM studies. The column density measurements, on the other hand, can be subject to substantial and widely varying uncertainty that can potentially affect the derived parameters. Following Stevans et al. (2014), we assume that $P(N)$ is a log-normal distribution defined by the measured column density parameters from Table 2 in Stevans et al. (2014) with modifications listed in Table 6 of the present paper. The one exception is the absorber at $z = 0.47379$ in the SDSSJ154553.48+093620.5 sightline, for which we have only upper and lower limits ($17.9 < \log N < 19.0$) and treat as a uniform distribution over that interval.

The function $w(N, z)$ gives the number of observed targets over which an absorber of column density N and redshift z could have been observed. Put another way, the integral of this function is the aforementioned effective pathlength over a given redshift and column density interval, $\Delta z_{\text{eff}} = \int \int w(N, z) dN dz$. In general, such a function depends on properties of the observations, including but not limited to the observed wavelengths, the redshifts of the background AGNs, and the wavelength-dependent signal-to-noise ratios of the spectra. Often, this function must be evaluated numerically, but in some cases simplifying assumptions can be made. Because the present study is concerned only with relatively strong H I absorbers in high signal-to-noise, well-resolved data, we assume that w is a function only of z and can be expressed as

$$w(N, z) \approx w(z) \approx \sum_{j=1}^{\mathcal{N}_{\text{AGN}}} [H(z - z_{\min,j}) - H(z - z_{\max,j})], \quad (\text{B3})$$

where $H(x)$ is the Heaviside step function and $z_{\min,j}$ and $z_{\max,j}$ are the minimum and maximum redshifts at which an absorber could be detected in sightline j , respectively.

Note that if all of the measured column densities and redshifts had no measurement errors and the pathlength was independent of N and z , the likelihood function would remain a pure power law. If upper integration limits are further allowed to go to infinity, it becomes straightforward to derive analytical formulae for a maximum-likelihood power-law exponent and its uncertainty, as shown in Newman (2005), Clauset et al. (2009), and references therein. Several authors have used these formulae to calculate β and/or γ (e.g., Tytler 1987a,b; Storrie-Lombardi et al. 1994; Stengler-Larrea et al. 1995; Songalia & Cowie 2010; Ribaldo et al. 2011a; Rudie et al. 2013). However, typical IGM

³ Discussion of these effects are given in published papers (Goldstein et al. 2004; Newman 2005; Clauset et al. 2009 and sub-

sequent on-line revisions, found in <https://arxiv.org/abs/cond-mat/0412004> and <http://arxiv.org/abs/0706.1062>.

surveys have a completeness function that varies strongly with N and z , as well as large uncertainties in N that span a wide range of magnitudes depending on z and their location on the CoG. Thus, these surveys may not sufficiently approximate the assumptions of such analytical formulae. In general, the approach of using these formulae introduces a systematic bias in the derived power-law exponents. Although the simplifications chosen for the present study maintain the separability of the likelihood function and thus the independence of the two fit parameters, this is not necessarily true for all possible forms of $w(N, z)$ and $P(N, z)$, which could introduce correlations between β and γ . In such a case, each term in Equation B2 must be explicitly evaluated as a two-dimensional integral at each step in the optimization process. These calculations are not computationally prohibitive, even if they must be performed numerically in the absence of an analytical solution.

The normalization C_0 is fixed by β and γ under the requirement that each observed absorber's existence has unity probability within the dataset. It can be evaluated as

$$C_0 = \mathcal{N}' \left[\int_{z_{\min}}^{z_{\max}} \int_{N_{\min}}^{N_{\max}} N^{-\beta} (1+z)^\gamma w(N, z) dN dz \right]^{-1}, \quad (\text{B4})$$

where the limits of integration are the search ranges of the survey and the single power-law approximation remains valid. In our standard fits, we set $(N_{\min}, N_{\max}) = (10^{15} \text{ cm}^{-2}, 10^{20} \text{ cm}^{-2})$ and $(z_{\min}, z_{\max}) = (0.24, 0.84)$, as discussed in Section 3.1. In Equation B4, we introduced the variable \mathcal{N}' (in contrast to the unprimed \mathcal{N}). This distinction is necessary to maintain definitional consistency of C_0 while accounting for the effects of the finite limits of integration in the second term of Equation B2, which may allow a fraction of $P(N, z)$ to fall outside the region of integration, into the first term of Equation B2. Therefore, \mathcal{N}' is the non-integer number of (fractional) absorbers contributing to the likelihood function,

$$\mathcal{N}' = \sum_{i=1}^{\mathcal{N}} \mathcal{N}'_i = \sum_{i=1}^{\mathcal{N}} \int_{z_{\min}}^{z_{\max}} \int_{N_{\min}}^{N_{\max}} P_i(N, z) dN dz, \quad (\text{B5})$$

where \mathcal{N}'_i is the individual fractional contribution of an absorber i .

Using each of our assumptions with Equation B2 and taking the logarithm for computational convenience, we obtain the log-likelihood function that we use for optimization of β and γ in the present study:

$$\ln \mathcal{L}(\vec{P}(N), \vec{z} | \beta, \gamma) = \sum_{i=1}^{\mathcal{N}} \ln \left(\int_{-\infty}^{N_{\min}} P_i(N) dN + \int_{N_{\max}}^{\infty} P_i(N) dN + C_0 (1+z_i)^\gamma w(z_i) \int_{N_{\min}}^{N_{\max}} P_i(N) N^{-\beta} dN \right). \quad (\text{B6})$$

For our dataset, the second term within the logarithm in Equation B6 is negligibly small and therefore not evaluated. Because this likelihood function contains multiple numerical integrals that must be evaluated for each absorber, it can be computationally expensive to evaluate for some choices of $P(N)$ and (N_{\min}, N_{\max}) . For this reason, we optimize the likelihood function and determine β and γ by sampling the posterior probability distribution with version 2.1.0 of **emcee** (Foreman-Mackey et al. 2013), which implements the affine-invariant Markov-chain Monte Carlo (MCMC) ensemble sampler from Goodman & Weare (2010). We adopt uniform priors over $-5 < \gamma < 10$ and $0 < \beta < 10$. We initialize 250 walkers randomly over the domain, allowing each to take 250 steps, the first 75 of which are discarded as a burn-in period.

This MCMC procedure yields median values of $\beta = 1.48 \pm 0.05$ and $\gamma = 1.14^{+0.88}_{-0.89}$, and $C_0 = 2.07 \times 10^7$ (for N in cm^{-2}). The error bars indicate the 1σ quantiles around the median in the highly-Gaussian, marginalized posterior probability distributions. Figures 12 and 13 show the fits and differential distributions.

TABLE 1
Detectability Ranges for H I Lyman Absorption^a

Feature	λ_0 (Å)	f	$\log N_{\text{HI}}$ $N_{\text{HI}} \text{ (cm}^{-2}\text{)}$	$(z_{\min} - z_{\max})$ (G130M)	$(z_{\min} - z_{\max})$ (G160M)
Ly α	1215.67	0.4164	12.96	0.002 – 0.200	0.152 – 0.477
Ly β	1025.72	0.07912	13.83	0.107 – 0.422	0.365 – 0.750
Ly γ	972.54	0.02900	14.31	0.167 – 0.500	0.440 – 0.846
Ly δ	949.74	0.01394	14.65	0.195 – 0.536	0.474 – 0.890
Ly ϵ	937.80	0.007804	14.92	0.210 – 0.556	0.493 – 0.914
Ly ζ	930.75	0.004816	15.13	0.219 – 0.568	0.504 – 0.929
Ly η	926.23	0.003813	15.32	0.225 – 0.575	0.512 – 0.938
Ly θ	923.15	0.002216	15.48	0.229 – 0.581	0.517 – 0.944
LL	911.75		16.20	0.245 – 0.600	0.536 – 0.969

^a Detectability ranges in redshift (z_{\min} and z_{\max}) for the first eight Lyman lines (and Lyman limit) of H I. Columns 2 and 3 show the absorption oscillator strengths (f) and wavelengths (λ). Column 3 gives the H I column density detectable in Lyman-series absorption at 50 mÅ equivalent width, $N_{\text{HI}} = (5.65 \times 10^{18} \text{ cm}^{-2})[f \lambda(\text{Å})]^{-2}$, or in a 10% flux decrement at the Lyman edge. Last two columns show redshift coverage for HST/COS observations in gratings G130M (1134–1459 Å) and G160M (1400–1795 Å). Because we usually detect an absorber pattern from Ly α through Ly ϵ our survey should be complete for $\log N_{\text{HI}} \geq 15$. However, most LL decrements would be undetected at $\log N_{\text{HI}} < 16.2$.

TABLE 2
Line Overlap Parameters (Higher Lyman Lines)^a

Lyman (n)	λ_0 (Å)	$\Delta\lambda_{n,n+1}$	f_n (in 10^{-4})	$\tau_0^{(n)}$ ($\times N_{17}/b_{25}$)
Ly12	917.1805	0.949 Å	7.231	3.97
Ly13	916.4291	0.751 Å	5.777	3.17
Ly14	915.8238	0.605 Å	4.689	2.57
Ly15	915.3289	0.495 Å	3.858	2.12
Ly16	914.9192	0.410 Å	3.212	1.76
Ly17	914.5762	0.343 Å	2.703	1.48
Ly18	914.2861	0.290 Å	2.297	1.26
Ly19	914.0385	0.248 Å	1.968	1.08
Ly20	913.8256	0.213 Å	1.699	0.930
Ly21	913.6411	0.185 Å	1.477	0.808
Ly22	913.4803	0.161 Å	1.293	0.707
Ly23	913.3391	0.141 Å	1.137	0.622
Ly24	913.2146	0.125 Å	1.006	0.550

^a Wavelength separations ($\Delta\lambda_{n,n+1}$) between Lyman transitions, λ_n and λ_{n+1} , and optical depths, $\tau_0^{(n)}$. Here, Ly n denotes transition from $(n+1)p \rightarrow 1s$, and line-center optical depth $\tau_0^{(n)} = (0.5474) N_{17} b_{25}^{-1} f_{-4} \lambda_{914}$, with $N_{\text{HI}} = (10^{17} \text{ cm}^{-2}) N_{17}$ and doppler parameter scaled to $b = 25 \text{ km s}^{-1}$. Oscillator strengths f_n (in units of 10^{-4}) and wavelengths (λ_0 scaled to 914 Å) are from Morton (2003).

TABLE 3
Absorber Distribution in Redshift and Column Density^a

z -bin	1	2	3	4	5	6	7	8	9	10	11	12	13	14	15	N_{tot}	Redshifts
($i=1$)	2	0	4	5	5	3	2	1	2	2	0	0	1	0	1	[28]	0.24 – 0.28
($i=2$)	0	5	1	5	2	4	1	0	3	2	0	0	0	0	1	[24]	0.28 – 0.32
($i=3$)	1	1	1	1	2	4	3	0	5	2	0	0	1	0	2	[23]	0.32 – 0.36
($i=4$)	0	1	3	5	5	0	1	0	1	0	0	2	0	0	1	[19]	0.36 – 0.40
($i=5$)	0	0	3	8	3	1	6	1	1	1	2	1	0	1	0	[28]	0.40 – 0.44
($i=6$)	0	1	1	0	1	4	2	2	0	1	0	1	0	1	1	[15]	0.44 – 0.48
($i=7$)	0	0	1	0	3	0	3	0	0	2	1	0	0	0	0	[10]	0.48 – 0.52
($i=8$)	1	0	0	0	2	1	2	2	3	2	0	1	0	0	0	[14]	0.52 – 0.56
($i=9$)	0	0	1	0	3	2	3	0	1	0	0	0	0	0	0	[11]	0.56 – 0.60
($i=10$)	0	0	1	1	1	2	3	2	1	1	1	0	0	0	0	[12]	0.60 – 0.64
($i=11$)	0	0	0	0	2	0	1	2	1	0	0	0	0	0	0	[6]	0.64 – 0.68
($i=12$)	0	0	0	0	0	2	3	0	0	2	2	0	0	0	0	[9]	0.68 – 0.72
($i=13$)	0	0	0	0	0	2	0	0	1	0	1	1	0	0	0	[5]	0.72 – 0.76
($i=14$)	0	0	0	1	0	0	1	0	0	0	0	0	0	0	0	[2]	0.76 – 0.80
($i=15$)	0	0	0	0	2	0	3	0	3	0	1	0	0	0	0	[9]	0.80 – 0.84
Total	4	8	16	26	31	25	34	10	22	15	8	6	2	2	6	[215]	0.24 – 0.84

^a Array $F(i, j)$ shows the number of H I absorbers per bin, with total numbers summed across rows and columns. In total, this table lists 211 absorbers: 158 ($\log N_{\text{HI}} \geq 15.0$), 60 ($\log N_{\text{HI}} \geq 16.0$), and 10 ($\log N_{\text{HI}} \geq 17.0$). Labels (i, j) denote redshift bins ($i = 1 - 15$) of width $\Delta z = 0.04$ from $0.24 \leq z \leq 0.84$ and column-density bins ($j = 1 - 15$) of width $\Delta \log N_{\text{HI}} = 0.25$ except for bins 13, 14, 15. Column density ranges of bins are: (1) $\log N_{\text{HI}} = 14.00-14.25$, (2) $14.25-14.50$, (3) $14.50-14.75$, (4) $14.75-15.00$, (5) $15.00-15.25$, (6) $15.25-15.50$, (7) $15.50-15.75$, (8) $15.75-16.00$, (9) $16.00-16.25$, (10) $16.25-16.50$, (11) $16.50-16.75$, (12) $16.75-17.00$, (13) $17.00-17.50$, (14) $17.50-18.00$, (15) $\log N_{\text{HI}} \geq 18.00$. Five absorbers (Systems #4, 10, 50, 70, 72 in Appendix A) lay at redshifts outside the range of this table. Although they do not appear in the numbers above, they are included in the MCMC analysis of Appendix B.

TABLE 4
Redshift Distribution of H I Absorbers

Bin (i)	Redshift Range	(N_{AGN}) ^a	(N_{abs}) ^b	(Δz_{eff}) ^{(i) a}	(dN/dz) ^b
1	0.24 – 0.28	102	17 (28)	3.83	4.44(+1.36, -1.07)
2	0.28 – 0.32	96	13 (24)	3.74	3.48(+1.26, -0.95)
3	0.32 – 0.36	91	19 (22)	3.39	5.60(+1.60, -1.27)
4	0.36 – 0.40	81	10 (19)	3.08	3.25(+1.39, -1.01)
5	0.40 – 0.44	73	17 (28)	2.80	6.07(+1.86, -1.46)
6	0.44 – 0.48	66	13 (15)	2.40	5.42(+1.96, -1.48)
7	0.48 – 0.52	54	9 (10)	2.10	4.29(+1.96, -1.46)
8	0.52 – 0.56	51	14 (15)	1.98	7.07(+2.44, -1.87)
9	0.56 – 0.60	49	10 (11)	1.83	4.92(+2.25, -1.61)
10	0.60 – 0.64	43	10 (12)	1.67	5.99(+2.56, -1.86)
11	0.64 – 0.68	39	5 (6)	1.40	3.57(+2.42, -1.54)
12	0.68 – 0.72	31	9 (9)	1.17	7.69(+3.51, -2.52)
13	0.72 – 0.76	24	5 (5)	0.963	5.19(+3.51, -2.24)
14	0.76 – 0.80	23	1 (2)	0.849	1.18(+2.71, -0.97)
15	0.80 – 0.84	19	9 (9)	0.738	12.2(+5.6, -4.0)

^a Number (N_{AGN}) of AGN sight lines providing full or partial spectral coverage of the H I Lyman edge (912 Å) over redshift bins ($i = 1 - 15$). The effective redshift, Δz_{eff} , is based on N_{AGN} subtracting partial coverage of bins and portions of spectrum blocked by strong absorbers.

^b Distribution (N_{abs}) of 158 H I absorbers with $\log N_{\text{HI}} \geq 15$ for the 15 redshift bins (from $0.24 \leq z \leq 0.84$). Values in parentheses are number of absorbers with $\log N_{\text{HI}} \geq 14$ (211 in all). Last column shows the frequency of absorbers per unit redshift, $dN/dz \equiv N_{\text{abs}}/\Delta z_{\text{eff}}$, for $\log N_{\text{HI}} \geq 15$. We compute (1σ) error bars for one-sided Poisson statistics (Gehrels 1986) on N_{abs} . Over total pathlength $\Delta z_{\text{eff}} = 31.94$, the average absorber frequency is $dN/dz \approx 4.95 \pm 0.39$. Full statistical analysis (MCMC) of the bivariate distribution, $f(N, z) \equiv (d^2 N_{\text{abs}}/dz dN)$, is given in Appendix B.

TABLE 5
Strong Absorbers and Wavelength Blockage^a

QSO ^b	z_{abs}	$\log N_{\text{HI}}$	z_{QSO}	Affected	Wavelength Blockage
1	0.24770	19.45 ± 0.10	0.47114	Bin 1	opaque below 1137.6 Å
2	0.39043	18.1 ± 0.1	1.131	Bins 1-4	opaque below 1267.7 Å
3	0.41065	17.80 ± 0.05	0.694596	Bins 1-5	opaque below 1286.2 Å
4	0.23740	17.29 ± 0.11	0.5251	...	opaque below 1128.2 Å
5	0.35586	18.3 ± 0.2	0.4556	Bins 1-3	opaque below 1236.2 Å
6	0.30360	19.41 ± 0.12	0.7462	Bins 1-2	opaque below 1188.6 Å
7	0.47379	18.3 ± 0.2	0.665	Bins 1-6	opaque below 1343.7 Å
8	0.41924	16.80 ± 0.05	0.4632	Bins 1-5	minor influence below 1294.0 Å
9	0.46334	17.85 ± 0.02	0.7666	Bins 1-6	opaque below 1334.2 Å
10	0.92772	17.15 ± 0.05	1.1625	Bins 1-14	minor influence below 1757.6 Å

^a Potential spectrum blockage by 10 strong absorbers listed with redshifts z_{abs} and fitted column densities, $\log N_{\text{HI}}$. Absorber column densities and redshifts are revised from values in Stevans et al. (2014), based on analysis of the Lyman limit flux decrement and new fits to CoG for high-order Lyman lines. See Appendix B for details. In 8 cases, strong LyC absorption produces flux decrements at wavelengths $\lambda \leq (911.753 \text{ Å})(1 + z_{\text{abs}})$ listed in comments. Potentially affected bins are noted. However, our survey can still find pLLS by detecting higher Lyman lines longward of the Lyman edge.

^b QSO targets: (1) SDSS J092554.70+400414.1; (2) FIRST J020930.7-043826; (3) SDSS J151428.64+361957.9; (4) SDSS J113327.78+032719.1; (5) SDSS J100902.06+071343.8; (6) SDSS J100102.55+594414.3; (7) SDSS J154553.48+093620.5; (8) SDSS J091029.75+101413.6; (9) SBS 1108+560; (10) PG 1206+459.

TABLE 6
Strong Absorbers (LLS and pLLS)^a

No.	QSO Name	z_{abs}	z_{AGN}	$\log N_{\text{HI}}$ Lehner ⁺ 13	$\log N_{\text{HI}}$ Stevens ⁺ 14	$\log N_{\text{HI}}$ This Paper
1	J092554.70+400414.1	0.2477	0.471139	19.55 ± 0.15	19.26 ± 0.06	19.45 ± 0.10
2	J020930.7-043826	0.39035	1.131		18.00 ± 0.2	18.5 ± 0.4
3	J151428.64+361957.9	0.41065	0.694596		17.93 ± 0.2	17.89 ± 0.06
4	J113327.78+032719.1	0.23756	0.525073		17.53 ± 0.10	17.29 ± 0.11
5	J100902.06+071343.8	0.35586	0.455631	18.40 ± 0.20	17.41 ± 0.04	18.3 ± 0.2
6	J100102.55+594414.3	0.30360	0.746236		17.27 ± 0.04	19.41 ± 0.12
7	J154553.48+093620.5	0.47379	0.665		17.25 ± 0.2	18.3 ± 0.2
8	J091029.75+101413.6	0.41924	0.463194		17.14 ± 0.8	$16.89^{+0.04}_{-0.11}$
9	SBS 1108+560	0.46334	0.76619		17.06 ± 0.1	17.85 ± 0.02
10	PG 1206+459	0.92772	1.16254	17.00 ± 0.10	17.03 ± 0.08	17.10 ± 0.10
11	PG 1630+377	0.27395	1.47607	16.98 ± 0.05	16.92 ± 0.04	17.04 ± 0.05
12	J100535.24+013445.7	0.41853	1.0809		16.37 ± 0.02	16.73 ± 0.10
13	J143511.53+360437.2	0.37292	0.428593	16.65 ± 0.07	16.72 ± 0.06	16.84 ± 0.06
14	J091029.75+101413.6	0.2634	0.463914		16.86 ± 0.5	16.21 ± 0.07
15	J161916.54+334238.4	0.47091	0.470946		16.84 ± 0.1	16.83 ± 0.10
16	J155048.29+400144.9	0.31257	0.496843		16.62 ± 0.06	16.3 ± 0.1
17	J155048.29+400144.9	0.4919	0.496843		16.57 ± 0.02	16.60 ± 0.05
18	PKS 0552-640	0.34513	0.680	16.90 ± 0.08	16.71 ± 0.03	17.01 ± 0.05
19	J124511.25+335610.1	0.55670	0.717		16.50 ± 0.2	16.28 ± 0.10
20	J124511.25+335610.1	0.68927	0.717		16.68 ± 0.2	16.70 ± 0.11
21	J100102.55+594414.3	0.41595	0.746236		16.61 ± 0.02	16.66 ± 0.08
22	HB89-0107-25	0.39913	0.956		16.59 ± 0.02	16.89 ± 0.06
23	J084349.49+411741.6	0.53255	0.989986		16.67 ± 0.05	16.85 ± 0.04
24	J100535.24+013445.7	0.83708	1.0809		16.81 ± 0.01	16.96 ± 0.08
25	PG 1522+101	0.72865	1.32785	16.66 ± 0.05	16.60 ± 0.09	16.62 ± 0.05
26	Q0232-042	0.73888	1.43737	16.72 ± 0.03	16.64 ± 0.08	16.76 ± 0.05
27	PG 1522+101	0.51839	1.32785	16.22 ± 0.02	16.32 ± 0.2	16.28 ± 0.05
28	PG 1338+416	0.68610	1.21422	16.45 ± 0.05	16.49 ± 0.04	16.49 ± 0.05
29	PG 1338+416	0.34885	1.2142	16.30 ± 0.13	16.37 ± 0.06	16.34 ± 0.10
30	PKS 0637-752	0.46850	0.653	16.48 ± 0.04	16.08 ± 0.03	16.48 ± 0.05
31	J141910.20+420746.9	0.28895	0.873501	16.40 ± 0.07	16.17 ± 0.03	16.17 ± 0.05
32	J141910.20+420746.9	0.42555	0.873501	16.17 ± 0.06	16.02 ± 0.02	16.24 ± 0.10
33	J141910.20+420746.9	0.53460	0.873501	16.34 ± 0.17	16.06 ± 0.07	16.15 ± 0.10
34	J143511.53+360437.2	0.38766	0.428593	16.18 ± 0.05	16.15 ± 0.02	16.17 ± 0.05
35	J094331.61+053131.4	0.35455	0.564336	16.11 ± 0.09	16.12 ± 0.09	16.12 ± 0.05
36	PG 1407+265	0.68270	0.946	16.38 ± 0.02	16.39 ± 0.03	16.38 ± 0.05
37	PG 1216+069	0.28231	0.3313	16.40 ± 0.05	16.29 ± 0.01	16.41 ± 0.03
38	J161916.54+334238.4	0.26938	0.470496	16.48 ± 0.05	16.40 ± 0.03	16.40 ± 0.08
39	SBS 1122+594	0.55810	0.852	16.24 ± 0.03	16.42 ± 0.02	16.45 ± 0.06
40	HE 0439-5254	0.61512	1.053	16.28 ± 0.04	16.25 ± 0.04	16.42 ± 0.10
73	J161649.42+415416.3	0.3211	0.440417	20.34 ± 0.12

^a Strong absorbers estimated (Stevens et al. 2014) with $\log N_{\text{HI}} \geq 16.5$ (systems #1-26) and $\log N_{\text{HI}} = 16.0 - 16.5$ (systems #27-40). System #73 is a new DLA. Some were reported previously (Battisti et al. 2012; Lehner et al. 2013; Fox et al. 2013). Columns 3 and 4 list redshifts of absorber (z_{abs}) and AGN (z_{AGN}). Our column densities (this paper) are from new CoG fits to Lyman-series approaching LL. Appendix A discusses CoGs and Ly decrements.

TABLE 7
Summary of LLS Frequency fitting^a

Survey	Instrument	Redshift Range	N_0	γ	N_{LLS}
This Paper	COS	0.24 – 0.48	$0.25^{+0.13}_{-0.09}$	1.14 ± 0.89	8
Storrie-Lombardi et al. 1994	FOS	0.40 – 4.69	$0.27^{+0.20}_{-0.13}$	1.55 ± 0.45	7
Stengler-Larrea et al. 1995	FOS	0.40 – 4.69	$0.25^{+0.17}_{-0.10}$	1.50 ± 0.39	7
Ribaudo et al. 2011a	FOS/STIS	0.25–2.59	0.28 ± 0.05	1.19 ± 0.56	17

^a Redshift evolution of low-redshift LLS ($\log N_{\text{HI}} \geq 17.2$) studied with UV spectra and fitted to $(dN/dz) = N_0(1+z)^\gamma$. We include the current COS survey, two *HST* low-resolution surveys with FOS/G140L (Storrie-Lombardi et al. 1994; Stengler-Larrea et al. 1995) and a low-resolution survey with FOS/G140L and STIS/G140L/G230L (Ribaudo et al. 2011a). The last column gives the number N_{LLS} of low redshift ($z < 0.84$ LLS in the COS survey, $z < 1.04$ in the FOS Key Project, and $z < 0.84$ in Ribaudo et al. (2011a). These surveys contain many more pLLS, which are used in the fits.

TABLE 8
List of Strong (DLA and sub-DLA) Absorbers^a

AGN	z_{abs}	z_{AGN}	$\log N_{\text{HI}} \text{ (cm}^{-2}\text{)}^{\text{b}}$	Comments
PG 1216+069	0.00635	0.331	19.32 ± 0.03	Sightline to System #37
J155304.92+354826.6	0.0830	0.721814	19.55 ± 0.15	Two other strong absorbers ($\log N = 15.18, 15.43$)
J161916.54+334238.4	0.0963	0.470946	20.55 ± 0.10	Sightline to Systems #15 and #56 (Appendix A)
J100902.06+071343.8	0.1140	0.455631	20.68 ± 0.10	Sightline to System #5 (Appendix A)
J092837.98+602521.0	0.1538	0.29545	19.35 ± 0.15	No other strong absorbers with $\log N > 15.5$
B0120-28	0.185	0.436018	20.50 ± 0.10	No other strong absorbers with $\log N > 15.5$
J143511.53+360437.2	0.2026	0.428593	19.80 ± 0.10	Sightline to System #13 (Appendix A)
J1342-0053	0.22711	0.326	18.5 ± 0.5	Prochaska et al. (2017)
J092554.70+400414.1	0.2477	0.471139	19.45 ± 0.15	System #1 (Appendix A)
J100102.55+594414.3	0.30360	0.746236	19.41 ± 0.12	System #6 (Appendix A)
J161649.42+415416.3	0.3211	0.440417	20.34 ± 0.12	System #73 (Appendix A)
J0020930.7-043826	0.39043	1.131	18.5 ± 0.4	System #2 (Appendix A)

^a Four low-redshift Damped Ly α (DLA) and six sub-DLA systems identified in our survey, ordered by absorber redshift (z_{abs}). The first eight absorbers lie below the minimum redshift ($z_{\text{abs}} = 0.24$) of our survey and are not included in our statistical analysis. DLA systems have $\log N_{\text{HI}} > 20.3$ and sub-DLAs have $19.0 < \log N_{\text{HI}} < 20.3$. Two other absorbers have column densities $\log N_{\text{HI}} = 18.5 \pm 0.5$ near the sub-DLA range.

^b Column densities for several systems in this list were listed in other papers (Meiring et al. 2011; Muzahid et al. 2015; Tejos et al. 2014) with column densities determined by fitting damping wings of Ly α profile. For other absorbers (systems #1, 2, 6, 7, 73 in Appendix A), we use our own fits to Ly α damping wings, the LL decrement, and CoG for higher Lyman lines.